FAT AND SODIUM QUANTIFICATION AND CORRELATION BY MRSI

by

Ahmad Abdulrahman M. Alhulail

A Dissertation

Submitted to the Faculty of Purdue University

In Partial Fulfillment of the Requirements for the degree of

Doctor of Philosophy

School of Health Sciences

West Lafayette, Indiana

August 2020

THE PURDUE UNIVERSITY GRADUATE SCHOOL
STATEMENT OF COMMITTEE APPROVAL

Dr. Ulrike Dydak, Chair

School of Health Sciences

Dr. Uzay Emir

School of Health Sciences

Dr. Joseph Rispoli

Weldon School of Biomedical Engineering

Dr. Keith Stantz

School of Health Sciences

Approved by:

Dr. Aaron Bowman

Dedicated to my family

ACKNOWLEDGMENTS

I would like to thank my sponsor, the Saudi Arabia Government represented by the Saudi Arabian Cultural Mission to the United States, for all their generous sponsoring and supporting during my entire period of studying PhD abroad.

I would like to express my sincere gratitude to Dr. Ulrike Dydak and Dr. Uzay Emir for their academic support and research guidance throughout my PhD. I deeply appreciate their great effort that was a major factor in putting this thesis together. I am very grateful for them to give me the chance to work with them which resulted in improving my research skills and widening my vision further. They will be an essential part of any of my future professional success. I am thankful also to the two other members of my advisory committee, Dr. Joseph Rispoli and Dr. Keith Stantz, for their constructive advices, and continuous availability to help and support. I am truly honored to work with these outstanding committee members.

Many thanks for the individuals of the School of Health Sciences to grant such wonderful educational environment, and for all my friends from the MRI lab for the good times they gave me throughout my PhD journey.

I would also like to acknowledge the Life Science MRI Facility, at Purdue University for facilitating the data collection process for my research work.

A special and exceptional thank you to my family, who shared all my good and hard times during my PhD journey. No words will be enough to express my gratitude to them. Their companion, patience, encouragement, prays, and smiles were my booster to finish my overseas PhD.

TABLE OF CONTENTS

LIST OF TABLES

LIST OF FIGURES

LIST OF ABBREVIATIONS

^{1}H	Hydrogen
2D	Two Dimensional
^{23}Na	Sodium
3D	Three Dimensional
ATP	Adenosine Triphosphate
B_0	Main Magnetic Field
BMI	Body Mass Index
BMS	Bulk Magnetic Susceptibility
BW	Bandwidth
CRLB	Cramér-Rao lower bound
CRT	Concentric Ring Trajectory
CT	Computed Tomography
CV	Coefficient of Variance
DW	Density Weighted
EFG	Electric Field Gradient
EMCL	Extramyocellular Lipid
EPSI	Echo-Planar Spectroscopic Imaging
FA	Flip Angle
FF	Fat Fraction

F_{Fast}	Fast Transverse Relaxation Time Component Signal Fraction
FID	Free Induction Decay
FLASH	Fast Low Angle SHot
FOV	Field Of View
FSE	Fast-Spin-Echo
F_{Slow}	Slow Transverse Relaxation Time Component Signal Fraction
GRE	Gradient-Echo
IMCL	Intramyocellular Lipid
IP	In Phase
KW	Kruskal-Wallis
MC	Metabolite-Cycled
MPVT	Minimum Positive Voxel Threshold
MQF	Multiple Quantum Filtered
MR	Magnetic Resonance
MRI	Magnetic Resonance Imaging
MRS	Magnetic Resonance Spectroscopy
MRSI	Magnetic Resonance Spectroscopic Imaging
MSC	Muscle Sodium Concentration
NUFFT	Non-Uniform Fast-Fourier Transform
OP	Out of Phase
OVS	Outer Volume Suppression

QI	Quadrupolar Interaction
RF	Radiofrequency
ROI	Region Of Interest
STD	Standard Deviation
SNR	Signal-to-Noise Ratio
SOI	Slice Of Interest
SQF	Single Quantum Filtered
SSIM	Structural Similarity
T_1	Longitudinal Relaxation Time
T_2	Transverse Relaxation Time
T_2^*	Transverse Relaxation Time in the Presence of Magnetic Field Inhomogeneity
T_{2Fast}	Fast Transverse Relaxation Time Component
T_{2Slow}	Slow Transverse Relaxation Time Component
TA	Total Acquisition Time
TE	Echo Time
TI	Inversion Time
TR	Repetition Time
TSC	Total Sodium Concentration
UTE	Ultra-Short Echo Time

ABSTRACT

Lipids and sodium (^{23}Na) are two essential components of the human body. They play a role in almost all biological systems. However, an increase in their levels is associated with metabolic diseases. The elevation of their contents can cause similar health disorders. Examples of prevalent disorders that share an increase of musculoskeletal lipids and ^{23}Na are hypertension and diabetes. However, the relationship between in vivo lipid and sodium levels in pathophysiology has not been studied enough and therefore is still unclear. Additionally, the available quantification methods to facilitate such a study may not be practical. They are either invasive, not sensitive enough, or require an impractical measurement time.

Therefore, in this work, our aims were to develop practical in vivo methods to quantify the absolute sodium concentration as well as the concentration of each lipid component individually, and to study the correlation between them within the skeletal muscles.

Since lipids and ^{23}Na have different nuclear magnetic resonance properties, their quantification by magnetic resonance (MR) techniques face different challenges. Thus, we optimized different MR spectroscopic imaging (MRSI) techniques for lipids and ^{23}Na.

Our proposed proton MRSI was able to provide eight lipid fat fraction (FF) maps representing each musculoskeletal lipid component (fatty acid) detected by our MRSI technique, and demonstrated a superior sensitivity compared to the conventional MR imaging methods. (*Aim 1; Chapter 2*)

For ^{23}Na, our developed ^{23}Na-MRSI was able to measure and map the absolute ^{23}Na concentration with values agreeing with those reported previously in biopsy studies, and with a high repeatability (CV < 6 %) within significantly shorter acquisition time compared to other available techniques. (*Aim 2; Chapter 3*)

Finally, the ^{23}Na concentration and the fat fractions of each lipid component within healthy skeletal muscles were measured and correlated using our developed MRSI methods. Our findings suggest a positive regional relationship between ^{23}Na and lipids and negative correlation between ^{23}Na and BMI under healthy conditions. (*Aim 3; Chapter 4*)

CHAPTER 1 : INTRODUCTION

1.1 MRSI

1.1.1 MRSI Principle

Magnetic resonance spectroscopic imaging (MRSI) is basically multi-voxel MR-spectroscopy (MRS) that can be post-processed and represented as a spatial distribution (image) of the collected data. MRS is a nuclear magnetic resonance technique to collect in vivo information about certain metabolites within a specific volume of interest noninvasively and represent them within a frequency spectrum. Unlike magnetic resonance imaging (MRI), MRS measures the signal at different time points while it is decaying. This measurement is called a free induction decay (FID). If a Fourier transform is performed, the FID data in the time domain can be transformed to the frequency domain and represented as a frequency spectrum. The spectrum will show the detected metabolites sorted as signal peaks at their characteristic resonance frequency shift in Hz or ppm.

Each nucleus (with nonzero magnetic moment) has a unique gyromagnetic ratio (γ). Thus, within a given magnetic field (B_0), a nucleus precesses with a Larmor frequency ($\omega = \gamma B_0$). However, when a nucleus is bound to another molecule (like oxygen or carbon), the surrounding electrons induce a small opposing magnetic field to the main applied B_0 with a shielding constant (σ) that results in shifting their frequency as follows:

$$\Delta\omega = \gamma B_0 (1- \sigma)$$

These small chemical shifts in frequency help to differentiate the metabolite signal. However, further spectral optimization may be required for a better differentiation. For ^1H, since the human body is basically made of water, the H_2O signal peak overwhelms the other metabolite peaks. Hence, this large water signal needs to be suppressed in order to see the smaller metabolite peaks.

With conventional MRSI methods, long acquisition times are required to collect enough and high-resolution voxels (for producing images) and to suppress the water peak. Therefore, an acceleration of these processes is needed.

1.1.2 MRSI Acceleration

Similar to MRI, an MRSI acquisition is usually accelerated by trying to sample k-space more efficiently. To speed up filling the Cartesian lines, methods like echo-planar spectroscopic imaging (EPSI) can be implemented.[1,2] Alternatively, center-out (non-Cartesian) k-space-filling trajectory methods such as concentric rings,[3] or spirals[4] can be used to acquire enough imaging data within a shorter duration. Additionally, parallel imaging techniques can be applied to accelerate MRSI with multi-channel coils.[5–7] While each method has its advantages and limitations, a density-weighted concentric ring trajectory (DW-CRT) acquisition method has been chosen to perform this work.[8] The main reason to pick this method is that it has been found that DW-CRT provides a higher signal-to-noise ratio (SNR) compared to the EPSI and the spiral methods even for x-nuclei.[9] This advantage is very important for ^{23}Na-MR since it suffers from a low SNR due its low NMR sensitivity and natural concentration as will be described below. For ^{1}H, techniques that can boost the SNR are also preferred to enhance the detection of some fatty acids of relatively low signal. Moreover, this SNR advantage also allows good data quality with a smaller number of averages (shorter scan duration). The main factor leading to this advantage is that k-space is filled more densely at its center (see Figure 1.1), where data of low spatial frequency exist and contain the general signal distribution information. Additionally, it is Hanning filter density-weighted by design, which boosts the SNR further.[8]

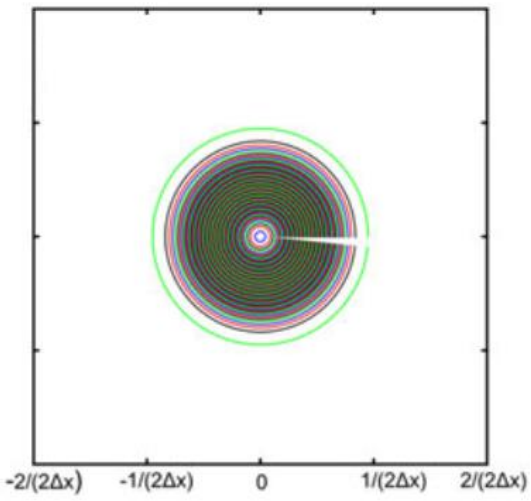

Figure 1.1 Density weighted concentric ring trajectory scheme used to fill the MRSI k-space. This Figure adapted from Chiew et al. [8]

1.2 Lipids

1.2.1 Biological Importance

In the context of this work, the term lipid will be equivalent to triglyceride, which is a group of lipids that can be detected by proton (^{1}H) MR techniques. Triglycerides are built from three fatty acids that are linked by a glycerol backbone.[10] Triglycerides form 60 - 85% of adipose tissue.[11] This lipid serves as an essential source of energy. However, the elevation of its content has been linked to several common diseases, such as type 2 diabetes and cardiovascular disease.[12] More in-depth investigations have related the accumulation of saturated fatty acids to insulin sensitivity.[13] Additionally, recent studies suggest an influence of lipids on the immune system and inflammation.[14] Lipid accumulation was also used as a sign of cancer.[15]

In the musculoskeletal system, lipids exist within the bone marrow, as strands between the muscle fibers (extra-myocellular lipids; EMCL), as droplets inside the of muscle cells (intra-myocellular lipids; IMCL) with a lower concentration, or stored as subcutaneous fat.[16] The elevation in musculoskeletal fat content has been related to Duchenne muscular dystrophy,[17] type 2 diabetes mellitus,[18] tendon tear severity,[19] Charcot-Marie-Tooth type 2 F disease,[20] osteoporosis,[21] and knee osteoarthritis.[22] Additionally, the increase of IMCL has been found to be contributing to insulin sensitivity.[23,24] Moreover, IMCL in contact with mitochondria has been found to be proportional in size with exercise intensities [25] and provides useful information about the energy supply,[26] and mitochondrial disorders.[27] In addition, it may indicate physiological details as it has been shown that muscle exercise results in altering the levels of bulk methylene IMCL.[28] Similarly, the increase of saturated lipids and decline of unsaturated olefinic lipid signal in bone marrow has been used as a sign of osteoporosis.[29]

1.2.2 Lipid Quantification Methods

Currently, there are several methods available to investigate the body fat content level. A biopsy specimen can be extracted from the region of interest (ROI) and quantified in vitro by electron microscopy,[30] histochemistry (Oil red O staining),[31] or biochemical analysis.[32] However, this method is invasive and does not provide the spatial distribution of lipids. Alternatively, computed tomography (CT)[33] and MRI can noninvasively image a larger area for fat content assessment. MRI is preferred over CT to use for fat quantification, especially in children, because MRI is used

without ionizing radiation. An alternative to CT, dual-energy X-ray absorptiometry (DXA) that utilizes a very low radiation dose can be used to assess total fat mass, but it is prone to errors due to the variation in soft tissue hydration.[34,35]

The Dixon technique[36] is the standard MRI method for measuring in vivo fat fraction (FF) quantification and mapping. As demonstrated in Figure 1.2, the conventional Dixon technique generates fat-only (F) and water-only (W) images that are usually used to calculate their FF maps (= F/W+F). In order to generate these W and F images, the sequence needs to acquire at least two signal echoes, one echo when fat and water spins are in-phase (IP) and another echo when they are out-of-phase (OP). Since the ^{1}H signal is coming mainly from water signal and the lipid component resonating at ~3.5 ppm lower than water, the time when their spins are IP or OP can be estimated based on this resonance frequency difference. The signal sum of the IP and OP acquisitions will eliminate the fat signal contribution and render double the water signal, and their difference will result in double the fat signal without the water signal. By dividing the results by two, images of water-only and fat-only signals are produced.

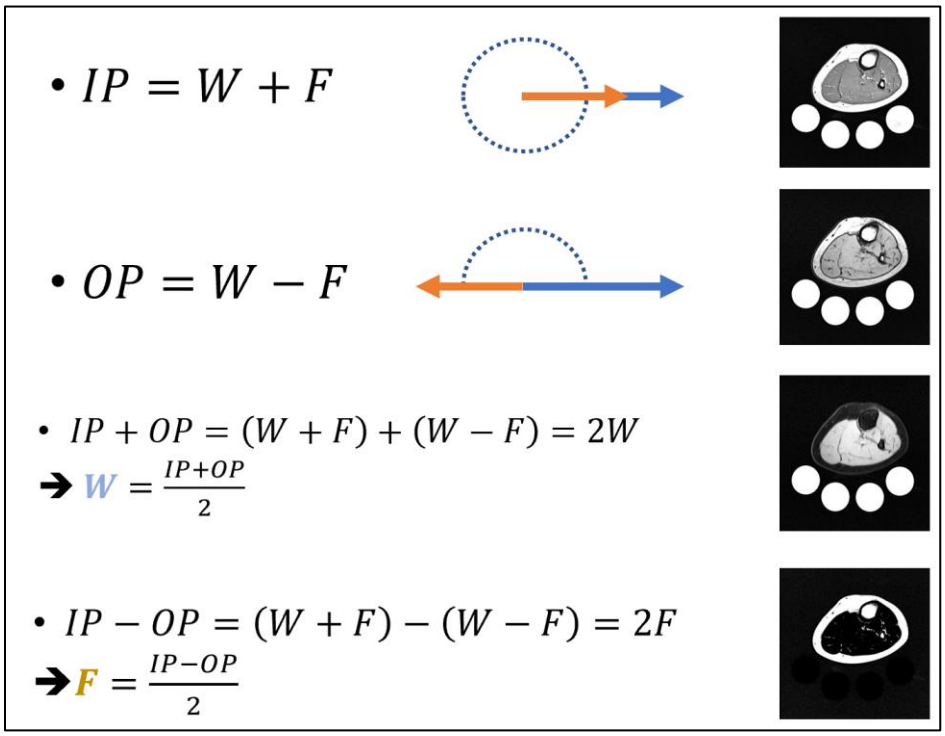

Figure 1.2 Dixon fat- and water-only image reconstruction steps. The fat (F) signal (orange), and water (W) signal (blue) are measured at two echo times. Once when they are in-phase (IP), and once when they are out-of-phase (OP). The water-only signal can be separated by summing the IP and OP signals. The fat-only signal can also be generated by subtracting the IP and OP signals

Although conventional imaging techniques can map and quantify the total fat content, they cannot differentiate their fatty acids components. To differentiate these lipid components, ^{1}H-MRS is usually used. The differences in chemical saturation, chain length, and location of lipid components relative to the cells result in a differentiated frequency of their protons that allows ^{1}H-MRS to detect their distinct signals noninvasively (see Figure 1.3 for a spectrum example). However, single voxel MRS cannot map the lipid's FF distribution, which was found to vary with muscle fiber types.[37] Alternatively, MRSI can cover a larger area with multiple voxels, but conventional MRSI requires a long acquisition time. Thus, an accelerated MRSI technique will be proposed in this work.

1.2.3 Musculoskeletal Lipid MRSI Challenges

To provide FF data, separated water and fat information are needed. Hence, two MRSI acquisitions are conventionally performed: one acquisition containing the water information, and another with a water-suppression for lipid information. However, to reduce the scan duration, using only one of these measurements is sometimes used. Each of these options comes with its drawbacks. With the non-water suppressed spectra, the water signal overwhelms the surrounding lipid peaks close to it, and only a few of the strong lipid peaks resonating away from the water frequency can be distinguished (see Figure 1.3). On the other hand, the use of water suppressed spectra alone pushes users to redefine the FF and calculate it without referencing it to the water signal. Additionally, the large water signal is important to determine the local magnetic field shifts and to correct the spectral phase and eddy current effects.[38,39] In this work, the use of a metabolite-cycled (MC) non-water-suppressed technique combined with the DW-CRT acquisition method is proposed to provide separated water and lipids information from one fast measurement, as will be shown in the following chapter.

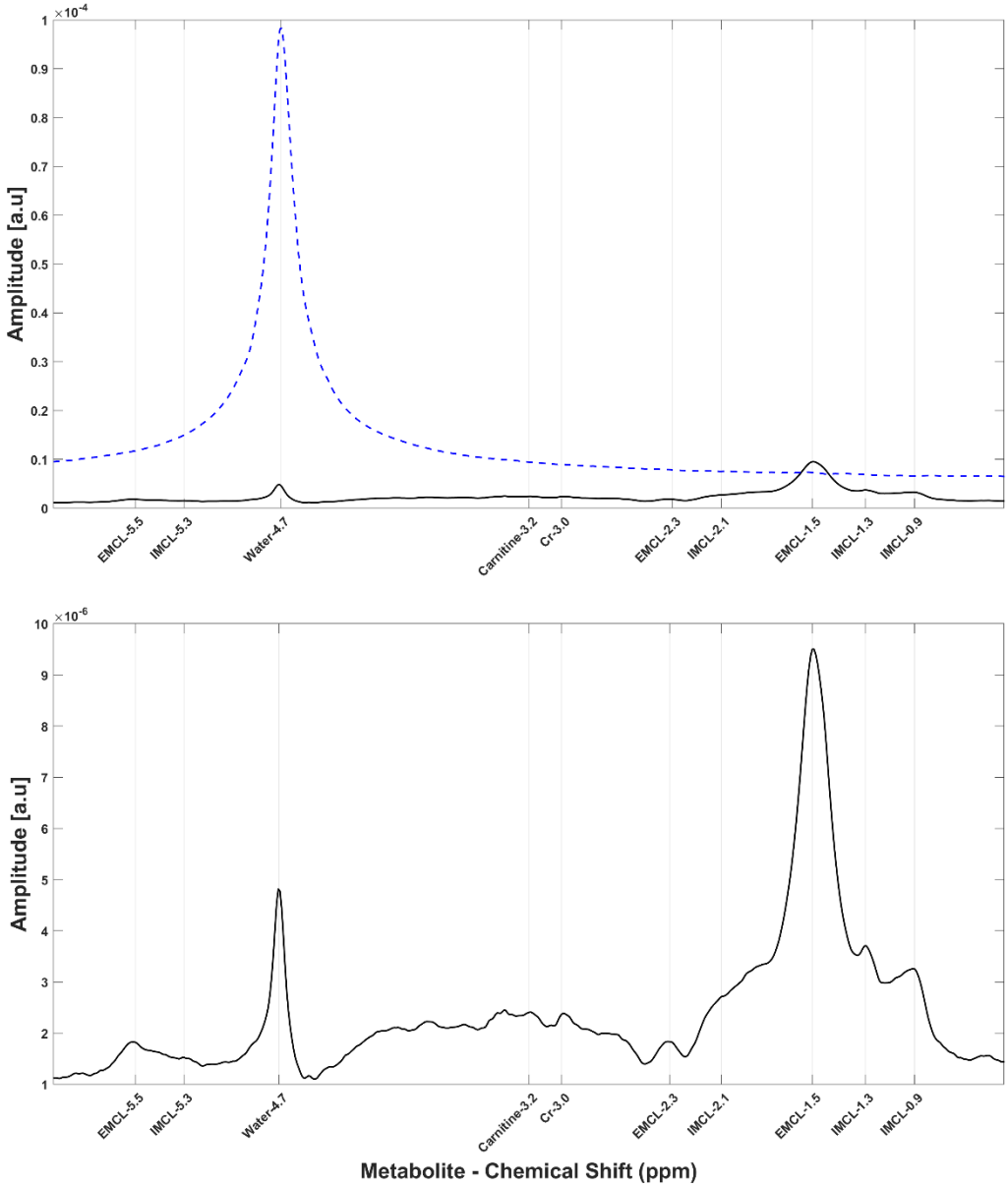

Figure 1.3 An example of a typical 1H-MR spectrum of skeletal muscle without water suppression (top), and after water suppression (bottom). The numbers next to each metabolite represents the chemical frequency shift in ppm

Another challenge facing musculoskeletal MRSI is the heterogeneity of the muscle fiber orientation. Due to the local bulk magnetic susceptibility (BMS), EMCL and IMCL are usually separated by ~ 0.2 ppm.[16,40] However, the EMCLs that follow the fiber orientation will have different angles relative to the main B_0 direction resulting in shifting its chemical shift closer to the IMCL. This factor can be reduced by increasing the spatial resolution to enhance the spectral line by reducing spatial variation within the voxels. Thus, we are implementing an MRSI technique

with a 0.25 mL resolution, which has been found to be sufficient to separate the adjacent IMCL and EMCL peaks.[41]

1.3 Sodium

1.3.1 Biological Importance

Sodium (^{23}Na) is the most abundant positive ion that exists naturally in our human body.[42] It plays a vital role in regulating nerve impulse, muscle action, blood and body fluid volume, osmotic pressure, immunity, and cell membrane viability (Na+/K+ pump).[42] In healthy tissues, ^{23}Na concentration is constant (within a specific range) and always lower within the intracellular space compared to the extracellular region.[42] An increase of sodium concentration over the normal ranges can be a result of one of three scenarios. One possibility is due to an increase in intracellular concentration that can be caused by the loss of cell integrity or the impairment of energy metabolism. A second potential reason is an increase in the extracellular volume that may reflect cells death or edema. Finally, it can result from an increase of vascularization for reasons such as the existence of a malignant tumor, or an infection.[42]

By using sodium MRI, several health disorders in different body locations can be evaluated. For example, in the brain, ^{23}Na-MRI has been used to assess strokes,[43] multiple sclerosis,[44] Alzheimer's disease,[45] and Huntington's disease.[46] In muscles, ^{23}Na-MRI has shown feasibility to diagnose diabetes,[47] muscular channelopathy,[48] and hypertension.[49] It was also proposed for breast cancer diagnosis,[50] and early therapeutic response assessment.[51]

1.3.2 Sodium MR

Sodium nuclear-MR (NMR) properties are very different than ^{1}H NMR properties (see figure 1.4). The 3/2 nuclear spin results in four quantum states (m = -3/2, -1/2, +1/2, and +3/2) with three possible transitions. These three transitions occur at the same NMR frequency unless further interactions exist.[52] Since it has a nuclear spin >1 (3/2), it exhibits a quadrupolar moment (Q), which interacts with the electric field gradients (EFG) generated by the local electronic distribution around the macromolecules and cell membranes .[52,53] Unlike the transverse relaxation of ^{1}H that is mainly determined by the dipole-dipole interaction, the quadripolar interaction (QI) is the dominant factor determining the decay nature of ^{23}Na signal.[52] This QI can lead to an NMR

frequency shift that gives rise to extra two lines corresponding to the long (satellite) transitions (between m =+1/2 and +3/2, and m =-1/2 and -3/2) resulting in three spectral lines under particular environmental circumstances.[53] The QI and the movement freedom of sodium spins determine this spectrum line separation and the relaxation mode of the signal.[54] Within liquids, the Q interactions with EFG are time averaged to zero leading to a mono-exponential transverse relaxation time (T_2) and one spectral peak.[42,54,55] Within the biological environment, this interaction does not average to zero, and the decay mode and magnitude will be affected by the motion restriction. The highest the restriction, the strongest the NMR frequency splitting (T_{2fast} and T_{2slow} observed), and the faster the bi-exponential decay. However, within an isotropic motion, the T_{2fast} matches the T_{2slow} resulting in a mono-exponential decay. In muscle tissues, T_{2fast} = 0.5-3 ms, and T_{2slow} = 12-23 ms were observed.[55]

NMR properties	^{23}Na	^{1}H
Spin	3/2	1/2
Gyromagnetic ratio [MHz/T]	11.25	42.58
Relative sensitivity [%]	9.2	100

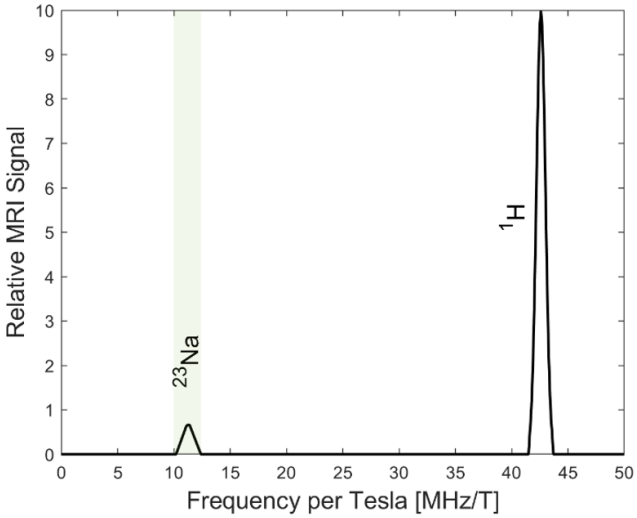

Figure 1.4 Sodium NMR properties compared to proton next to a simulation of their peaks (assuming similar proton density, and that the MR sensitivity is the only determining factor of SNR variation). The Table information was extracted from Hu et al.[56]

1.3.3 Sodium MR Quantification Methods

Since ^{23}Na is resonating at a totally different frequency (Figure 1.4), we purchased a dedicated coil that tuned to the ^{23}Na frequency at 3T (Figure 1.5, top panel). The coil is a transmit/receive birdcage knee coil (32.6 MHz, Stark-Contrast, Erlangen, Germany).

For quantification purposes, four cylindrical phantoms were filled with increasing and known sodium concentration solutions (10, 20, 30, and 40 mmol/L) to be positioned under the

subject leg within a homemade holder (Figure 1.5, bottom panel). 2.9 g/L $CuSO_4$ were added to each phantom to shift the sodium T_1 into the in-vivo range.

Our sodium MR images will cover the leg and the phantom area. As can be seen from the example in Figure 1.6, a concentration map can be generated by calibrating the phantom signal to its previously known concentration using a linear regression line.

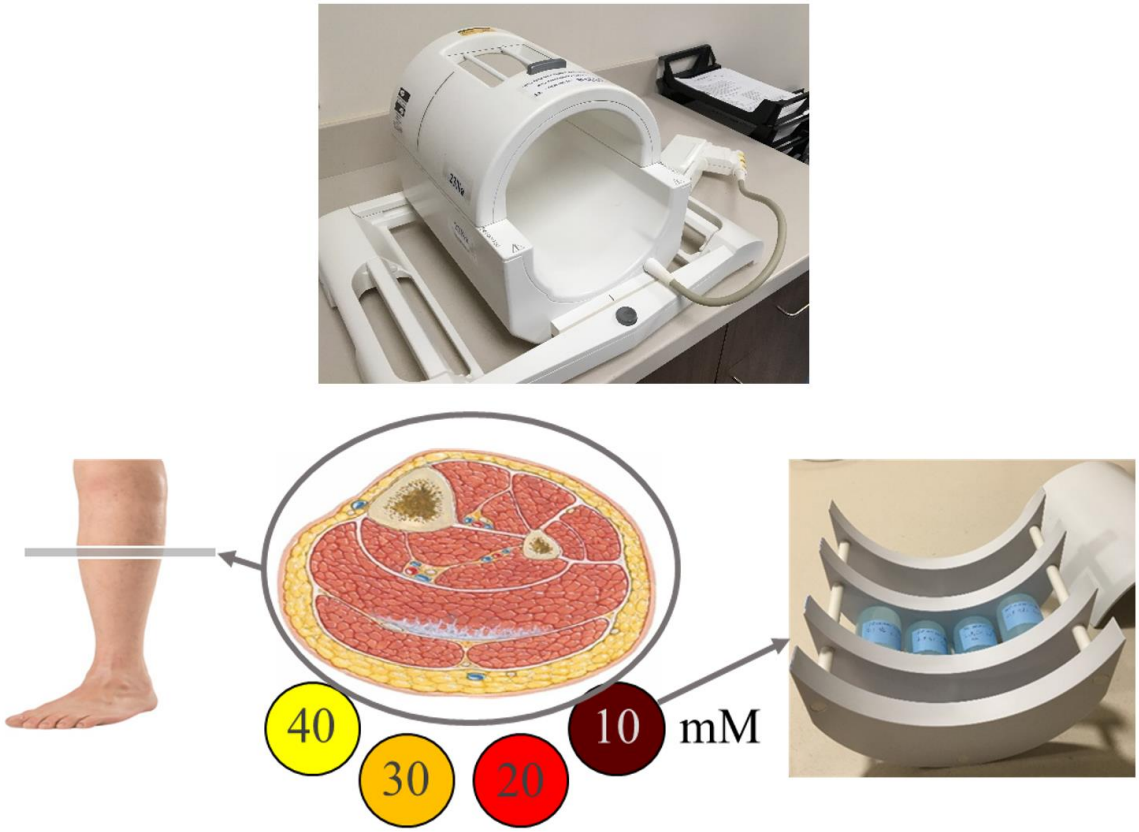

Figure 1.5 Quantitative ^{23}Na-MRI study setup. Top: Special coil tuned to ^{23}Na Larmor precession frequency. Bottom: phantoms with known ^{23}Na concentration used as quantification standards placed within a homemade holder underneath the subject's body region to be scanned (lower leg in our case)

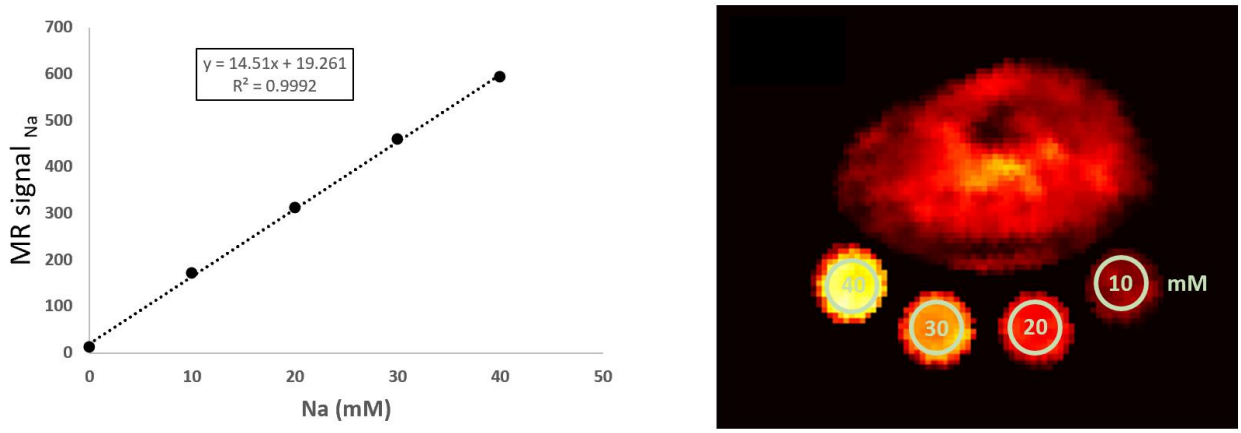

Figure 1.6 Example of a sodium signal-to-mM calibration line (left) used to reconstruct a ^{23}Na-MRI concentration maps (right)

1.3.4 Sodium MR Challenges

Although ^{1}H MRI provides better anatomical images, ^{23}Na MR techniques can give extra information. For instance, ^{23}Na results can be used as a direct biochemical marker for cell integrity and tissue viability. Also, ^{23}Na-MR techniques can be used as an early detection tool for several disorders. However, ^{23}Na MRI suffers from a set of challenges. First, it has a low SNR compared to ^{1}H (Figure 1.7). Additionally, the very fast transverse relaxation times aggravate this issue further. Thus, measurements at ultra-short TE (UTE), increasing the voxel size, and taking more averages are usually needed to enhance the SNR. To use UTE, 3D methods are implemented since it does not require applying slice selection before data readout. Increasing voxel size improves the SNR at the expense of the image spatial quality, introducing large volume effect artifacts within the voxels, and signal leakage to the surrounding voxels due to the larger point spread function. In addition, taking more averages can reduce the noise, but it will lengthen the scan duration.

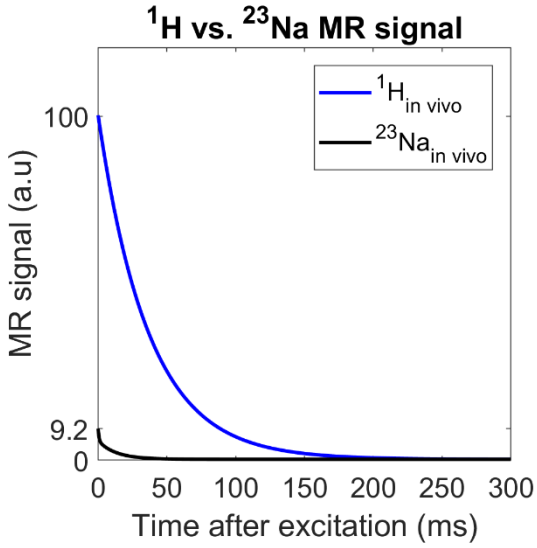

Figure 1.7 Low sodium NMR sensitivity compared to ^{1}H. The figure shows a simulation of ^{1}H and ^{23}Na MR signal decay [assuming similar concentration]

An extra challenge arises when quantification with external standards are used since the relaxation within these standards (mono-exponential) does not represent the relaxation within the biological system (bi-exponential). As can be seen from Figure 1.8, as the time after excitation increases, the difference between the in vivo and in vitro signals increases even though they have the same initial magnetization.

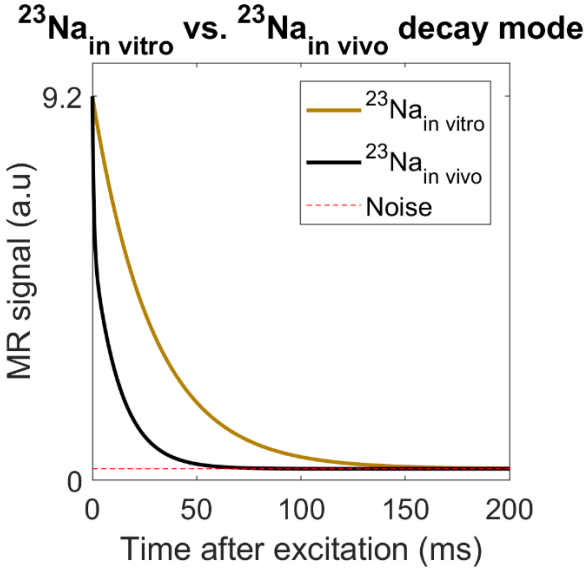

Figure 1.8 Simulation mimicking the ^{23}Na nuclei decay mode in vivo (bi-exponential) and in vitro (mono-exponential)

Even using UTE may not be enough to avoid this later issue. A better approach to deal with this issue is to estimate the relaxation constants and calculate the initial magnetization value voxel-wisely. This will also boost the SNR. Here, we propose a high-resolution 2D-MRSI FID method with DW-CRT to acquire several time points after excitation to estimate the T_2^* values within an acceptable scan time. To start measuring shortly after excitation, an outer volume suppression (OVS) bands will be applied to determine the slice location and thickness.

1.4 Specific Aims

Skeletal muscle represents approximately 55% of the body mass.[57] It is considered a major source of energy and responsible for about 40 - 80% of whole-body insulin-stimulated glucose uptake.[57] Interestingly, common diseases have been linked to the increase in the levels of both lipids and sodium within this organ. However, these correlations have been found in separate studies (lipid or sodium). For example, the elevation in musculoskeletal fat content has been related to Duchenne muscular dystrophy,[17] and type 2 diabetes mellitus.[58] Similarly, other independent studies have linked the level of musculoskeletal sodium to these same diseases.[47,59] Recently, one study found a positive relation between the Dixon's total FF and sodium levels in muscular periodic paralyses patients.[60] In addition to the similar trend of ^{23}Na and fat in the same diseases observed in the separate studies mentioned above, it has been shown that muscle exercises can alter the levels of both ^{23}Na[61,62] and IMCL.[28] Moreover, Tarnopolsky et al. (2007) observed that exercises increased the proportion of IMCL in physical contact with mitochondria.[63] This influence of exercise on IMCL and ^{23}Na may suggest an energy metabolism linkage between them. However, a work focusing on correlating their levels in the same study, and with a robust method was not conducted and whether there is a correlation between them in healthy subjects is still unclear. Thus, studying the relationship between the healthy skeletal muscle ^{23}Na and lipid levels deserves a more in-depth look, and with appropriate tools.

As discussed earlier, lipid and sodium quantification methods have several limitations. The lipid quantification methods either cannot differentiate between IMCL and EMCL, have limited spatial coverage, or require a lengthy scan. On the other hand, current ^{23}Na MRI quantification methods provide data biased by T_2^* or need a long scan session to acquire data to correct for the T_2^*. Thus, there is an urgent need for a technique that can provide separate FF maps for individual lipid compartments as well as an accelerated method that accounts for the T_2^* of ^{23}Na.

Accordingly, the following are the specific aims of this thesis:

Aim 1: *To generate separate spatial FF maps for IMCL and EMCL components by using fast and high-resolution MRSI.*

Based on the amplitude and unique resonance frequency of each lipid type that can be identified by the MRSI technique, separate IMCL and EMCL maps can be generated. In addition, the metabolite-cycled technique will be implemented to acquire the water-only signal map without additional measurement. From these maps, FF maps (= signal of specific lipid component/total signal) will be generated. Since MRSI is being acquired efficiently using the DW-CRT k-space-filling approach, the scan time can be reduced (Chapter 2).

Aim 2: *To generate T_2^*-corrected absolute concentration maps of musculoskeletal ^{23}Na using high-resolution FID-MRSI.*

A high-resolution MRSI sequence will be tuned to ^{23}Na and used to generate ^{23}Na concentration maps for the calf muscles and the calibration bottles, which work as concentration references. To account for the variation in the T_2^* values (in vivo and in vitro), fitting of the ^{23}Na-MRSI FID data will be used to map each ^{23}Na T_2^* relaxation compartment (fast and slow) and estimate the initial magnetization (Chapter 3).

Aim 3*: Identify the relationship between ^{23}Na and IMCL levels within healthy skeletal muscles measured by MRSI.*

Sodium and lipid data will be collected by using the developed MRSI techniques. The resulting maps will be segmented to extract quantitative muscle data. The FF and absolute sodium concentration levels within healthy skeletal muscles will be correlated to evaluate their relationship. The BMI and sex differences will also be considered (Chapter 4).

CHAPTER 2 : FAT-WATER SEPARATION BY FAST METABOLITE CYCLING MAGNETIC RESONANCE SPECTROSCOPIC IMAGING AT 3 T: A METHOD TO GENERATE SEPARATE QUANTITATIVE DISTRIBUTION MAPS OF MUSCULOSKELETAL LIPID COMPONENTS

Published in Magnetic Resonance in Medicine (2020;00:1–14); Adapted Version

***Ahmad A. Alhulail**, Debra A. Patterson, Pingyu Xia, Xiaopeng Zhou, Chen Lin, M. Albert Thomas, Ulrike Dydak, Uzay E. Emir*

2.1 Introduction

The accumulation of adipose tissue in the human body is a risk factor for many common health disorders, such as type 2 diabetes mellitus and cardiovascular disease.[12,64] Indeed, obese children and adolescents are more likely to develop such health problems.[65–67] It has been found that intramyocellular triglycerides (lipids) content has a direct relationship to insulin resistance,[23,24] and is hypothesized to be a precursor to type 2 diabetes mellitus.[18,68] Thus, a non-invasive method to reliably evaluate particular lipid content can be useful in the early detection and prevention of such diseases in children, adolescents, and adults.

Currently, there are several methods available to investigate fat content within the muscles of the body. An invasive biopsy specimen can be extracted from a limited region of interest (ROI).[30–32] Alternately, computed tomography (CT)[33] and magnetic resonance imaging (MRI) can noninvasively image a larger area for fat content assessment. However, MRI is preferred over CT for fat quantification, especially in children, because CT uses ionizing radiation.

The Dixon MRI technique has been used to quantify in vivo total fat fraction (FF).[36] This technique has been considered to be the standard MRI method in providing information about the fat level from a relatively large area in the body. However, the clinically available Dixon MRI techniques are utilized to map the total fat fraction rather than the individual lipid component (Table 2.1) as these techniques cannot differentiate the signal amplitude of each fatty acid separately. In certain situations, individual lipid component information might reflect different pathology or physiology. For instance, the methylene lipid group $(CH_2)_n$ is considered to evaluate arterial stiffness.[69] On the other hand, only the intramyocellular methylene (IMCL$(CH_2)_n$) is the lipid component of particular interest since its elevated level has been found to be a biomarker for

insulin resistivity[24,70] as well as for mitochondrial disorder MELAS.[27] All these studies indicate a need to measure the lipid components separately.

Table 2.1 Common musculoskeletal lipid signals detected by MR techniques[16,40,71–73]

Lipid	Chemical shift [ppm]	Chemical group	Location in muscles	Bone marrow & subcutaneous existence
IMC/L (CH_3)	0.9	Methyl **CH_3**	IMCL	✓
EMCL (CH_3)	1.1		EMCL	*x*
IMC/L $(CH_2)_n$	1.3	Bulk methylene **$(CH_2)_n$**	IMCL	✓
EMC/L $(CH_2)_n$	1.5		EMCL	β-methylene CO–CH_2–**CH_2**–
IMC/L (CH_2–CH)	2.1	Allylic methylene –**CH_2**–CH=CH–	IMCL	✓
EMC/L (CH_2–CH)[a]	2.3		EMCL	α-methylene CO–**CH_2**–CH_2–
IMC/L (–CH=CH–)	5.3	Unsaturated olefinic fat –**CH=CH**–	IMCL	✓
EMC/L (–CH=CH–)	5.5		EMCL	

Abbreviations: EMCL, Extramyocellular lipid; IMCL, Intramyocellular lipid; L, lipid in general (e.g., within the bone marrow or subcutaneous spectra).
[a]Within the bone marrow or subcutaneous spectra, this lipid is L(CH_2–CH_2–).

The single-voxel magnetic resonance spectroscopy (SV-MRS) can be used to differentiate the lipid components. However, it has a limited volume of interest. Alternatively, conventional magnetic resonance spectroscopy imaging (MRSI) methods can be used to cover an entire cross-section over the region of interest, but it requires a long scan time between ~ 17 to 51 minutes.[41,74–77] Acceleration of MRSI sequences had been achieved by reducing the flip angle and repetition time (TR),[78] or by using a gradient-echo sequence with several echo time (TE) step increments.[79] These accelerated methods allow a very high resolution (<0.1 mL) within a shorter acquisition time (~ 10-15 minutes). However, they compromise on large water residual and only allowing for detection of the most intense methylene peaks.[80] MRSI acceleration was also achieved by using a circular sampling acquisition,[81] or by implementing an echo planer acquisition technique to speed up the scan by trading the signal-to-noise ratio.[80,82] However, these techniques alone do not provide water information without an extra measurement.

High spatial resolution is important since it enhances the spectral line separation and eventually the detectability of different lipid peaks. Extramyocellular lipid (EMCL) and intramyocellular lipid (IMCL) are usually separated by ~ 0.2 ppm due to the local bulk magnetic susceptibility (BMS).[16,40] Unlike IMCL, EMCL extends along the muscle fibers, and thus its chemical shift may be affected by the fiber orientation relative to the main magnetic field (B_0) direction because of the experienced anisotropic BMS.[16,83] The separation of EMCL from IMCL was found to be maximal when the fiber orientation is parallel to B_0. However, the precision frequency of the EMCL starts approaching that of IMCL as the muscle fibers orientation deviates away from B_0 direction.[16] Therefore, muscles with asymmetrical fibers orientation distribution such as the soleus muscle will have broader EMCL spectral linewidth.[84] Thus, using techniques of high spatial resolution is desired to reduce the potential variation of the fiber orientation within the same voxel and eventually mitigate its influence of widening the EMCL spectral line width. This is especially useful to resolve the peak of EMCL$(CH_2)_n$ and its adjacent smaller peak of IMCL$(CH_2)_n$.

Therefore, there is a need for a reliable and fast non-invasive in vivo acquisition method that is capable of providing the spatial distribution for each lipid component of interest within a clinically acceptable acquisition time. In this work, we demonstrate a high-resolution, density-weighted concentric ring trajectory (DW-CRT) [85] metabolite cycling (MC) free induction decay (FID) MRSI acquisition technique to provide the spatially resolved water and lipid spectra simultaneously. By using this advantage, the water signal information can be used as an internal reference to calculate the FF voxel-wisely in a similar approach used by the Dixon method, but for each lipid component individually based on their amplitude and unique resonance frequency. Thus, the aim of this study is to investigate the regional distribution of each lipid component over the calf muscles in an adolescent population.

2.2 Methods

2.2.1 Human Subjects

In vivo calf muscle scans were performed for five healthy non-obese adolescent volunteers [2 males and 3 females; age 12-16 years (median = 14 years); body mass index (BMI) = 20 ± 3 Kg/m^2]. The scans were acquired at the maximum circumference of the lower leg. All subjects

stated that they did not exercise for at least 24 hours before their scan. The study was conducted in accordance with the institutional review board of Purdue University. Before being scanned, an informed written assent was obtained from all the subjects, and written consent was obtained from their parents.

2.2.2 Scanning Parameters

The data were acquired by using the integrated body coil of the Siemens Prisma 3T MR system (Siemens, Germany). The FID DW-CRT MRSI was prescribed using a Hanning-windowed acquisition with an alpha of 1 and the following parameters: field of view (FOV) = 240 × 240 mm^2, matrix size = 48 × 48, acquisition delay = 4 ms, repetition time (TR) = 1 s, points-per-ring = 64, temporal samples = 512, resolution = 5 × 5 × 10 mm^3 (nominal resolution= 0.25 mL), number of rings = 24, spatial interleaves = 4, and spectral bandwidth = 1250 Hz. For the MC, similar parameters to that used in Steel et al.[85] and Emir et al.[86] were implemented: an 80 Hz transition bandwidth ($-0.95 < M_z/M_0 < 0.95$) and 820 Hz inversion bandwidth ($-1 < M_z/M_0 < -0.95$), 70 to -750 Hz) downfield/upfield from the carrier frequency (carrier frequency offset = +60 Hz and -60 Hz for downfield and upfield) were defined. The number of averages was 1, corresponding to a total acquisition duration of 3 minutes and 16 seconds.

For comparison, imaging with a 3-point fast-spin-echo (FSE) Dixon sequence was performed with echo time (TE) = 11 ms, TR = 5 s, 2 averages, FOV = 200 × 200 mm^2, and resolution = 0.6 × 0.6 × 10 mm^3. Since Dixon is considered the standard MR technique of clinical scanners to quantify FF and map the fat only and water only distributions, its results will serve as a reference to assess the goodness of the MRSI results.

To get an anatomical image suitable for segmentation, an image was acquired with a T_1-FLASH sequence with TR/TE = 250 ms/2.46 ms, flip angle = 60º, 2 averages, 0.6 x 0.6 x 10 mm^3 resolution, and FOV = 200 x 200 mm^2.

All the above sequences were planned to collect data from the same axial slice placed at the scanner isocenter.

2.2.3 Phantom Experiment

In order to assess the quantification accuracy, a lipid phantom with 50:50 lipid/water concentration has been constructed as described in Hu et al. study.[87] The Dixon and MRSI sequences were used to scan the lipid and water only phantoms.

2.2.4 MRSI Post-processing

The MRSI data were reconstructed in MATLAB (MathWorks, Natick, MA, USA). The gridding and the Fast Fourier Transform were performed by utilizing the Nonuniform FFT (NUFFT) method[88] without using any post-hoc density compensation since DW-CRT is already weighted by design.[8] The voxel-wise frequency and phase corrections were performed using cross-correlation and least-square fit algorithms, respectively, as described in Emir, et al..[86] The FIDs were smoothed by using a Gaussian filter of 250 ms timing parameter and zero filling to 1024 time points. Following, the water-only and the metabolite-only spectra were created by summing and subtracting the alternating FIDs, respectively, as described in Figure 2.1.

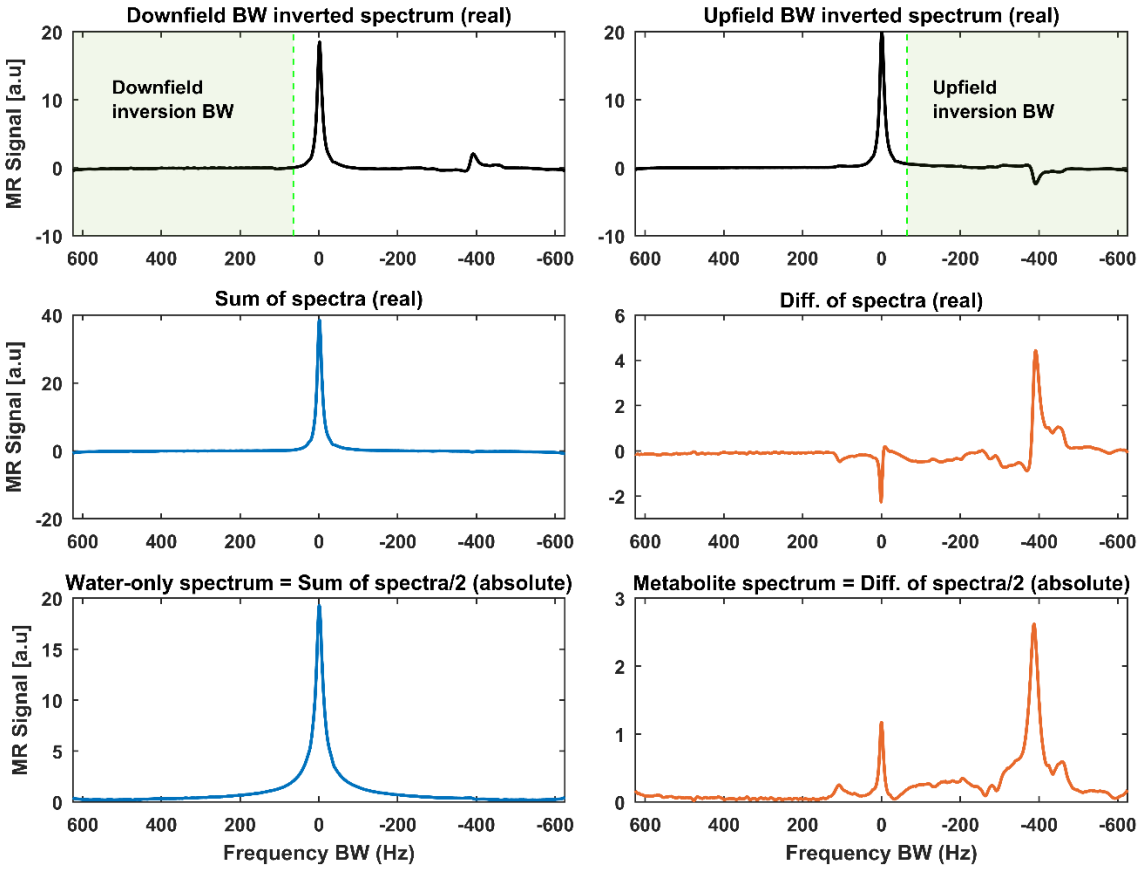

Figure 2.1 Example of how to get water-only and metabolite-only (includes the lipid peaks) spectra using metabolite cycling (MC) acquisition. The MC acquisition technique includes two selective adiabatic inversion RF pulses, each with a transition over the water bandwidth (BW). The first adiabatic pulse inverts the downfield BW relative to the water frequency (top panel, left), while the second one inverts only the metabolites upfield of the water frequency (top panel, right). The sum of these spectra provides a pure water spectrum with a minimal residual metabolite signal (middle panel, left), while their difference gives a pure metabolite spectrum with insignificant residual water (middle panel, right). The final spectra are magnitude spectra divided by two since the summation and subtraction give double the original signal (bottom panel)

2.2.5 Quantification

The Dixon technique provides a water image and a total lipid image. In order to generate a signal fat fraction map out of these Dixon images, the following formula is used:

$$\mathrm{FF}_{Dixon} = \frac{\mathrm{signal}_{\mathrm{lipid}}}{\mathrm{signal}_{Total}} . 100 \qquad (1)$$

Where signal_{Total} = lipid + water images signals. An illustration of signal FF_{Dixon} map reconstruction can be found in Figure 2.2.

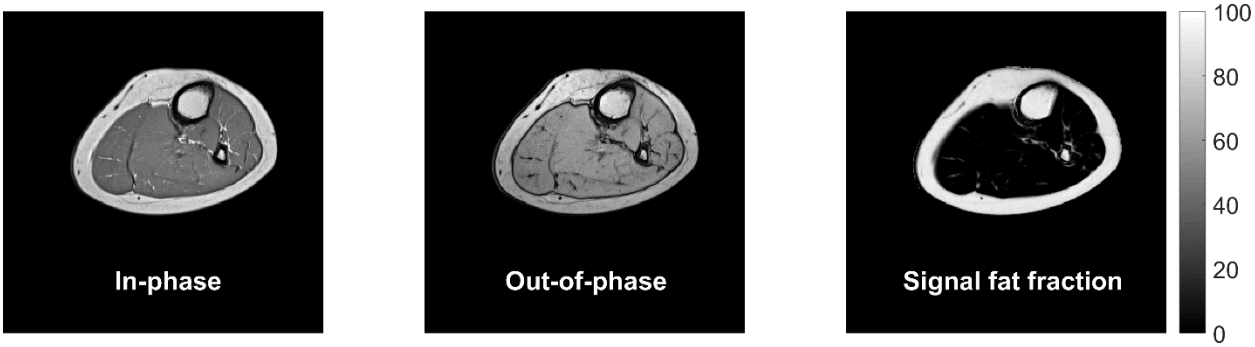

Figure 2.2 Dixon output and signal fat fraction map reconstruction. In order to generate a fat fraction map by the Dixon technique, at least two signal acquisitions are required. Since the strongest fat component, the bulk methylene, has a chemical shift of about 3.5 ppm lower than water, one acquisition is acquired when this fat component is in-phase (IP) with water spins and another acquisition when they are out-of-phase (OP). The signal sum of the IP and OP acquisitions will eliminate most of the fat signal contribution and render double the water signal, and their difference will result in double the fat signal without water signal. By dividing the results by two, images of water-only and fat-only signals are produced. From theses fat/water only images, a signal fat fraction map can be calculated using Equation (1)

As for MRSI, MC FID DW-CRT provides water-only and metabolite-only resonance spectra. Following their spectral post-processing, these spectra from each voxel are passed into LCModel to fit each peak of the spectra individually and return their integrated signal.[89]

In order to avoid phase correction artifacts in areas overwhelmed by lipids such as bone marrow or subcutaneous fat regions, the LCModel phase correction option was set to zero. Instead, the magnitude value was used as previously done by Meisamy et al..[90] In order to correct for the long water T_1 relaxation time effect, the water reference attenuation correction parameter, ATTH2O, in LCModel was used. This parameter was determined based on the T_1 signal relaxation term, 1-exp(-TR/T_1), where the T_1 value of water in skeletal muscle was assigned to 1412 ms as measured by Stanise et al. at 3T.[91] LCModel's basis set of muscle spectra, "muscle-5", was used to fit the magnitude MRSI-spectra. To construct the MRSI maps, only peaks with Cram´er-Rao lower bounds (CRLB) values of 8% or less (measured by LCModel) were used. The FF was then calculated by using a similar expression to that used to calculate the FF_{dixon}:

$$FF_{MRSI} = \frac{\text{signal}_{\text{specific lipid}}}{\text{signal}_{Total}} . 100 \quad (2)$$

For both techniques the water fraction (WF) is calculated by the following formula:

$$WF = \frac{\text{signal}_{\text{water}}}{\text{signal}_{Total}} . 100 \quad (3)$$

In addition, to assess the MC performance within the calf area, the residual water (RW) fraction was calculated as:

$$\text{RW fraction (\%)} = \frac{\text{signal}_{\text{RW}}}{\text{signal}_{\text{water}}} . 100 \quad (4)$$

Where $\text{signal}_{\text{RW}}$ is the signal of the residual water peak within the metabolite-only spectra fitted by the LCModel.

2.2.6 Muscle Segmentation

To assess the spatial FF distribution of each lipid component within the calf muscles, muscles were manually segmented by drawing ROIs over each of the eight main muscles based on their high-resolution T1-weighted image. The ROIs borders were determined by following the muscle boundaries. These ROIs were down-sampled to match MRSI resolution and co-registered to each lipid FF map to assess their distribution voxel-wisely. To avoid any partial volume effect by adjacent structures, voxels on the borders were excluded out of the down-sampled ROIs (Figure 2.3).

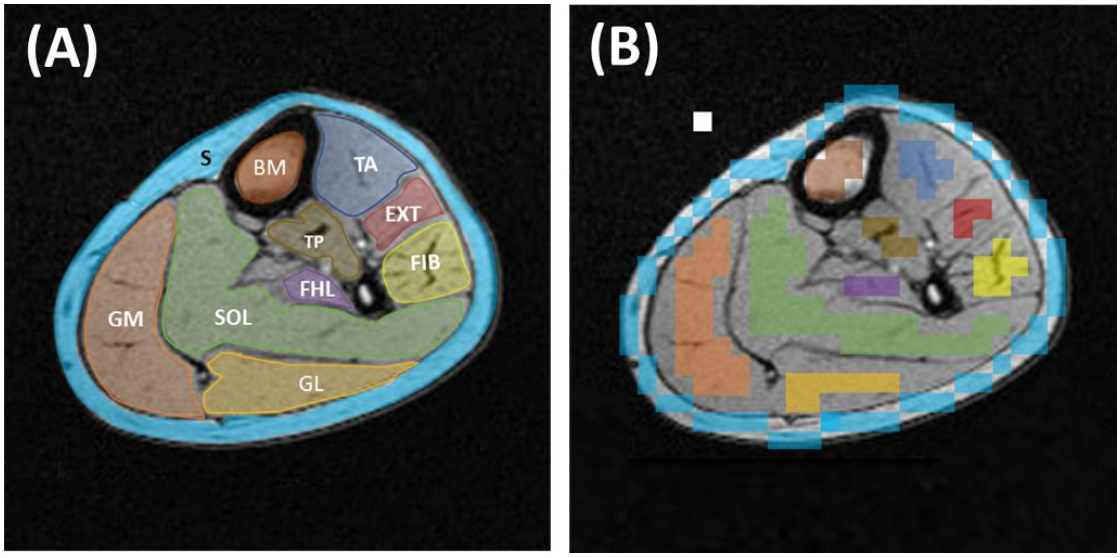

Figure 2.3 A, Calf muscle, bone marrow (BM), and subcutaneous (S) regions of interest (ROIs) drawn on a high-resolution T1 axial image, which provides a good anatomical delineation. Eight ROIs were used to cover the main eight calf muscles. SOL, Soleus muscle; FIB, Fibularis muscles; EXT, Extensor longus muscles; TA, Tibialis anterior muscle; GM, Gastrocnemius medialis muscle; GL, Gastrocnemius lateralis muscle; FHL, Flexor halluces longus muscle; TP, Tibialis posterior muscle. B, The same ROI set after being down-sampled into MRSI resolution and removing the voxels on the muscle borders. The white box represents one ROI voxel

2.2.7 Data Analysis

To compare the results of the two used techniques, the Structural Similarity (SSIM) Index method,[92] implemented in MATLAB, was used to find the level of similarity in fat detectability between the FF maps generated from the MRSI versus those from the Dixon technique. SSIM analysis compares two images and returns their signal intensity and structural similarity level (index) for each voxel as well as a global (mean of all voxels) value. In addition, regression comparisons with ROIs were performed between the FF values measured from the Dixon method data versus the data of the integrated IMCL and EMCL. For comparison, this regression analysis was performed with FF calculated with all eight lipid peaks, and also with only the upfield lipid peaks (methyl and bulk methylene lipid peaks).

Additionally, in order to assess each lipid component FF spatial distribution within the muscles estimated by the proposed MRSI method, the previously segmented muscle ROIs were used with each lipid component FF map. To eliminate outlier voxels from generating false-positive findings, a minimum positive voxel threshold (MPVT = 1/number of subjects = 20% of the ROI voxels from all subjects) was considered. This means that only muscles with enough (i.e., above MPVT) positive voxels (voxels containing the lipid of comparison and passed the CRLB criteria of peak fitting goodness) were included in the regional comparison. To conduct this regional comparison, the Kruskal Wallis one-way analysis of variance test was used to assess the lipid spatial distribution variation and followed by the Bonferroni multiple comparison test to determine whether a significant FF difference exists between any two muscles.

2.3 Results

The phantom study showed that Dixon and MRSI were able to estimate the true FF (see Figure 2.4). The results of the lipid phantom FF in the defined volume of interest were 49.6 ± 9 % measured by MRSI and 47.4 ± 5.4 % by the used Dixon method.

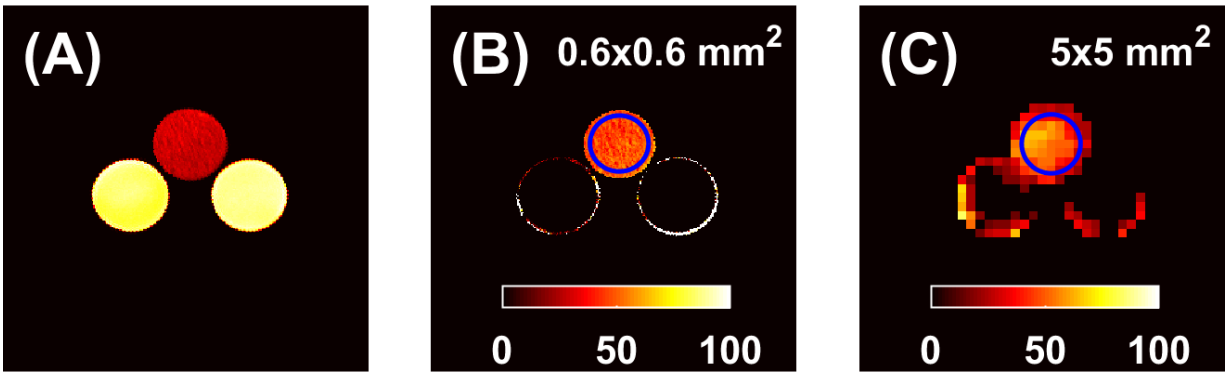

Figure 2.4 A, structural image shows the phantoms setup. B, corresponding Dixon signal fat fraction (FF) map. C, The MRSI total FF map. Both methods were able to estimate the phantom FF. However, the MRSI provided more accurate result (49.6 ± 9 % and 47.4 ± 5.4 % measured by MRSI and Dixon, respectively). The blue circles highlight the region that has been quantified (the bottles border was excluded).

As shown in Figure 2.5, generated water- and lipid-only maps of MC MRSI are in agreement with the anatomical distribution of those provided by the Dixon technique. The proposed MRSI technique further provided separate pure water spectra, and spectra with different lipid components and other metabolites. The generated MRSI spectra were fitted by LCModel, which identified eight lipid peaks found within the metabolite spectra (IMC/L(CH_3), EMCL(CH_3), IMC/L(CH_2)$_n$, EMC/L(CH_2)$_n$, IMC/L(CH_2–CH), EMC/L(CH_2–CH), IMC/L(–CH=CH–), and EMC/L(–CH=CH–)) plus Cr30, Cr39, and Crn32 (see examples in Figure 2.6). In addition to total FF, water fraction, integrated IMCL, and integrated EMCL FF maps (see Figure 2.7), eight separate FF maps of each lipid component were reconstructed (Figure 2.8) from the quantification results by LCModel for the fitted lipid and water peaks. The MC method resulted in only 1.3 ±1.2% RW fraction that was only found in half of the calf voxels (Figure 2.9).

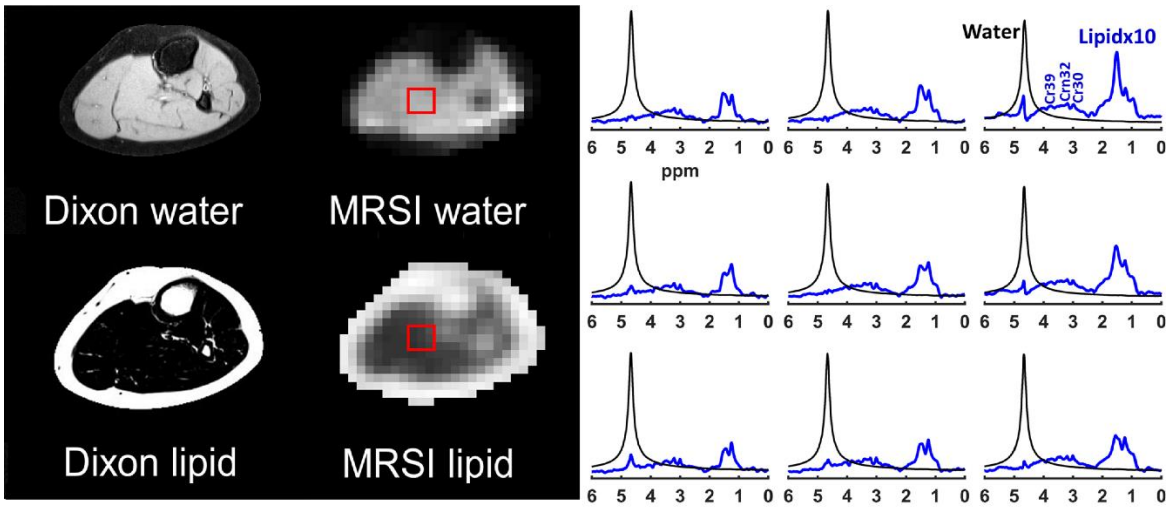

Figure 2.5 Dixon versus MRSI output. The results of the FID density-weighted concentric ring trajectory (DW-CRT) metabolite cycling MRSI sequence are in line with the Dixon images. On the right, representative water (black) and lipid (blue) spectra acquired from the same location (box) by MRSI. The lipid peaks were magnified ten times compared to the water peak for better visualization

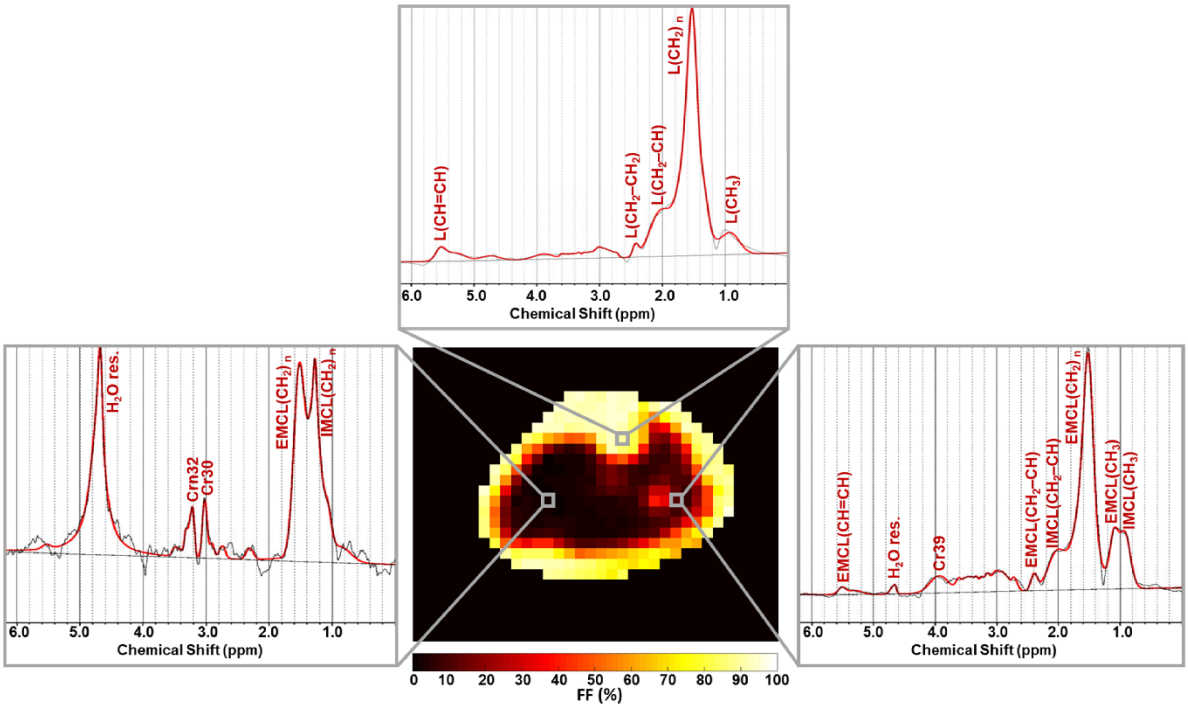

Figure 2.6 Representative spectra fitted by LCModel from different locations in muscles and bone. The shown spectra (black) were acquired from the voxels highlighted on the total fat fraction map. The LCModel fit is shown in red, with the fitted lipid components labeled. H_2O res. stands for the residual water signal. Other metabolites than lipids can also be detected such as CH_3 and CH_2 groups of creatine that resonate at 3.0 ppm (Cr30) and 3.9 ppm (Cr39), respectively, in addition to the CH_3 group of carnitine (Crn32)

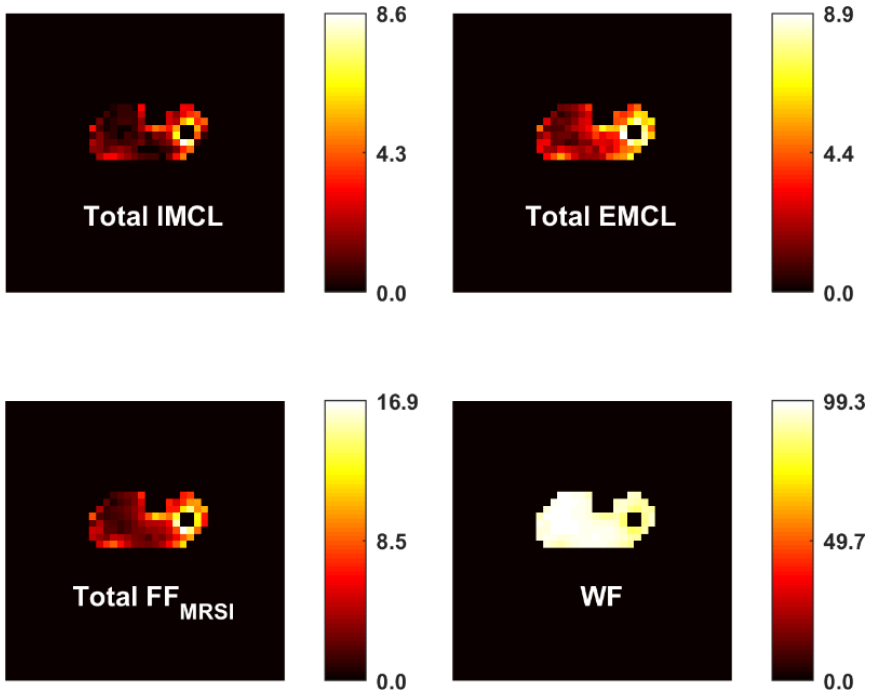

Figure 2.7 Additional to muscles total fat fraction (FF) and water fraction (WF) maps, an integrated intramyocellular lipid (IMCL) peaks map, and integrated extramyocellular lipid (EMCL) peaks FF maps can be generated. These maps showing the ability of the MRSI method to spatially resolve IMCL and EMCL

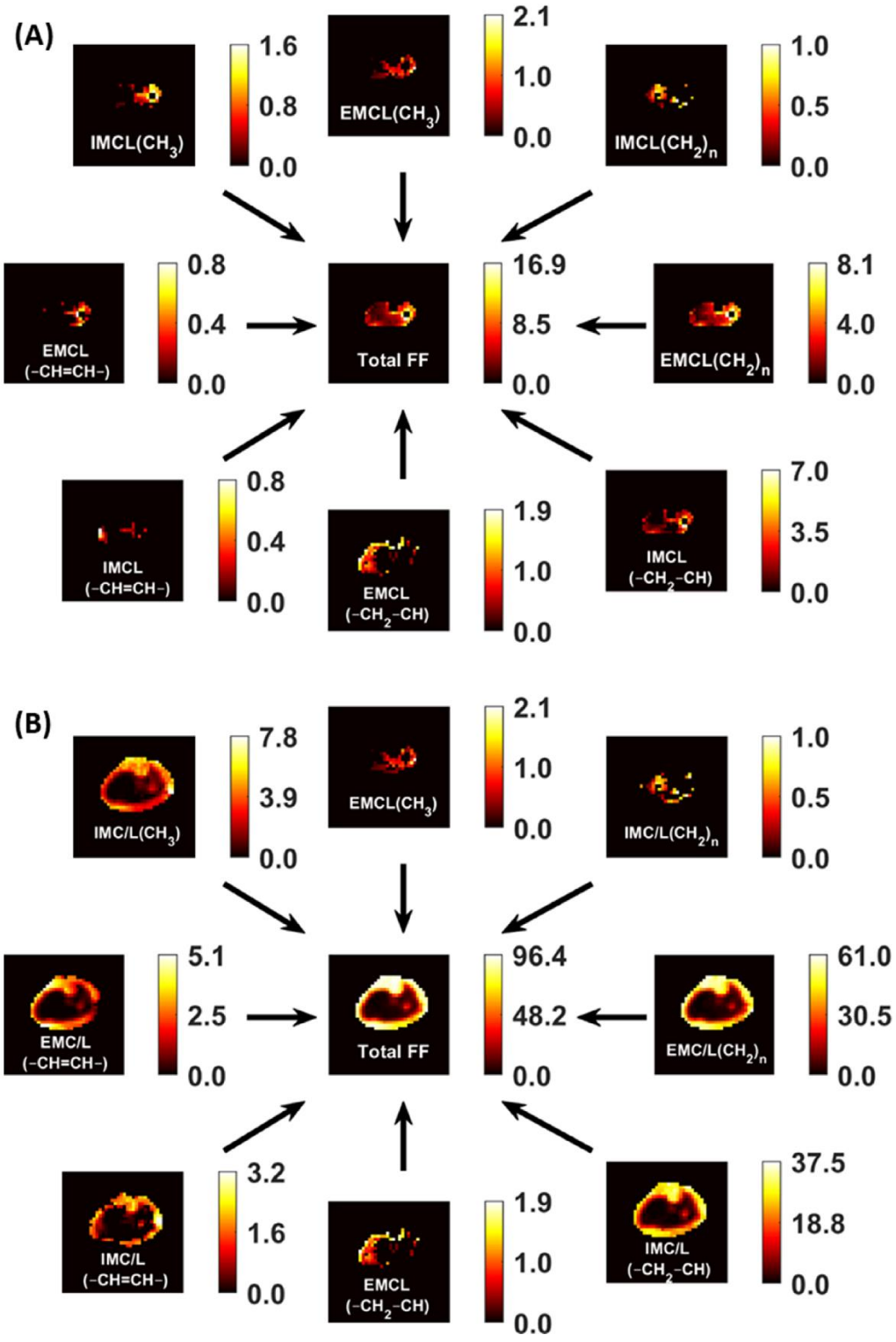

Figure 2.8 Representative fat fraction (FF) maps for each lipid component that was fitted by LCModel. Only results with CRLB of 8% or less were included. The scale next to each map indicates the FF values from 0 to maximum in percent. A, the dominant lipid in the bone and subcutaneous regions were masked to better visualization of the muscle lipid components, which usually have lower contents. B, the same maps without any tissue masking

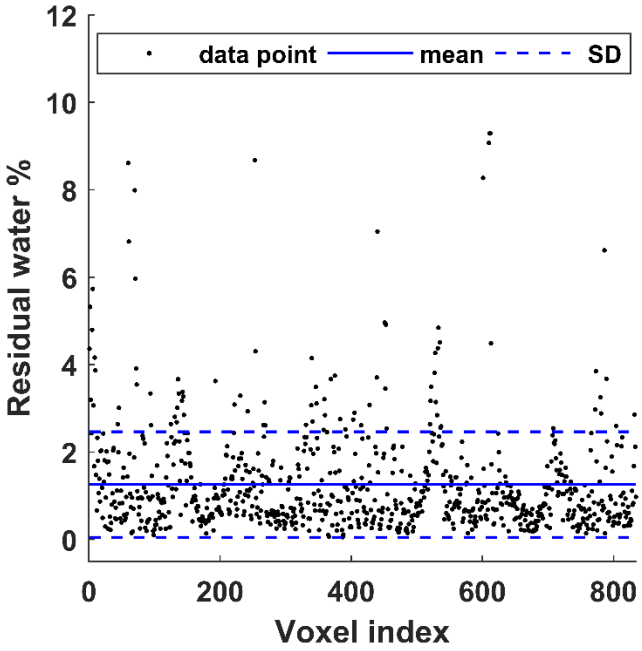

Figure 2.9 Residual water (RW) after implementing the MC. Out of 1626 voxels within the calf area (from the five subjects), the LCModel could fit residual water in 832 voxels with a mean RW fraction of 1.3 ±1.2%

The results of the SSIM analysis comparing the signal FF_{Dixon}-map to each lipid component FF-map generated by MRSI are illustrated in Figure 2.10. The data presented as SSIM index mean ± standard error that was evaluated for all the five scanned subjects. Figure 2.11 demonstrates an example of the SSIM analysis result from one subject's data. The example involved the lipid of the highest signal, the EMC/L$(CH_2)_n$, and the lipid of the lowest signal, the IMC/L$(CH_2)_n$. In this example, the mean SSIM index results from comparing the Dixon technique used in this study to the IMC/L$(CH_2)_n$ results was very low (0.03) compared to the similarity of EMC/L$(CH_2)_n$ (0.59). In fact, the Dixon technique used in this study could not detect IMC/L$(CH_2)_n$ and EMC/L$(CH_2)_n$ in several locations where the MRSI was able to detect considerable signals from these lipid components. For demonstration, in the same figure, spectra from 2 x 2 voxels covering a random area where total mismatching present (SSIM = 0) were shown. This also can be seen from the regression analysis in Figure 2.12, the shaded boxes. The regression analysis in Figure 2.12 also shows that the Dixon values mostly coming from the extramyocellular (EMCL) signal, specifically from the upfield lipid peaks (Figure 2.12, D), which is in-line with earlier reports.[93,94]

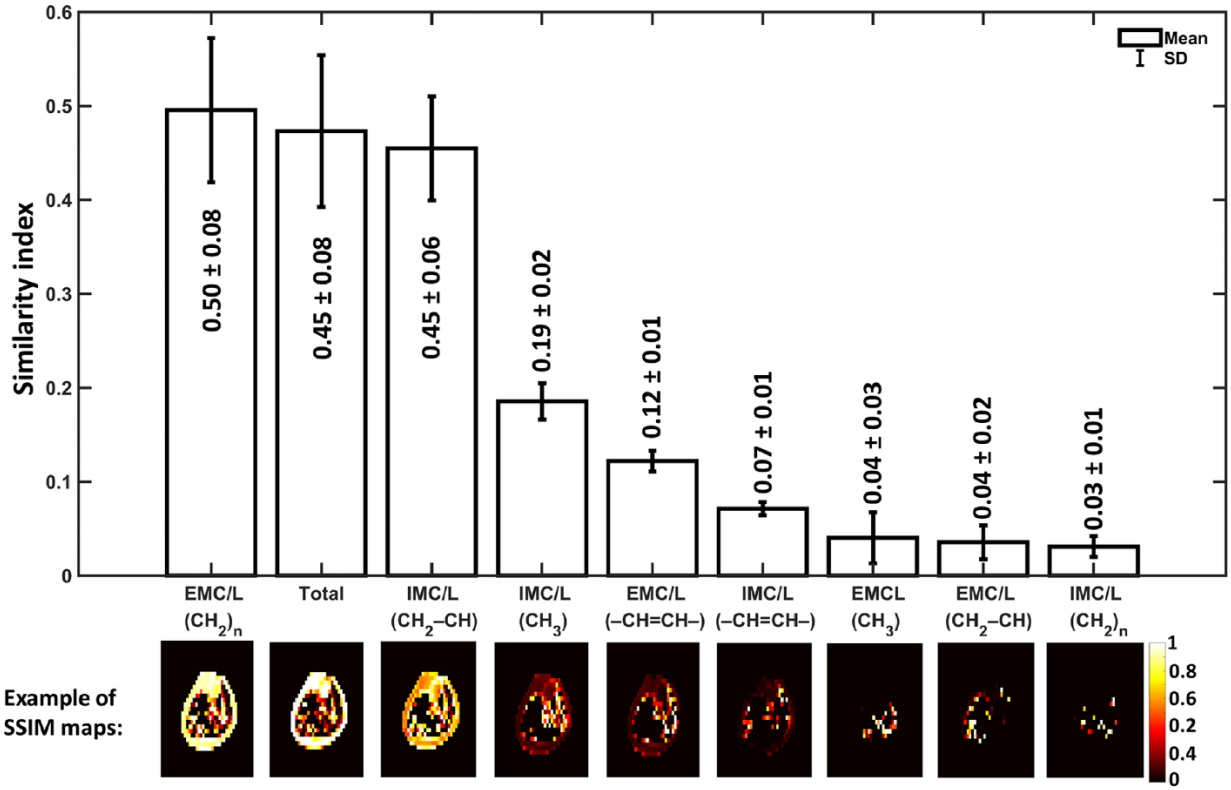

Figure 2.10 Dixon similarity to MRSI maps results. The structural similarity (SSIM) indices mean as a result of comparing the Dixon signal fat fraction (FF) map to the FF-map of each lipid detected by MRSI. The mean and standard error were calculated based on the data from the five healthy subjects. The SSIM indices range between 0 and 1. SSIM=1 represents a perfect similarity. The results are ordered based on their order of similarity from the highest to lowest (left to right). Representative SSIM maps from one subject are depicted below each bar of their corresponding lipid component. The results suggest that Dixon's fat signal is mainly coming from EMC/L$(CH_2)_n$, IMC/L$(CH_2–CH)$, and IMC/L(CH_3)

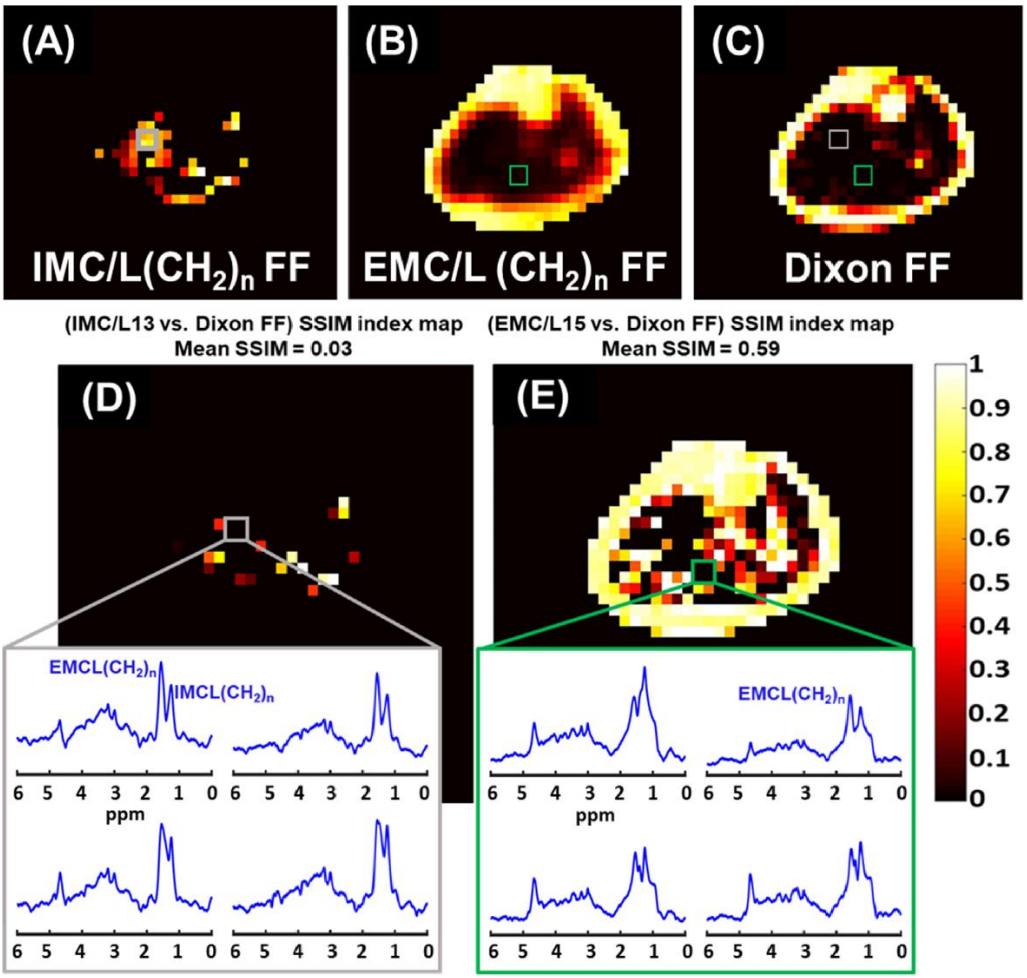

Figure 2.11 Fat fraction (FF) distribution maps of MRSI IMC/L$(CH_2)_n$ (A), EMC/L$(CH_2)_n$ (B), and the Dixon-MRI undifferentiated-fat-fraction image (C). The Dixon MRI image was down-sampled to MRSI resolution for a better comparison. The corresponding SSIM index maps show the structural similarity (SSIM) between the Dixon signal FF image and the MRSI IMC/L$(CH_2)_n$ FF map (D), and the EMC/L$(CH_2)_n$ FF map (E). The mean SSIM value is listed above each SSIM map. The dark areas of SSIM = 0 on the maps (box) represent total mismatching between MRSI and the used Dixon method results. Within these areas, only MRSI could identify lipid peaks

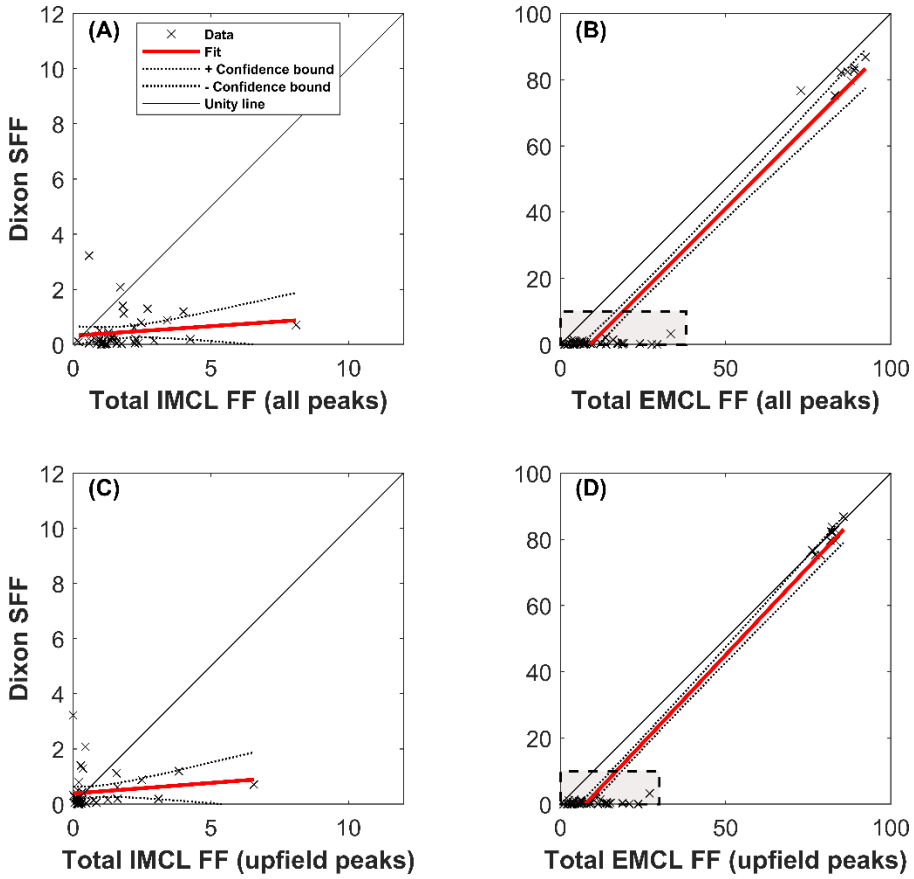

Figure 2.12 Region of interests (ROIs) comparison between the Dixon signal fat fraction (SFF) values versus the integrated intramyocellular lipid (IMCL) and integrated extramyocellular lipid (EMCL) fat fraction (FF) values measured by MRSI with different peak models. Among these comparisons, Dixon data values are closer to the agreement (the unity line) when compared with the integrated EMCL data which suggests that the Dixon signal is mostly coming from EMCL. The correlation agreement increases when only the upfield lipid peaks are used (D) and only for the regions of high FF (subcutaneous and bone ROIs). Muscles ROIs have low FF and MRSI was more sensitive by detecting more lipid signals at these ROIs (shaded boxes)

As shown in Figure 2.13, IMC/L(CH_3) FF was present in all the muscles that were defined in Figure 2.3 except in the GL as IMC/L(CH_3) was detected within less than 20% of its ROI voxels. According to the Kruskal-Wallis (KW) statistics, the FF of IMC/L(CH_3) was highly variable among tested muscles (KW-P < 0.001), and it was significantly lower in GM than in EXT (P < 0.001), FBL and SOL (P < 0.01) based on the multi comparison statistics. For EMCL(CH_3), it existed within less than 20% of the GM voxels. The KW statistics also indicated a very high variation of this lipid among the other muscles (KW-P < 0.001). The EMCL(CH_3) level was significantly lower in TA compared to FHL (P < 0.001), TP (P < 0.01), SOL and FIB (P < 0.05), and it was also lower in GL relative to FHL (P < 0.01). For IMC/L$(CH_2)_n$, the MPVT was exceeded

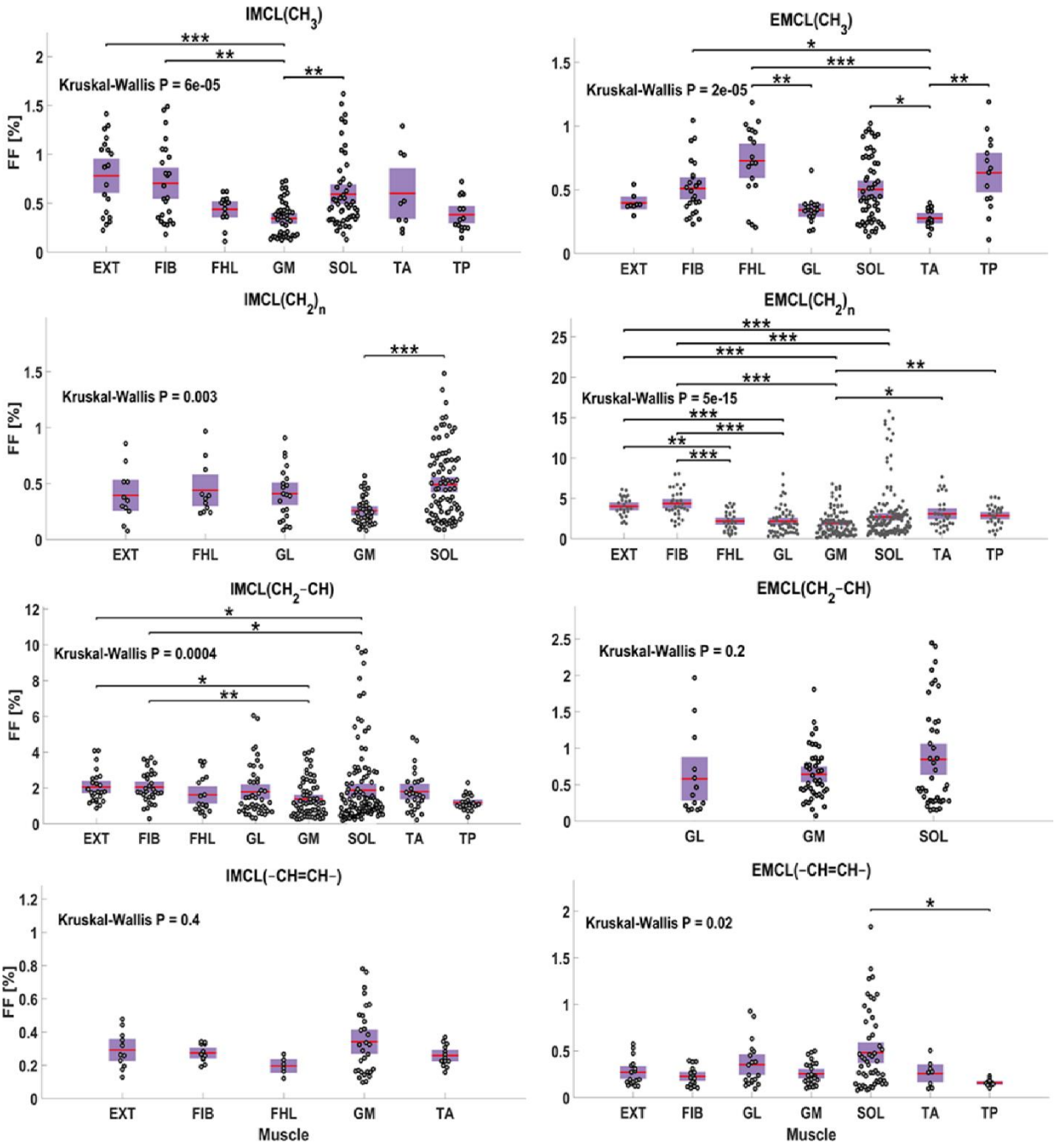

Figure 2.13 Regional comparison of each lipid component fat fraction (FF) distribution within the calf muscles. Each plotted point represents one voxel FF data. Only muscles with at least 20% of their voxels containing the lipid of comparison are included. The *p*-value (*P*) of Kruskal Wallis analysis of variance test is listed for each lipid distribution. The *, **, *** represent $P < 0.05$, $P < 0.01$, and $P < 0.001$ respectively, and are shown when a significant difference exists between any two muscles according to the Bonferroni multi-comparison test

only in five muscles (EXT, FHL, GL, GM, and SOL). Its level among these muscles was only higher in SOL compared to it within GM ($P < 0.001$). On the other hand, EMC/L$(CH_2)_n$ was detected within all the calf muscles with a very large level variation (KW-$P < 0.001$). The multi-comparison analysis detected that EMC/L$(CH_2)_n$ has a higher FF in EXT and FIB compared to GL, GM, and SOL ($P < 0.001$). The EMC/L$(CH_2)_n$ FF was also smaller in FHL compared to FIB ($P < 0.001$) and EXT ($P < 0.01$) and smaller in GM compared to TP ($P < 0.01$) and TA ($P < 0.05$). Similar to EMC/L$(CH_2)_n$, the IMC/L(CH_2–CH) was also detected within all the muscles with a strong FF distribution variability (KW-$P < 0.001$), with a significantly higher FF within FIB than in GM ($P < 0.01$), and SOL ($P < 0.05$), and EXT has higher FF compared to GM and SOL as well ($P < 0.05$). On the other hand, EMC/L(CH_2–CH) was detected with enough voxels larger than the MPVT only in the three muscles located at the posterior part of the leg (GL, GM, and SOL) and without significant FF variation among them (KW-$P = 0.2$). For IMC/L(–CH=CH–), The MPVT was satisfied in only five muscles (EXT, FIB, FHL, GM, and TA) without significant fat level variation (KW-$P = 0.4$). The EMC/L(–CH=CH–) was not above the MPVT for the FHL and GL voxels. Among the other muscles, the EMC/L(–CH=CH–) FF distribution was found to be moderately variable (KW-$P = 0.02$) as only SOL has significantly higher FF of EMC/L(–CH=CH–) relative to TP ($P < 0.05$).

2.4 Discussion

Our proposed technique has a set of advantages. It is fast, which reduces motion artifact, and reduces the MRI acquisition durations. Although this MRSI has lower spatial resolution compared to MRI, it has a high spatial (in term of MRSI) and spectral resolution to reduce the degrading influence of the point spread function and the fiber orientation heterogeneity on spectral quality. Furthermore, it has a short TE relative to the lipid and water T_2 values, so quantification is possible without the need for a T_2 correction. Most importantly, it provides water-only and separate lipid signals simultaneously for more precise FF quantification that eventually reflected in better diagnosing ability. Finally, the water-only spectra are used as an internal reference, to minimize sideband artefacts and to perform voxel-wise post-processing corrections without the need for an extra acquisition.

This work has shown that clinically important lipid components, but of relatively low MR signal such as IMC/L$(CH_2)_n$ are better evaluated by the proposed MRSI method rather than the

imaging technique. This recommendation is based on the findings observed from the SSIM analysis. As demonstrated in the results, the MRSI method showed a better performance identifying those lipid components of lower levels. Such molecules of interest normally have a low signal that is hard to be detected by imaging techniques or overwhelmed by larger signals from other molecules within the same voxel. Indeed, the lipid signal measured by the conventional Dixon techniques mainly originates from the methyl and methylene peaks. This finding agrees with a previous phantom study that showed that the Dixon method provides lower accuracy in quantifying total FF compared with MRS when the signals from all lipid peaks were summed.[94]

The FSE Dixon technique used here is a limitation of this study. Usually, a gradient echo proton density FF Dixon sequence with a shorter TE is used for more accurate FF quantification. However, we used a conventional Dixon technique that is similar to the most common Dixon sequences available with the most clinical scanners. Since we used the body coil, we had to turn off the parallel imaging feature, which resulted in prolonging the scan time. To mitigate the impact of not using the parallel imaging, we used an FSE sequence[95] and adjusted its parameters (by setting the TE to the shortest possible value and using a long TR) to make it closer to a proton-density-weighted sequence. However, the used TE (11 ms) may not be short enough to avoid the potential T_2 influence, especially on the faster-decaying water signal. In addition, J-coupling at a TE of 11 ms might have affected the fat signal decay of the FSE Dixon method.[96,97] Thus, the FF measured by the FSE Dixon method is signal-weighted FF rather than proton density FF. Although that other advanced Dixon techniques were introduced and some of them suggested methods to account for the fat multipeak existence such as the work done by Yu et al.,[98] they are still not independently able to allocate different map for each lipid of interest like the proposed MRSI technique. Indeed, the multipeak modeling approach assumes that peaks have constant relative amplitudes. However, this assumption may not always be applicable. At least within the muscles, the relative peak amplitudes have been noticed to change with exercises and diseases.[99,100]

The phantom study showed that MRSI could provide a more accurate estimation of the true FF compared to the used Dixon method, but with lower precision. However, this lower precision is expected due to the lower spatial response function of the used DW-CRT method with an alpha of 1.[8]

We decided to perform this study on an adolescent population to investigate the lipid distribution in this age group as several studies have conducted a similar assessment but on adult

populations.[41,101,102] Most of these adult studies considered only IMC/L$(CH_2)_n$ and EMC/L$(CH_2)_n$ distribution. Our findings agree with all these previously published studies for IMC/L$(CH_2)_n$. However, for EMC/L$(CH_2)_n$, our findings on adolescents agree only with one study findings[101] that there is no significant variation in EMC/L$(CH_2)_n$ content within SOL and TA. For the other three studies, the EMC/L$(CH_2)_n$ level was always significantly larger in SOL relative to it in TA. Although that our IMC/L$(CH_2)_n$ distribution conclusion matches the published studies, the other studies were able to report values for IMC/L$(CH_2)_n$ level in TA, which usually the lowest among the investigated muscles, but our findings suggest that no IMC/L$(CH_2)_n$ was detected in this muscle. Potential reasons for these contrast in findings could be the age impact as muscles lipid content found to be lower in younger age,[103,104] because some of these studies conducted by using a large SV-MRS, which is more sensitive to the partial volume effect, or MRSI without considering a method to exclude the false positives. In addition, SV-MRS was found to have more variability to reproduce the same measurement compared to MRSI based on the study done by Shen et al.[105] on the TA muscle which can be another potential reason for this difference in findings of this muscle. The uneven distribution of IMC/L$(CH_2)_n$ across muscles was related to the amount of slow-twitch (type I) fibers in the muscles.[41,101] For instance, the majority of SOL fibers are of type I, whereas GM and GL contain more fast-twitch (type II) fibers.[106] In contrast to type II fibers, type I is smaller in diameter, contains more mitochondria, depends less on the ATPase activity to produce energy and thus stores more IMCL for the mitochondrial oxidation process.[106–108] In addition, the functional role[101] and fiber orientation[74] of muscles were suggested as a potential contributor in the lipid content regional differences. Thus, the reason for the contrast of the lipids level among muscles still needs further investigations.

Conducting this research by scanning healthy young subjects was challenging since their tissue fat content is not as high as that in obese people or patients with a condition associated with a fat level increase. Further, using the body coil exacerbate the challenge due to its lower sensitivity. However, our technique could successfully produce high-quality data. Even so, the results can be enhanced further by using a dedicated multiple receive coil. Indeed, by using the scanner-integrated body coil, we showed the feasibility to use it to achieve good spectra while an x-nuclei coil was attached to the scanner for another purpose. Furthermore, the data quality can be increased more by using a shorter TE that helps to reduce the eddy current effect on the smoothness of the spectra baseline.

A summary of the latest MRI/S methods for neuromuscular disease monitoring has been recently published.[109] Within this publication, the importance of advancing quantitative MR-based fat mapping techniques was emphasized. We think that our proposed technique would help the field by providing a different approach to assess fat infiltration diseases. Actually, the importance of this proposed technique can be extended beyond the focus of this work to cover more applications such as quantifying FF in the bone marrow to assess osteoporosis,[29] and Anorexia nervosa,[110] or to assess the intrahepatic lipid in the liver, which is used to evaluate the hepatic steatosis.[111] Nonetheless, our proposed technique can be used to assess physiological change by mapping extra metabolites such as Crn32 that associated with muscle exercises, or maybe implemented to assess choline level to evaluate hepatic and breast tumors.[112–114] Further, this MRSI sequence could fill the need for a fast fat-water separation to provide specific lipid component maps for fatty liver. This need was expressed in a study by Parente et al., where they preferred imaging technique since SV-MRS required a long time, and it may increase the chance of misinterpretation in cases of heterogeneous steatosis.[115] Although that the proposed MRSI method showed its applicability on the calf region, further testing is still required at other prospective body regions. Conducting similar analysis outside the calf region is important to assess this method performance when a potential larger B_0 inhomogeneity may be present which influences the lipid peaks linewidths.

To the best of our knowledge, this is the first time a technique provided to generate separate spatial FF maps for the lipid components. However, the lower spatial resolution of MRSI relative to imaging may be a limitation for some applications. Thus, a technique to improve the MRSI spatial resolution further (within the same acquisition time, or less) would be useful to serve any fat quantification application.

2.5 Conclusions

The proposed MRSI technique provides a needed tool to quantify different lipid components non-invasively. It can reliably detect fat components with high sensitivity and provides pure water information to calculate the FF accurately. Most importantly, it allows reconstructing separate quantitative spatial maps for the lipid components over the entire region of interest within clinically feasible acquisition time, ~ 3 minutes.

CHAPTER 3 : FAST IN VIVO ^{23}NA IMAGING AND T_2^* MAPPING USING ACCELERATED 2D-FID MAGNETIC RESONANCE SPECTROSCOPIC IMAGING AT 3 T: PROOF OF CONCEPT AND RELIABILITY STUDY

Under review with Magnetic Resonance in Medicine

***Ahmad A. Alhulail**, Pingyu Xia, Xin Shen, Miranda Nichols, Srijyotsna Volety, Nicholas Farley, M. Albert Thomas, Armin M Nagel, Ulrike Dydak, Uzay E. Emir*

3.1 Introduction

Sodium (^{23}Na) plays a crucial role in preserving many vital functions in our bodies. Under healthy conditions, ^{23}Na concentration stays within certain ranges but varies among tissue types.[42] The increase in these ranges is a sign of health disorder or physiological changes. In skeletal muscles, the rise in ^{23}Na concentration was used as a biochemical marker for several diseases such as hypertension[49], diabetes,[47] or muscular channelopathies.[48,116] It was also tested for monitoring early therapeutic responses.[51] The physiological changes have also been observed by using ^{23}Na-MR experiments to assess the influence of exercise. An increase in muscle sodium concentration has been noticed after the exercises.[117] In a similar study, this has been suggested to be a result of an increase in the transverse relaxation time (T_2), which eventually led to an increase in the detected MR signal.[118]

^{23}Na possesses 3/2 nuclear spin and its relaxation is determined by the quadrupolar interaction (QI = the interaction between the ^{23}Na nuclear quadrupole moment and the local electric field gradients), and the containing environment.[52,54] In an aqueous solution, the time-averaged QI equals zero, and the spins move freely and tumble very fast. Subsequently, ^{23}Na exhibits a relatively long monoexponential T_2. However, within a biological system, ^{23}Na spins interact with the surrounding macromolecules, and a time averaged QI $\neq 0$ is possible. As the mobility of the ^{23}Na gets more restricted, the transverse relaxation becomes biexponential.[54] The monoexponential relaxation decay within in-vitro aqueous ^{23}Na solutions was estimated to be ranging between 20-50 ms.[53,119] In-vivo, a monoexponential ^{23}Na relaxation of 55-65 ms was also measured within the CSF.[42,120] In human muscles, a fast transverse relaxation time ($T_{2\mathrm{Fast}}^*$) ranges between 0.5–3.0 ms, and slow transverse relaxation time ($T_{2\mathrm{Slow}}^*$) between 12–28 ms were observed.[55] This variation in relaxation modes and magnitude between the in-vivo and in-vitro

environments can cause a T_2 quantification bias if no correction is performed. Similarly, the longitudinal relaxation time (T_1) of ^{23}Na is also short. At 3T, the T_1 of skeletal muscles has been estimated to be about 29 ms.[48] Thus, a careful relaxation measurement is necessary to conduct accurate quantification studies and can also yield useful physiological information.

Within the few conducted in-vivo skeletal muscle studies, the used ^{23}Na-relaxometry techniques suffer either from a limitation in their spatial precision (large voxel covering different tissue types) or from their impractical acquisition time. The intact skeletal muscles T_2^* values have been measured previously using a non-localized FID method.[118,121] Such relaxometry methods estimate the averaged value from a large scanned area, which may include different tissues in addition to the muscles. Moreover, because of this partial volume effect, the estimated value may not be enough to perform a voxel-wise relaxation correction. To achieve the relaxometry study with more spatial precision, a 3D-UTE acquisition technique was used with images acquired at different echo times, which consumes a long scan time (9 min per image), and with a low in-plane spatial resolution (6×6 mm^2).[117] Alternatively, a multi-echo GRE sequence has been used to measure the T_2^* over the entire slice of interest with higher resolution and shorter total time (~14 minutes).[122] However, since GRE starts with a slice-selective gradient, the minimum possible first echo was 1.9 ms, which may not be short enough to detect the fast decaying component of the T_2^*. To allow shorter TEs and avoid the lengthy slice-selective gradients, outer volume suppression (OVS) methods such as single-shot, inversion-recovery based, non-echo (SIRENE)[123] and FIDLOVS[124] have been proposed. However, these methods have not been applied and tested for ^{23}Na imaging.

Therefore, the goal of this work was to develop an accelerated method with an early acquisition start to estimate in vivo T_2^* values of muscle tissues in a voxel-wise manner at 3T while maintaining high spatial and temporal resolution. To attain this, we are proposing an accelerated density-weighted concentric ring trajectory (DW-CRT) MRSI acquisition to measure in vivo ^{23}Na relaxation times in the lower leg muscles with a high sampling frequency. Additionally, to mitigate the long TE limitation when using slice-selective gradients, the SIRENE method[123] was used instead to reach UTE. Before conducting an in-vivo repeatability study, the localization method was tested using simulation and in-vitro experiments.

3.2 Methods

3.2.1 Sequence Design

The sequence begins with a pair of slice-selective gradients and adiabatic full passage inversion pulses (hyperbolic secant (HS20) pulses, B_1 peak of 19.2 μT, a pulse duration of 12.8 ms, and a thickness of 100 mm) applied to invert the magnetization bands outside the desired slice along the z direction and followed by spoiler gradients. After a delay chosen to null the inverted magnetization (TI = ln[2] x tissue's T_1, 20 ms here), pairs of wide-bandwidth adiabatic half passage OVS saturation pulses (HS20, B_1 peak of 29 μT, a pulse duration of 2.56 ms, and thickness of 100 mm) and gradients along z-axis were applied. The net effect is to eliminate the magnetization within the bands at each side of the slice of interest (SOI) along the z direction. The FID is then measured from the remaining magnetization within the SOI after a square excitation pulse of 240 μs duration (see Figure 3.1). To accelerate data collection, the k-space data is collected by using a fast density-weighted concentric ring trajectory (DW-CRT) acquisition similar to that implemented in Chiew et al.[8]

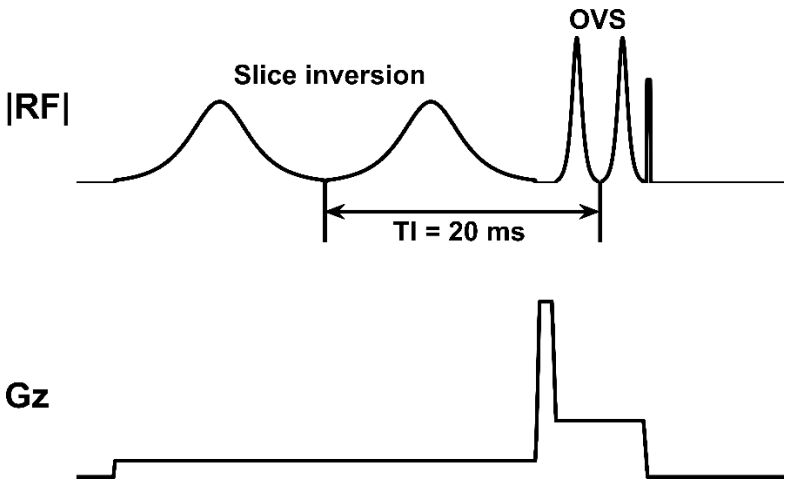

Figure 3.1 Pre-readout MRSI pulse sequence. To suppress the unwanted region outside the slice of interest (SOI), two OVS bands are assigned before the FID excitation. These OVS bands along the z-direction are applied after two selective 180° inversion recovery pulses covering the area outside the SOI at inversion time (TI) = ln(2) x 29 ms = 20 ms, where 29 ms is the muscles T_1.[48] Directly after the OVS band pulses, a nonselective 90° excitation pulse is applied before starting the FID-MRSI readout

3.2.2 Outer Volume Suppression Bands Performance Evaluation

3.2.2.1 Simulation

To evaluate the OVS bands' performance in eliminating the entire ^{23}Na signal outside the SOI, the OVS pulse was simulated on SpinBench (HeartVista, Inc. Menlo Park, CA). Along with the approximated skeletal muscle sodium NMR properties at 3T (gyromagnetic ratio = 11.25 MHz/T, T_1 = 29 ms, fast T_2^* = 0.5 ms, and slow T_2^* = 12 ms), the identical MRSI experimental parameters were used for the simulation software. The resulted thickness, sharpness, and residual signal amplitude over the generated spatial profile were used to judge and optimize the bands' parameters.

3.2.2.2 Phantom experiment

To test the optimized OVS bands parameters on the scanner, a phantom study was conducted. Four phantoms (bottles) were prepared with different known ^{23}Na concentrations (10, 20, 30, 40 mM), which will also serve a reference for the in vivo signal calibration. To mimic the in-vivo T_1 of sodium, 2.9 g/L $CuSO_4$ was added to each phantom.

As demonstrated in Figure 3.2A, to ensure that no signal is coming from outside the SOI, a scan was acquired while two ^{23}Na phantoms of the highest concentration (30 and 40 mM) were placed outside the SOI, within the OVS bands. The remaining phantoms of lower concentration (10 and 20 mM) were placed in the center of the SOI. For comparison, ^{23}Na images with a 3D-MRI sequence scan covering the same SOI thickness were also acquired.

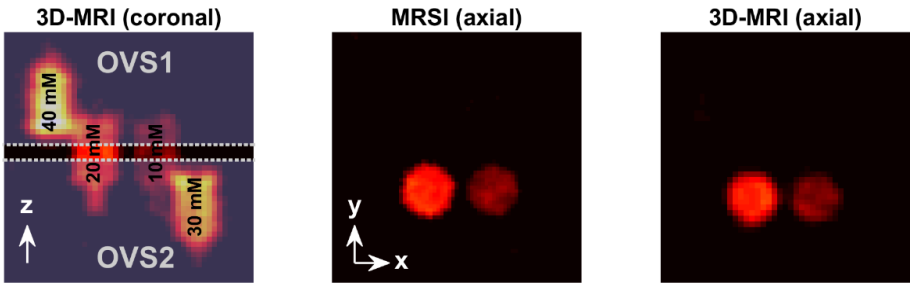

Figure 3.2 Phantom evaluation of the OVS localization. Two ^{23}Na phantoms (10 and 20 mM) were placed at the center of the slice of interest (SOI), which were located between the 2 OVS bands. Two additional phantoms of higher concentrations (30 and 40 mM) were placed outside the SOI, within the OVS bands and away from the center. As shown in the axial images, the MRSI signal is obtained only from the phantoms within the SOI, resulting in an image that is very similar to that produced by the 3D-MRI sequence

3.2.3 In Vivo Experiment

3.2.3.1 Human subjects

In vivo calf muscle scans were performed in four subjects [1 male and 3 females; age 22-40 years (median = 26 years); body mass index (BMI) = 24 ± 3 kg/m^2]. The study was conducted in accordance with the institutional review board of Purdue University. Before being scanned, an informed written consent was obtained from all the subjects.

3.2.3.2 Repeatability study

In order to evaluate the reliability of the proposed MRSI method, test-retest scans were performed. The subjects were asked to lie in a head-first supine position with their left leg within a ^{23}Na coil. The maximum circumference of their lower leg was positioned to be centered in the middle of the coil. Additionally, to make sure that both scans were acquired from the same slice, an ink marker was used to draw a line on the leg region (~10.5-11.5 cm below the knee joint, based on the subject) where the scanner laser was centered for the first scan. After a short break (about 5 minutes) outside of the scanner, the repeat scan was acquired using the same scanning protocol.

3.2.3.3 Scanning parameters

The data were collected using a 3T Siemens Prisma MR system (Siemens Healthineers, Germany) and a frequency-tuned mono-resonant ^{23}Na-transmit/receive birdcage knee coil (32.6 MHz, Stark-Contrast, Erlangen, Germany).

The ^{23}Na data were measured through the default shim currents of the MR system ("Tune Up" under shim settings).

For the ^{23}Na-MRSI study, inversion pulses with TI of 20 ms were applied, followed by the two OVS pulses on the z-direction preceded by the excitation RF pulse. The FID DW-CRT MRSI was implemented with an alpha of 1 (to improve SNR)[8] and the following parameters: matrix size = 96 x 96, field of view (FOV) = 240 x 240 mm^2, resolution = 2.5 x 2.5 x 20 mm^3 (nominal resolution = 0.125 mL), flip angle (FA) = 90^o, acquisition delay (time from the center of excitation pulse to the first FID time point) = 0.55 ms, repetition time (TR) = 650 ms, temporal samples = 64, number of rings = 48, points-per-ring = 64, spectral bandwidth = 312.5 Hz, spatial interleaves

= 4, and readout duration = 204.8 ms. The scan performed with 8 averages, which resulted in a total acquisition time (TA) of 15 minutes and 24 seconds.

For comparison, ^{23}Na-MRI was collected with a density-adapted 3D radial acquisition sequence[125] with UTE = 0.3 ms, TR = 100 ms, FA = 90°, 1 average, 4 × 4 × 4 mm^3 nominal resolution, and FOV = 256 × 256 mm^2, and TA = 6.66 min. Five axial slices were averaged to cover the same MRSI slice. These 3D MRI images will serve as a reference to assess the spatial distribution of the MRSI maps.

To get an anatomical image suitable for segmentation, ^{1}H images were acquired using the integrated body coil with a T_1-FLASH sequence of TR/TE = 250 ms/2.46 ms, FA = 60°, 2 averages, 0.6 × 0.6 × 10 mm^3 resolution, and FOV = 200 × 200 mm^2.

All the above sequences were planned to collect data from the same axial slice placed at the scanner isocenter. Additionally, shimming using the ^{1}H coil was done before the sodium measurements.

3.2.3.4 Post-processing

The reconstruction of the MRSI data were performed in MATLAB (MathWorks, Natick, MA, USA). The gridding and the Fast Fourier Transform were done using the Nonuniform FFT (NUFFT) method.[88] In addition to the DW-CRT trajectory[8], a Hanning filter was applied in k-space for density compensation.

The B_0 inhomogeneity was corrected by calculating the ^{23}Na ΔB_0 maps as described in Gast et al.[126] Here, the ^{23}Na ΔB_0 maps were calculated based on the first two ^{23}Na-MRSI phase-unwrapped images ($\theta_{TE_2,unwrapped}$ and $\theta_{TE_1,unwrapped}$) acquired at TE_1 = 0.55 ms, and TE_2 = 3.75 ms, as follows:

$$\Delta B_0 = \frac{\theta_{TE_2,unwrapped} - \theta_{TE_1,unwrapped}}{TE_2 - TE_1} \quad (1)$$

These ΔB_0 maps were used to reconstruct field-corrected ^{23}Na-MRSI images using a fast iterative image reconstruction method.[127] Finally, we applied low rank approximations for spatial-spectral filtering of reconstructed ^{23}Na MRSI data.[128]

The 3D-MRI data were reconstructed using a MATLAB tool designed for the radial sequence. To reconstruct the 3D-MRI magnitude images, the k-space data were density

compensated before being re-gridded with an oversampling ratio of two using a Kaiser-Bessel kernel,[129] and Fourier transformed by a conventional fast FFT. The data were filtered with a Hanning filter.

3.2.3.5 Fitting of T_2^*

The acquired FID data from the leg region were fitted to a biexponential decay to calculate the $T^*_{2\mathrm{Fast}}$ and $T^*_{2\mathrm{Slow}}$ relaxation time components:

$$SI_{Leg}(t) = S_{Fast}\, e^{-t/T^*_{2\mathrm{Fast}}} + S_{Slow}\, e^{-t/T^*_{2\mathrm{Slow}}} + n \quad (2)$$

Here, S_{Fast} and S_{Slow} are the contributions to the initial signal from the fast and slow components, respectively, *t* indicates the FID points collection time, and *n* represents the offset level.

The initial (undecayed) signal equals the sum of S_{Fast} and S_{Slow}. Thus, their contribution fractions were represented as:

$$F_{Fast} = \frac{S_{Fast}}{S_{Fast} + S_{Slow}} \quad (3)$$

$$F_{Slow} = \frac{S_{Slow}}{S_{Fast} + S_{Slow}} \quad (4)$$

For the reference bottles, *Ref*, the FID curves were fitted to a monoexponential decay:

$$SI_{Ref}(t) = S_{Ref}\, e^{-t/T^*_{2\mathrm{Ref}}} + n \quad (5)$$

3.2.3.6 Quantification

The ^{23}Na concentration maps in mM were reconstructed by calibrating the signals of the reference bottles to their corresponding known concentrations. The resulting signal-to-concentration linear equation was used to calibrate the signals within the leg and to estimate the concentration in mM.

3.2.3.7 Muscle segmentation

To assess the sodium concentration and T_2^* values within the human calf muscles, the high-resolution T1-weighted image was used to manually draw regions of interest (ROIs) over each of the seven main large muscles (Figure 3.3). The borders of these ROIs were determined by tracing the boundaries of their corresponding muscle. Following, The ROIs were down-sampled and co-registered to each sodium map to evaluate the ^{23}Na spatial distribution. Voxels close to the main blood vessels were avoided. The subcutaneous fat region was segmented similarly.

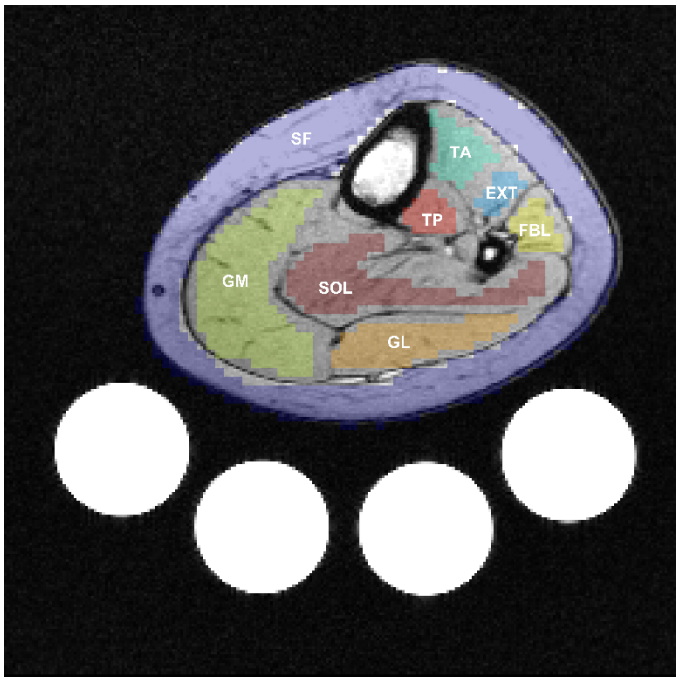

Figure 3.3 Representative segmented regions of interest (ROIs). Calf muscle and subcutaneous fat (SF) ROIs were drawn based on their high-resolution T1 axial ^{1}H-image, which allows clear anatomical features for segmentation. Seven ROIs were drawn to cover the main human calf muscles: SOL, Soleus; FBL, Fibularis; EXT, Extensor longus; TA, Tibialis anterior; GM, Gastrocnemius medialis; GL, Gastrocnemius lateralis; and TP, Tibialis posterior muscles. The shown ROIs are presented in the MRSI resolution and overlaid over their corresponding high-resolution T1 anatomical image

3.2.3.8 Statistical analysis

The Spearman regression analysis was performed to assess the signal spatial distribution agreement between the two used acquisition techniques within the segmented ROIs. The MRSI signals were extrapolated to their estimated values at 0.3 ms to match the TE of 3D-MRI).

To evaluate the repeatability of the MRSI and 3D-MRI methods, coefficient of variance (CV), intraclass correlation coefficient (ICC), and Bland–Altman analyses were utilized.

3.3 Results

3.3.1 Outer Volume Suppression Bands Performance Evaluation

The result of the simulation (Figure 3.4) showed that using a TI of 20 ms within a region of muscle provides a sharp suppression profile. The spatial profile in Figure 3.4 represents the ^{23}Na magnetization after the 90^{o} excitation. While the signal within the OVS bands was totally

suppressed, the magnetization within the SOI has full transverse magnitude and resulted in a slice thickness of 20 mm.

In-line with the simulation, the phantom study demonstrated that the signals from the high ^{23}Na concentration phantoms (30 and 40 mM) placed within the OVS bands were totally suppressed (Figure 3.2B). In contrast, the signals of the low concentration phantoms (10 and 20 mM) within the SOI did not have any contamination and were in agreement with the 3D-MRI sequence (Figure 3.2C).

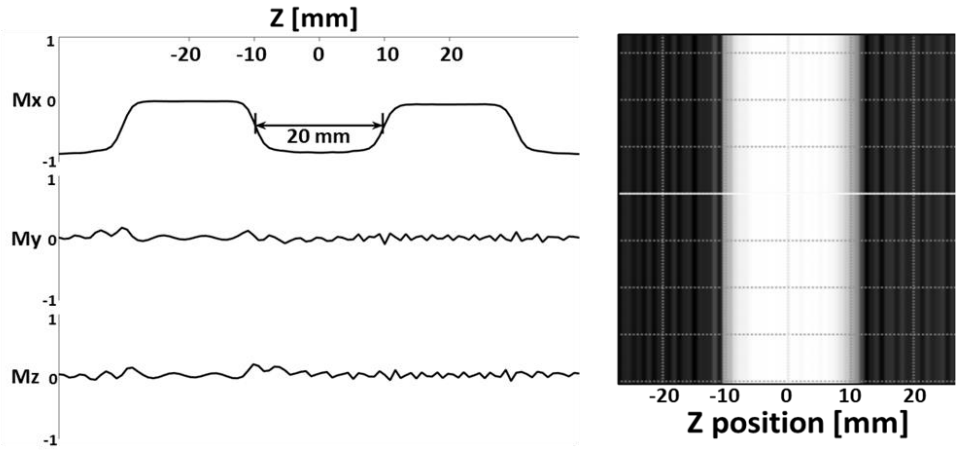

Figure 3.4 Simulated data shows a sharp spatial profile along the z-direction when using an inversion time of 20 ms

3.3.2 In Vivo Experiment

As shown in Figure 3.5, comparison of the ^{23}Na concentration spatial distribution between the MRSI and the 3D MRI (data from 64 muscle and subcutaneous fat ROIs from all subjects) resulted in a regression line of slope = 1.01 that is close to the unity line with a correlation coefficient (r) = 0.7 ($P < 0.001$). Additionally, the Bland–Altman analysis comparing between MRSI and the 3D-MRI showed a bias of 0.7 mM with a CV of 9 % (Figure 3.5D).

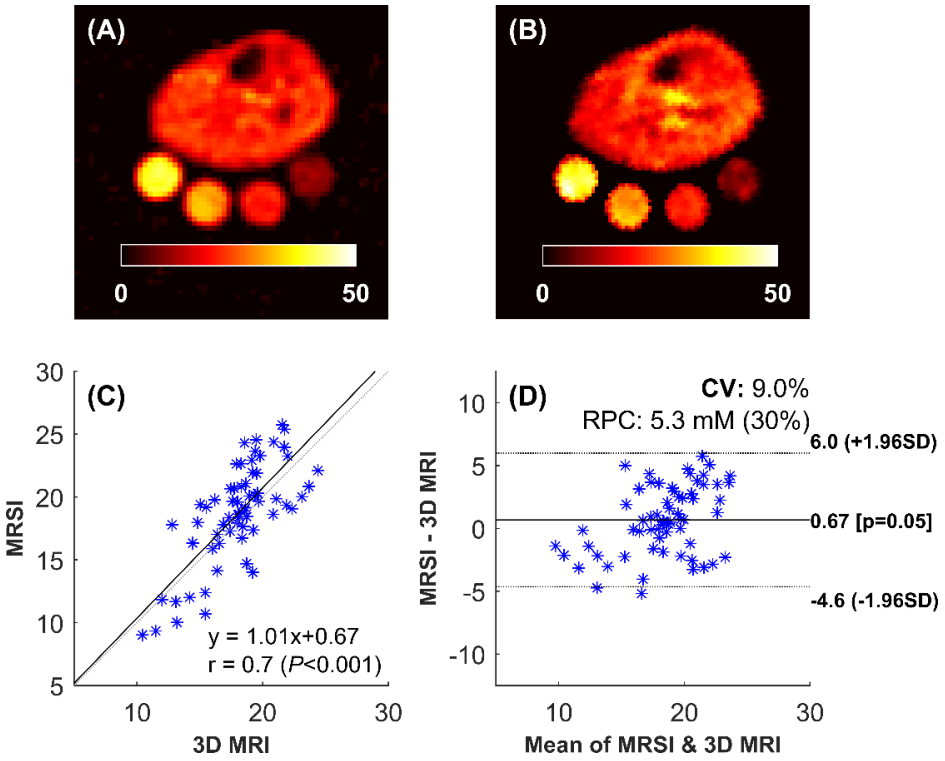

Figure 3.5 Correlation of MRSI with 3D MRI. A, A 3D ^{23}Na-MRI map example. B, A ^{23}Na-MRSI map example for the same subject (the signal was extrapolated to represent data at 0.3 ms, which is the 3D-MRI TE). C, The result of the regression analysis comparing the normalized mean signal (normalized to the phantom signal) of the MRSI and the 3D MRI within 64 regions of interest from all subjects data (7 muscles and one subcutaneous fat ROIs x 4 subjects x 2 scans). D, Bland–Altman analysis comparing the MRSI and the 3D-MRI results

The results of the biexponential T_2^* values (T^*_{2Fast} and T^*_{2Slow}) and their fractions are summarized in Table 3.1, which also includes the T_2^* corrected concentration within each ROI. Fast and slow T_2^*-maps and their corresponding signal fraction maps are illustrated in Figure 3.6. The T_2^* correction was demonstrated by showing sodium maps before and after correction with their difference (Figure 3.7A-C). Additionally, Figure 3.7D shows an example of two signals with similar initial MR signals diverging with time due to their different transverse relaxation in different environments. The ^{23}Na spins decay monoexponentially within the reference phantom (blue) and biexponentially within the muscle (green).

A representative set of baseline and repeated scan maps of the MRSI ^{23}Na concentration (before and after T_2^* correction) and their corresponding 3D-MRI maps are provided in Figure 3.8. The repeatability results of the muscle and subcutaneous fat ROIs from all subjects are shown in

Figure 3.9. The CV was calculated as 4.2, 5.2, and 5.9 %, and the ICC as 0.98, 0.95, and 0.89 for the MRSI data before correction, after correction, and the 3D MRI data, respectively.

Table 3.1 Regions of interest absolute ^{23}Na concentrations, T_2^* values, and signal fractions

ROI	Concentration [mM]	T^*_{2Fast} [ms]	F_{Fast} [%]	T^*_{2Slow} [ms]	F_{Slow} [%]
SF	15.7 ± 1.9	0.71 ± 0.04	38.9 ± 1.5	13.2 ± 0.1	61.1 ± 1.5
GM	25.0 ± 2.8	0.67 ± 0.03	38.3 ± 2.1	13.2 ± 0.4	61.7 ± 2.1
TA	25.3 ± 2.1	0.61 ± 0.09	34.9 ± 2.1	12.9 ± 0.4	65.0 ± 2.1
EXT	26.9 ± 3.5	0.62 ± 0.19	35.8 ± 2.8	13.0 ± 0.5	64.2 ± 2.8
GL	28.6 ± 3.1	0.73 ± 0.06	38.6 ± 0.9	13.1 ± 0.2	61.4 ± 0.9
TP	29.5 ± 2.3	0.73 ± 0.21	37.8 ± 3.4	13.3 ± 0.5	62.2 ± 3.4
FBL	31.1 ± 3.4	0.59 ± 0.14	34.8 ± 2.8	13.3 ± 0.6	65.2 ± 2.8
SOL	34.1 ± 2.2	0.76 ± 0.11	38.4 ± 2.8	13.3 ± 0.4	61.6 ± 2.8
Phantom	10 - 40	---	---	29.5 ± 0.3	100.0

Abbreviations: SF, Subcutaneous fat; GM, Gastrocnemius medialis muscle; TA, Tibialis anterior muscle; EXT, Extensor longus muscles; GL, Gastrocnemius lateralis muscle; TP, Tibialis posterior muscle; FBL, Fibularis muscles; SOL, Soleus muscle. F_{Fast}, The fraction of fast decaying signal; F_{Slow}, The fraction of slow decaying signal.

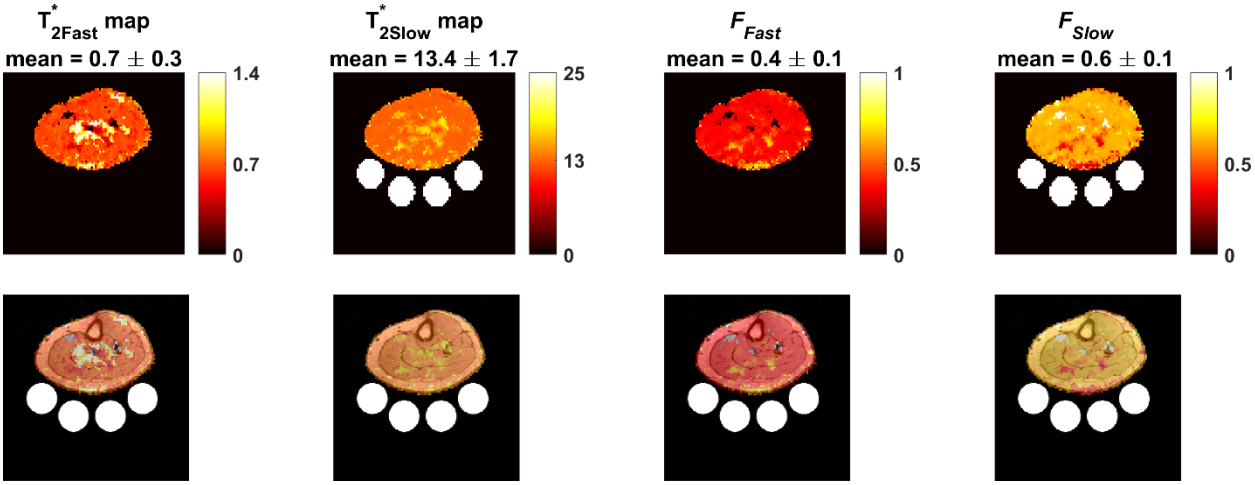

Figure 3.6 Representative relaxation maps. Top panel: fast and slow T_2^* maps, and their corresponding signal fraction (F_{fast}, and F_{slow}). Their mean values from the entire leg slice (without the bottles) are listed above their maps. Bottom panel: the same maps overlaid on their anatomical images

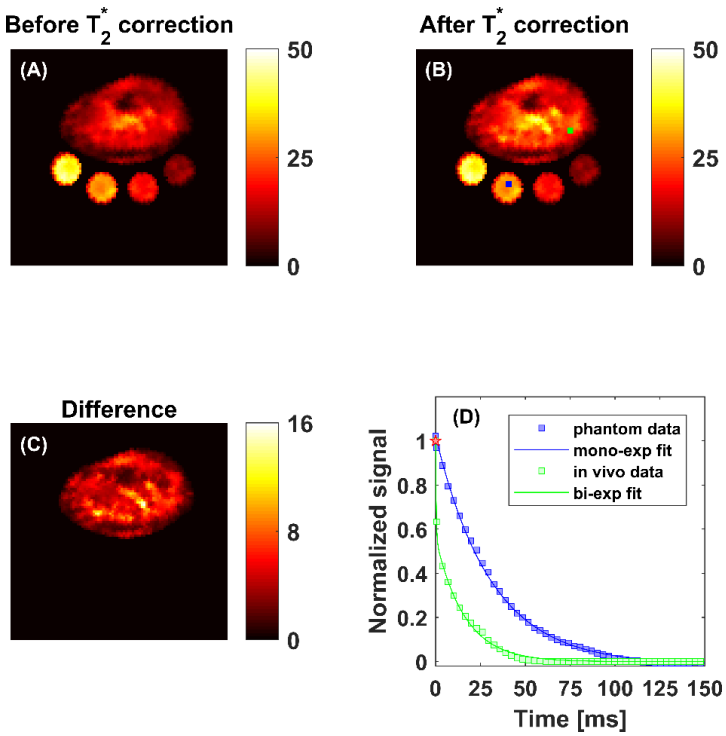

Figure 3.7 Illustrations of the importance of the relaxation correction. The difference between the data acquired at 0.55 ms (A) and the data after correction (B), shows a large improvement in concentration estimation. In the difference map (C), about 5 mM difference in muscles was found. The red star (D) represents the proton density signal corresponding to 30 mM absolute concentration. The fitting example of leg voxel (green box, B and D) and quantification reference voxel (blue box, B and D) with this absolute concentration shows how their signal can diverge with time before fully decaying

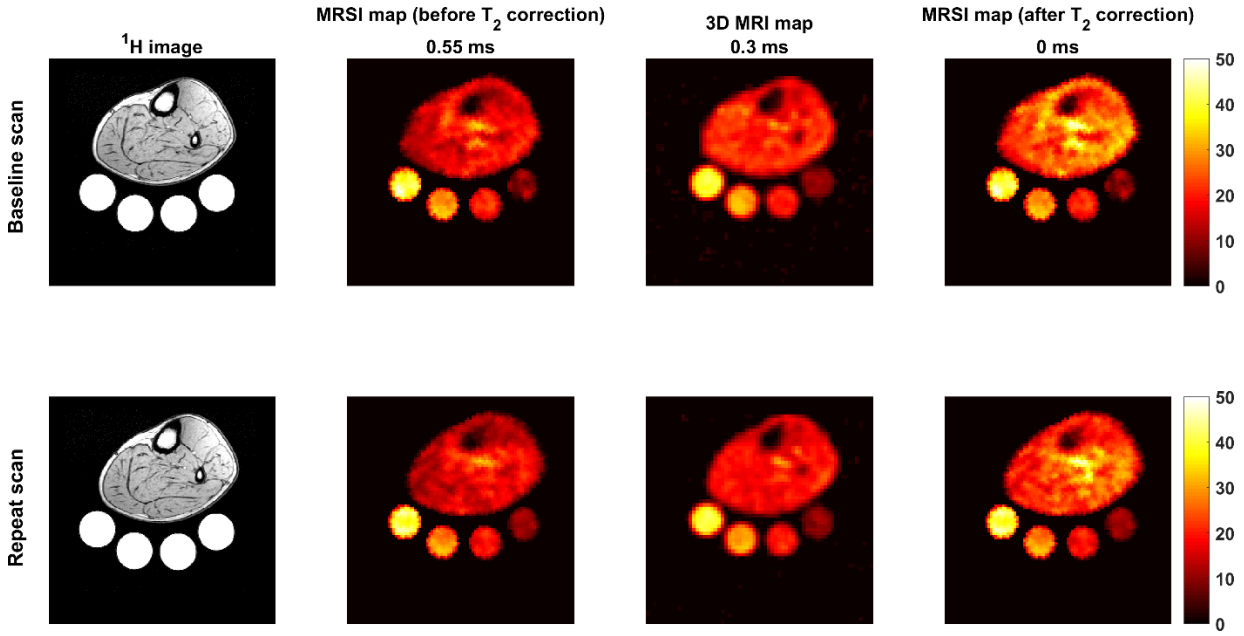

Figure 3.8 Data example of baseline and repeat scans

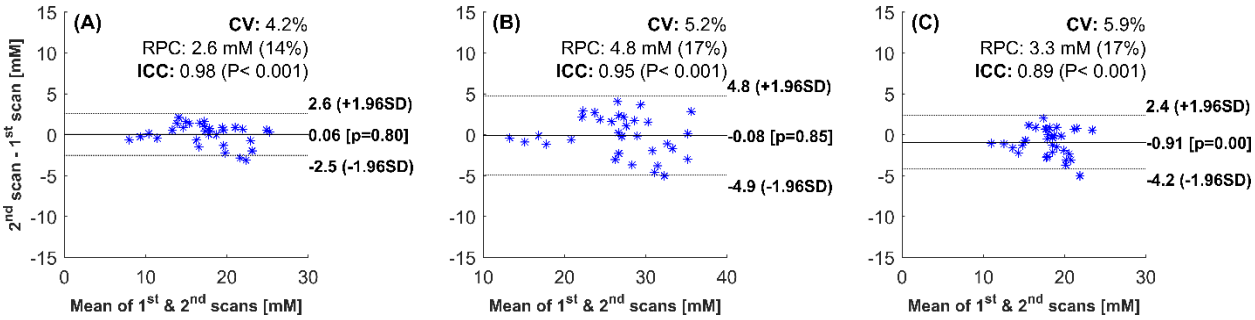

Figure 3.9 Evaluation of repeatability by Bland–Altman analysis. A, The results from the MRSI data before T_2^* correction. B, The results from the MRSI data after the T_2^* correction. C, The 3D-MRI data results. The graphs represent the variability of the measured data (muscles and subcutaneous fat ROIs from all subjects, 7 muscles and one subcutaneous fat ROIs x 4 subjects) between 1st and 2nd scans. The coefficient of variance (CV), reproducibility coefficient (RPC), systematic bias, and intraclass correlation coefficient (ICC) values are listed on each plot

3.4 Discussion

In this work, we have introduced a novel method to acquire ^{23}Na 2D-FID data with short acquisition delay (0.55 ms) with a good quality comparable to a well-established 3D acquisition method. The proposed method provides additional time points in the FID to calculate the T_2^* and correct for its effects.

To reduce the delay time while performing a 2D-measurement, we utilized a single-shot, inversion-recovery based, non-echo (SIRENE) method based on OVS bands[123]. In this study, we implemented the technique with a novel accelerated k-space trajectory, DW-CRT,[8] and showed its feasibility for the ^{23}Na acquisition. The simulation and phantom studies showed that the proposed technique could be used as an alternative to the slice-selective gradient approach in which achieving an ultra-short TE is difficult.

Considering the variation in the parameters of the MRSI and the 3D-MRI sequences, the spatial distribution of their signal was in a good agreement (Figure 3.5C) with a small bias of 0.67 mM that was found with a 9 % CV. This variability between the two sequences results is expected due to their different spatial resolution (MRSI: 2.5 × 2.5 mm^2; 3D-MRI: 4 × 4 mm^2), and spatial response function.[8,125] Moreover, the field inhomogeneitiy correction was only performed on the MRSI reconstruction. A recent study with a similar 3D sequence, but with double echo to measure B_0 and correct for its inhomogeneity at 3T, showed a small enhancement in the results.[130]

In this work, we provided an accelerated technique to conduct voxel-wise T_2^* measurements within an acceptable scan time (15 minutes) while maintaining the spatial quality.

It is worth mentioning that recently a number of studies have shown the feasibility of voxel-wise T_2^* mapping in the brain using UTE 3D acquisition techniques.[131–135] However, these techniques were conducted with fewer time points (8-38 echoes), and require long acquisition times (26 min - 1 h). Moreover, many of these methods were either done with lower spatial resolution, at a higher magnetic field, or done with both. If our proposed MRSI method was applied under these conditions, further reduction in scan time can be achieved.

The estimated mean muscle relaxation times ($T^*_{2\mathrm{Fast}}$ = 0.7 ± 0.1 ms of F_{Fast} = 37 ± 2 %; $T^*_{2\mathrm{Slow}}$ = 13.2 ± 0.2 ms of F_{Slow}= 63 ± 2 %) are in line with previously reported values measured using single voxel ^{23}Na MRS ($T^*_{2\mathrm{Fast}}$ = 0.8 ± 0.2 [32 ± 7 %], $T^*_{2\mathrm{Slow}}$ = 12.4 ± 1.8 ms [68 ± 7 %]).[121] The average muscle absolute concentration (after T_2^* correction) was 28.6 ± 3.3 mM, which is also in agreement with reported biopsy results.[117] In terms of T_2^* spatial distribution, the slow fraction is larger and slower in areas with large blood vessel, which makes sense. In blood vessels, the motion is less restricted compared to muscles and spins move more freely that resulting in longer T_2^* values and the time averaged QI is minimal, which means that the fast component fraction is also minimal.

One can conclude at least two important reasons for performing a relaxation study. First, relaxation corrected data provides a better estimation of absolute concentration, as shown by better agreement with biopsy results (see the preceding paragraph). In Figure 3.7, it has been shown that concentration was increased after the correction. Additionally, one can see that even with UTE measurement, a relaxation bias might be present due to the difference in decay mode within the reference bottles. The second use of T_2^* mapping is the extra information that can be utilized to assess potential physiological changes. Nevertheless, one needs to be aware that voxel-wise T_2 correction may also result in overestimating ^{23}Na concentrations in limited regions, where a hard to avoid partial volume effect exists. This was seen in this study in areas where the main blood vessels start bifurcating to smaller vessels (see the regions of very large difference in Figure 3.7C).

According to the repeatability analysis, the proposed method showed high repeatability (CV = 4%, ICC = 0.98). The repeatability CV and ICC after T_2^* correction were close to the 3D MRI results (CV = 5%, ICC = 0.95 vs CV = 6% and ICC = 0.89). Thus, the proposed MRSI might be a potential method to estimate the T_2^* values and the absolute sodium concentration (free from T_2^* bias) within a reasonable scan time. Since ^{23}Na signal suffers from low SNR, with longer data acquisition, scanning with large voxels or at high fields is performed to maintain good SNR within

a reasonable scan time. Compared to other techniques at 3T, the proposed MRSI method acquires 64 data points with an acceptable spatial resolution (2.5 mm^2, nominal in-plane) and acquisition time (15 minutes and 24 seconds). Since the FID data acquired at different time points with different phases, ΔB_0 correction is also feasible with this method without extra scans. To ensure a proper biexponential fitting for T_2^* estimation, the prolonged acquisition sampling duration allows for acquisition of the entire FID. This is important for areas of longer T_2^* values like reference phantoms.

A limitation of this method is its large dependency on the T_1 value of the scanned tissues. In order for the OVS to perform correctly, the sequence needed to be applied with TI = ln(2) × tissue's T_1 (close approximation when $TR>>T_1$). In this study, we used a TI of 20 ms because muscles have a ^{23}Na T_1 of 29 ms, as previously measured at 3T.[48] To suppress tissues with shorter T_1, such as cartilages, the TI has to be reduced, which may be technically challenging. However, one can make sure that no such tissues are within the active region of the receiving coil. For instance, we avoided getting residual signals from the knee by keeping it outside the ^{23}Na-coil field. Here, we evaluated the technique in healthy muscles. However, T_1 might change with diseases. Although it is expected that this OVS technique would still achieve good suppression even with slightly T_1 deviations, future studies might be needed to confirm this. In this study, no ΔB_1 correction was implemented. However, the coil ΔB_1 mapping was performed using a GRE sequence with the double angel method.[136] Since the ΔB_1 map was very homogeneous, no ΔB_1 correction was conducted. The ^{23}Na-coil ΔB_1 map can be found in Figure 3.10. Although the sample size may be a limitation in this study, there is no reason to anticipate a large difference in our results with larger sample size.

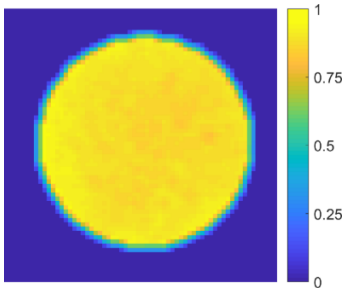

Figure 3.10 Sodium coil B_1 map. The map was generated using a ^{23}Na-GRE sequence and the double angle method. A large phantom (15 cm diameter, 300 mM) was scanned with TE/TR: 1.9 ms/120 ms, FA: 45°/90°, 224 averages, resolution: 3×3×30 mm^3, FOV: 192x192 mm^2. The normalized B_1 map is very homogeneous. Thus, no B_1 correction was performed

For this study, we used a volume coil placed along the z-axis of the scanner. Thus, the spatial B_1 variation is expected to increase along the z-direction, where the OVS bands are applied. Together with inversion pulses, OVS bands make the reduction of the longitudinal magnetization depends mainly on the T_1 and is independent of spatial B_1 variations. Additionally, the broad-BW OVS pulses were applied with a B_1 peak of 29 μT, 2.56 ms duration, and a thickness of 100 mm that resulted in no SAR issues.

The considerable regional variability within T_2^*, their fraction maps, and the increased accuracy of concentration maps demonstrate the potential for future characterization of ^{23}Na in conditions such as muscle diseases, diabetes, cancers, strokes, cartilage degeneration, and to evaluate physiological interventions. The reduction in scan time will increase the technique's availability and reduce motion artifacts. Technically, while still using a long enough TR (4-5 times T_1), a shorter TR than that used in this study can be used, which will accelerate the acquisition further. In addition to insuring a full T_1 recovery and maintaining a low SAR, we used a very long TR because we wanted to study the existence of any long decaying species. However, no such decay has been noticed within the scanned area. Thus, we would suggest using a TR of about half of the value used here. Additionally, scanning with shorter TEs, and with higher sampling frequency could enhance the fitting quality further.

3.5 Conclusions

The proposed method allows fast data collection for measuring sodium concentrations and T_2^* values at high repeatability. This may facilitate evaluating pathological and physiological changes related to the ^{23}Na concentration and T_2^* values within a clinically feasible time, and with a good spatial resolution at 3T.

CHAPTER 4 : STUDYING THE RELATION BETWEEN IMCL, EMCL, AND ^{23}NA CONCENTRATION WITHIN HEALTHY SKELETAL MUSCLES MEASURED BY MRSI

4.1 Introduction

Sodium (^{23}Na) and lipid (triglycerides) are essential components within our body. They take part in maintaining many vital functionalities. However, an elevation of their tissue concentration is a sign of metabolic disruption. The accumulation of musculoskeletal lipids has been linked to type 2 diabetes,[58] hypertension,[137] and Duchenne muscular dystrophy.[17] In separate studies, the increase of muscle ^{23}Na concentration (MSC) was related to these health problems as well.[47,49,138] Furthermore, a physiological situation changer, such as exercise, has been found to raise the content of ^{23}Na and intramyocellular lipid (IMCL) in independent lipid[28] and ^{23}Na studies.[62] Although no correlation analysis was conducted, a recent MRI study showed that the lower leg ^{23}Na and total FF are both increased in lipedema, which allows for differentiating it from obesity (lipedema is commonly misdiagnosed as obesity).[139] In one study that we found with correlation analysis, a positive correlation was found between the total FF and ^{23}Na concentration in muscular periodic paralyses patients.[60]

The reported similar increase of muscle ^{23}Na and lipid level under the same conditions is a strong motivation to further study the relationship of ^{23}Na and lipid components within one study. Additionally, it is crucial to know whether a potential correlation presents in healthy muscles as well, or not. Furthermore, comparing specific lipid components is required, as many health changes have been related to only the IMCL level rather than the total fat level. To perform such a correlation study, robust measurement tools providing comparable ^{23}Na and lipid components data are needed. However, the quantifying methods for lipids are usually either unable to differentiate lipid components, are invasive, cover a limited region of interest, or require a long measuring time.[140] On the other hand, ^{23}Na is usually quantified using an invasive biopsy, using a urine sample,[141] which is not representative of the MSC, or quantified noninvasively by MRI. MRI is the most suitable tool for MSC quantification. Still, most available ^{23}Na-MRI sequences provide T_2^* biased results, which underestimate the actual concentration or require very long scan times to collect enough data to account for the T_2^* bias.

Therefore, the aim of this study is to study the correlation between ^{23}Na and lipid components (including IMCL) in healthy skeletal muscles. To facilitate this study, we will use our recently optimized magnetic resonance spectroscopic imaging (MRSI) methods that allow separate maps of IMCL fat fraction (FF), extramyocellular lipids (EMCL) FF (Chapter 2),[140] and absolute sodium concentration (Chapter 3) within a clinically feasible acquisition time. Further, the influence of gender, age, and body mass index (BMI) factors will be considered.

4.2 Methods

4.2.1 Human Subjects

In vivo magnetic resonance scans were performed on 16 healthy non-obese Caucasian volunteers: 8 males [age 9-26 years; BMI = 20 ± 4 kg/m^2], and 8 females [age 12-32 years; BMI = 21 ± 3 kg/m^2]. The calf muscle scans were measured at the maximum circumference of the lower leg. All subjects stated that they did not exercise for at least 24 hours before their scan. The study was approved by the institutional review board of Purdue University. Before being scanned, informed written consent or assent was obtained from all subjects, and written consent was obtained from the parents of any adolescent subjects. Exclusion criteria include elevated blood pressure, muscle diseases, kidney problems, diabetes, the use of diuretics or attention-deficit hyperactivity disorder medications, and intense exercises within 24 hours before the MR scan.

4.2.2 Scanning Parameters

MRI data was collected using a Siemens Prisma 3T MR system (Siemens, Germany). The anatomical images and lipid maps were acquired using the integrated body coil of the scanner. ^{23}Na data were acquired with a dedicated ^{23}Na transmit/receive knee coil (32.6 MHz, Stark-Contrast, Erlangen, Germany).

For lipid data, a metabolite cycling (MC) MRSI sequence was implemented as described in Chapter 2[140]: field of view (FOV) = 240 × 240 mm^2, matrix size = 48 × 48, acquisition delay = 4 ms, repetition time (TR) = 1 s, flip angle (FA) = 90^o, number of averages = 1, temporal samples = 512, in-plane nominal spatial resolution = 5 × 5 mm^2, and spectral bandwidth (SBW) = 1250 Hz. The total acquisition time was = 3 minutes and 16 seconds.

To reduce any potential bias that may arise from using different measurement methods, the ^{23}Na data was collected using a similar MRSI sequence and parameters: FOV 240 × 240 mm^2, matrix size 48 × 48, acquisition delay = 4 ms, TR = 1 s, FA = 90^o, temporal samples = 512, in-plane nominal spatial resolution = 5 × 5 mm^2. Since ^{23}Na suffers from lower SNR relative to lipids, more averages (8) were prescribed. Additionally, the SBW was reduced to 625 Hz, as sodium does not need as large a SBW to cover its peaks as the lipid experiment. This resulted in a total acquisition duration of 12 minutes and 48 seconds.

For segmentation, a high-resolution anatomical image was acquired with a T_1-FLASH sequence with TE = 2.46 ms, TR= 250 ms, FA = 60^o, number of averages = 2, spatial resolution = 0.6 × 0.6 mm^2, and FOV = 200 × 200 mm^2.

All the acquired data were from the same axial slice centered at the isocenter.

4.2.3 MRSI Post-processing and Quantification

The lipid and sodium MRSI data were reconstructed in MATLAB (MathWorks, Natick, MA, USA). The gridding and the Fast Fourier Transform were conducted by using the Nonuniform FFT (NUFFT) method.[88]

The lipid data were processed as described in Chapter 2[140] to get the water-only and metabolite-only resonance spectra. Spectra from each voxel were passed into LCModel[89] to fit the individual IMCL, EMCL, and water peaks and integrate their differentiated signal. LCModel's basis set of muscle spectra, "muscle-5", was used as a reference to fit the lipid peaks. The ATTH2O parameter (= 1-exp(-TR/T_1)) in LCModel was used to correct for the long T_1 relaxation time of water signal (1412 ms at 3T)[91] before fitting it. To avoid falsely fitted peaks, only peaks fitted with Cramer-Rao lower bounds ≤ 8% were considered.

To reconstruct the FF maps, the voxel-wise FF was calculated as follows:

$$\mathrm{FF} = \frac{\mathrm{signal}_{\text{specific lipid compnent}}}{\mathrm{signal}_{Total}} * 100 \quad (1)$$

For ^{23}Na data, no MC was implemented since no contaminating peak is needed to be removed here. However, since the ^{23}Na signal decays much faster than the protons of lipid, its signal is T_2^*-weighted. Therefore, the ^{23}Na signals were corrected using the T_2^* values measured in Chapter 3. These corrected signals were then calibrated to their corresponding absolute ^{23}Na concentration values by using external concentration references (phantoms of known ^{23}Na

concentrations, 10, 20, 30, and 40 mM) included within the scanned FOV. The phantom signals and their known concentration were regressed to get a linear equation to calibrate the tissue sodium signal and calculate their absolute concentration maps in mM. Example of generated maps can be seen in Figure 4.1 below.

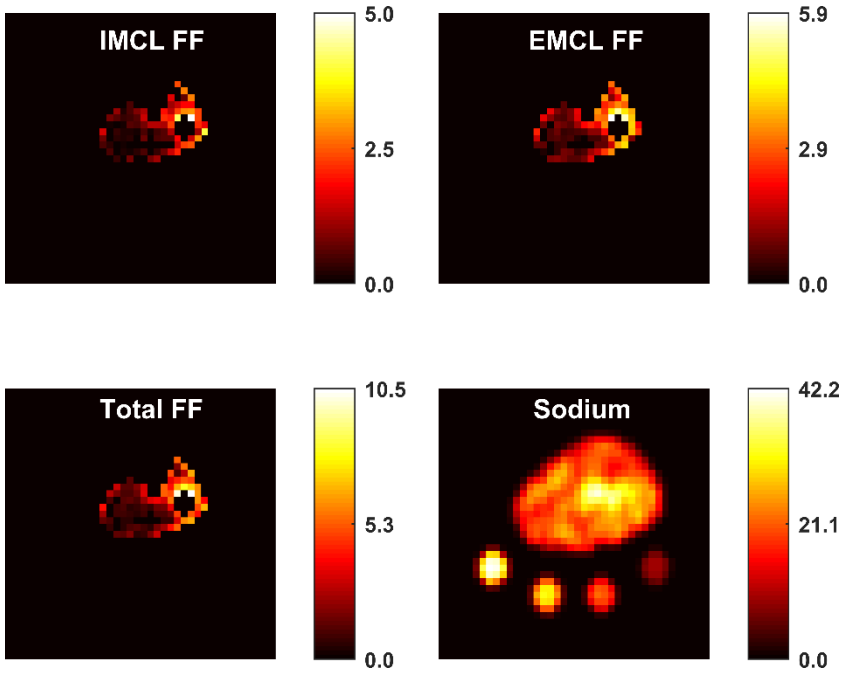

Figure 4.1 Examples of IMCL FF, EMCL FF, total lipids FF, and sodium concentration maps. The subcutaneous lipids were masked out in order to visualize the muscular region lipids which have a much lower FF. The circular shapes in the sodium map represent the quantification references of 10, 20, 30, and 40 mM concentration

4.2.4 Regions of Interest Segmentation

To assess the regional sodium and lipid levels within the scanned area, calf muscle regions were manually segmented by drawing ROIs over them based on their high-resolution T_1-weighted image. The ROI borders were determined by following the muscle boundaries. These ROIs were down-sampled to match MRSI resolution and co-registered to each lipid FF map to assess their distribution voxel-wisely. To reduce any partial volume effect by adjacent structures, voxels on the borders were excluded from the down-sampled ROIs (Figure 4.2). Additionally, to avoid overestimating sodium contents, the central muscles were also excluded since they are within a very vascular region (^{23}Na concentration is more than four times higher in blood[42]).

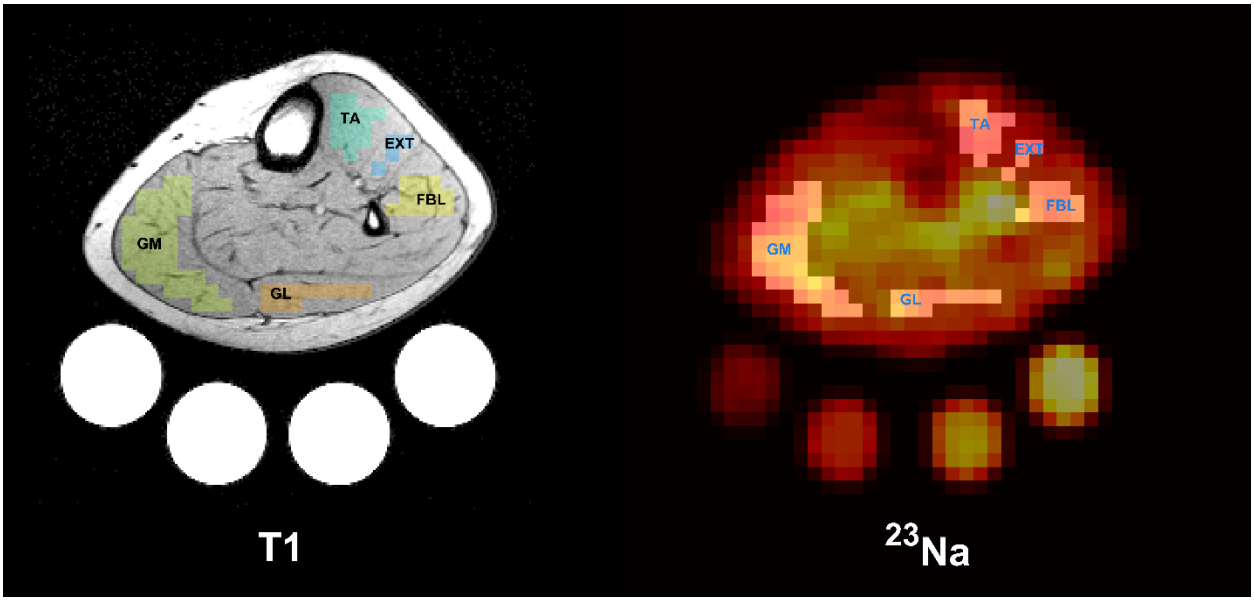

Figure 4.2 A representative example of the segmented regions of interest (ROIs). The peripheral muscles [GM, Gastrocnemius medialis muscle; GL, Gastrocnemius lateralis muscle; FBL, Fibularis muscles; EXT, Extensor longus muscles; and TA, Tibialis anterior muscle] were drawn on a high-resolution T1 axial image and down-sampled to the MRSI spatial resolution (left). To avoid overestimating the actual muscle sodium (^{23}Na) concentration, the central muscles were excluded since they are within a rich vascular region of high ^{23}Na concentration compared to muscles as shown in the ^{23}Na map (right)

4.2.5 Data Analysis

To assess the sex difference in lipid (or sodium) levels, a two-sample t-test was used. The BMI and age effects on each of the sodium and lipid component levels were studied by multiple linear regressions. Additionally, a Kruskal-Wallis (KW) one-way analysis of variance test was used to study the MSC, IMCL, EMCL, and total FF regional differences. The KW test was followed by Bonferroni multiple comparison correction to determine whether a significant difference exists between any two muscles. Finally, correlations between sodium and IMCL, EMCL, and total lipids within each muscle were performed with multivariate regressions to account for any multicollinearity.

4.3 Results

As can be seen from Figure 4.3, The t-test analysis showed no significant sex difference in the ^{23}Na concentration ($P = 0.7$), total FF ($P = 0.1$), IMCL FF ($P = 0.06$), or EMCL FF ($P = 0.1$) within the calf muscles.

Based on the multiple linear regressions results (Figure 4.4), there was a very significant and negative correlation between BMI and ^{23}Na concentration in the calf muscles with a correlation coefficient (r) = -0.7 and P <0.01. For lipids, the correlation with BMI was positive, but not significant (P > 0.05). Additionally, age had no significant association with either ^{23}Na or lipid levels.

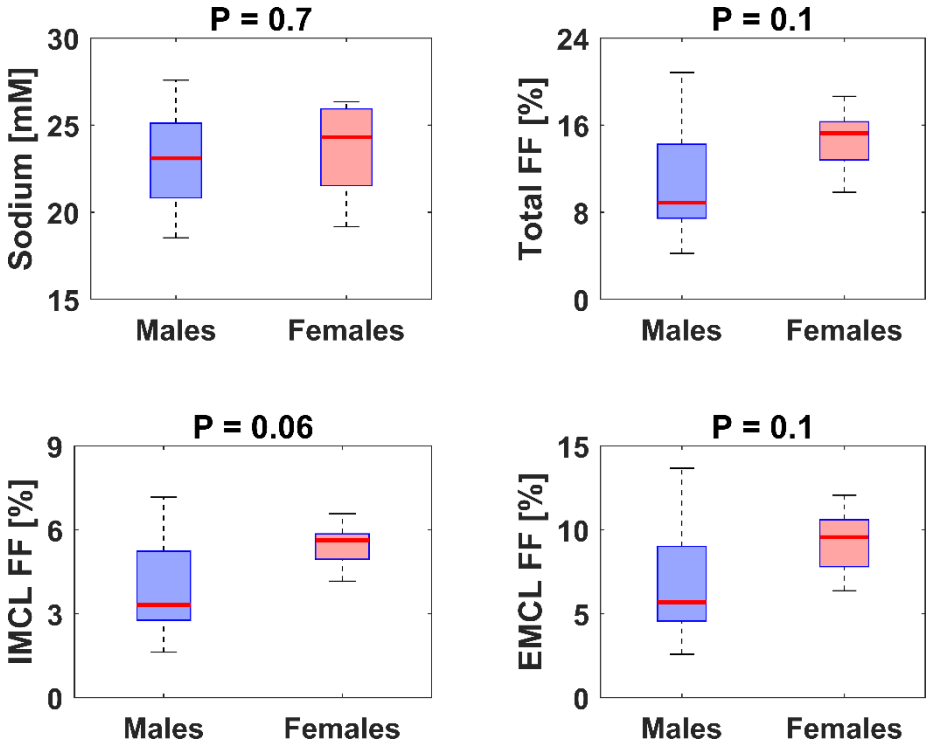

Figure 4.3 Two-sample t-test results of studying the sex difference in sodium concentration, total FF, intramyocellular lipid (IMCL) FF, and extramyocellular lipid (EMCL) FF. In general, no significant sex differences were found within the calf muscles. However, females tend to have larger medians

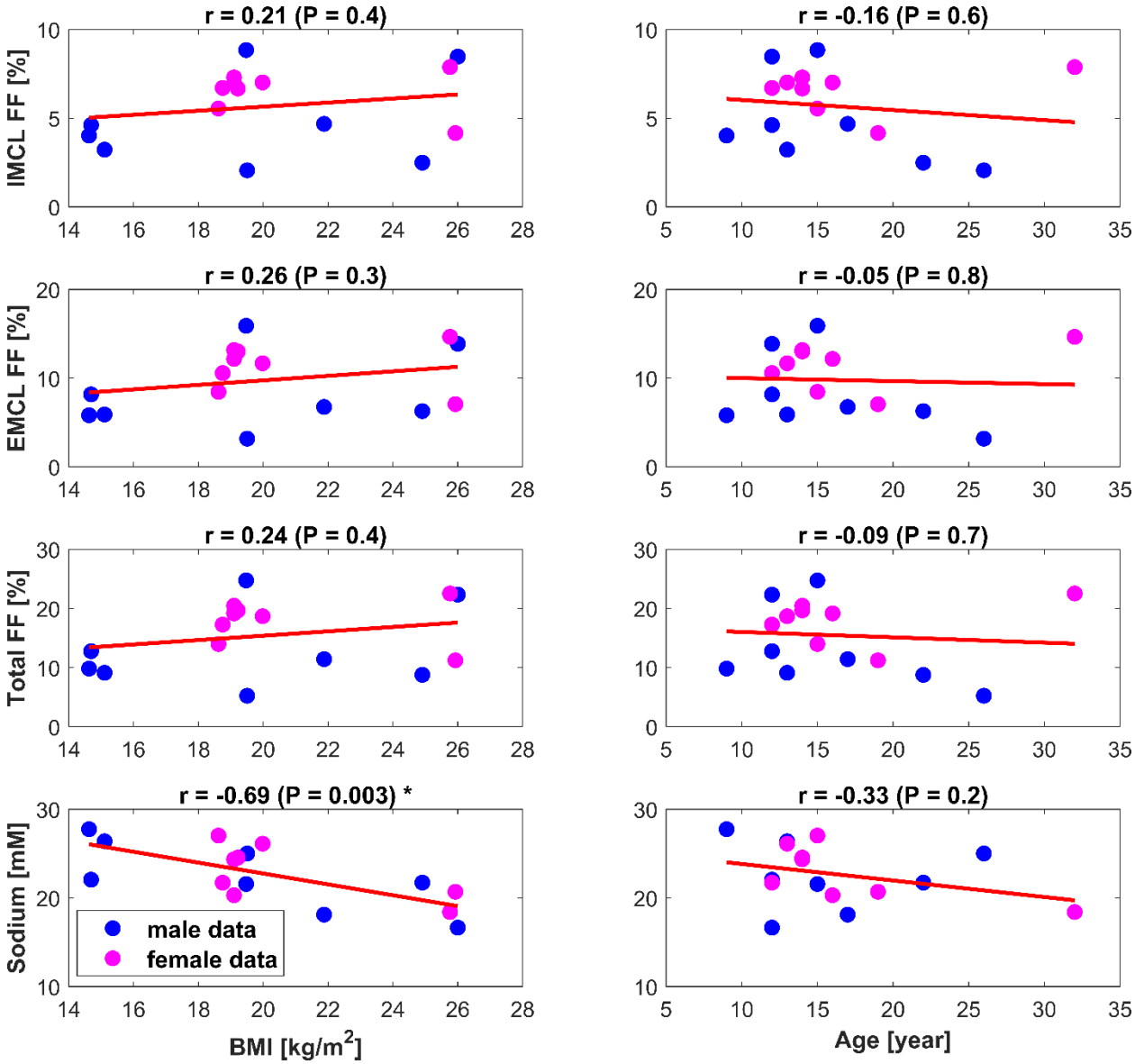

Figure 4.4 Linear regression analyses showing the correlations of BMI (left column) and age (right column) with IMCL, EMCL, total FF, and sodium concentration within the calf muscles from all subjects. Data points are mean ROI values per subject (blue for males, pink for females). Correlation coefficients (r) and P-values (P) are listed above each analysis

A strong ($P < 0.05$) regional variation in sodium and lipid components levels was found among the calf muscles (Figure 4.5, left column). According to the Bonferroni tests, the gastrocnemius muscles have preferentially higher MSC, EMCL, and total FF. The general trend of this variation was similar in males and females (Figure 4.5, middle column), and MSC and all lipid components (see Figure 4.5, right column).

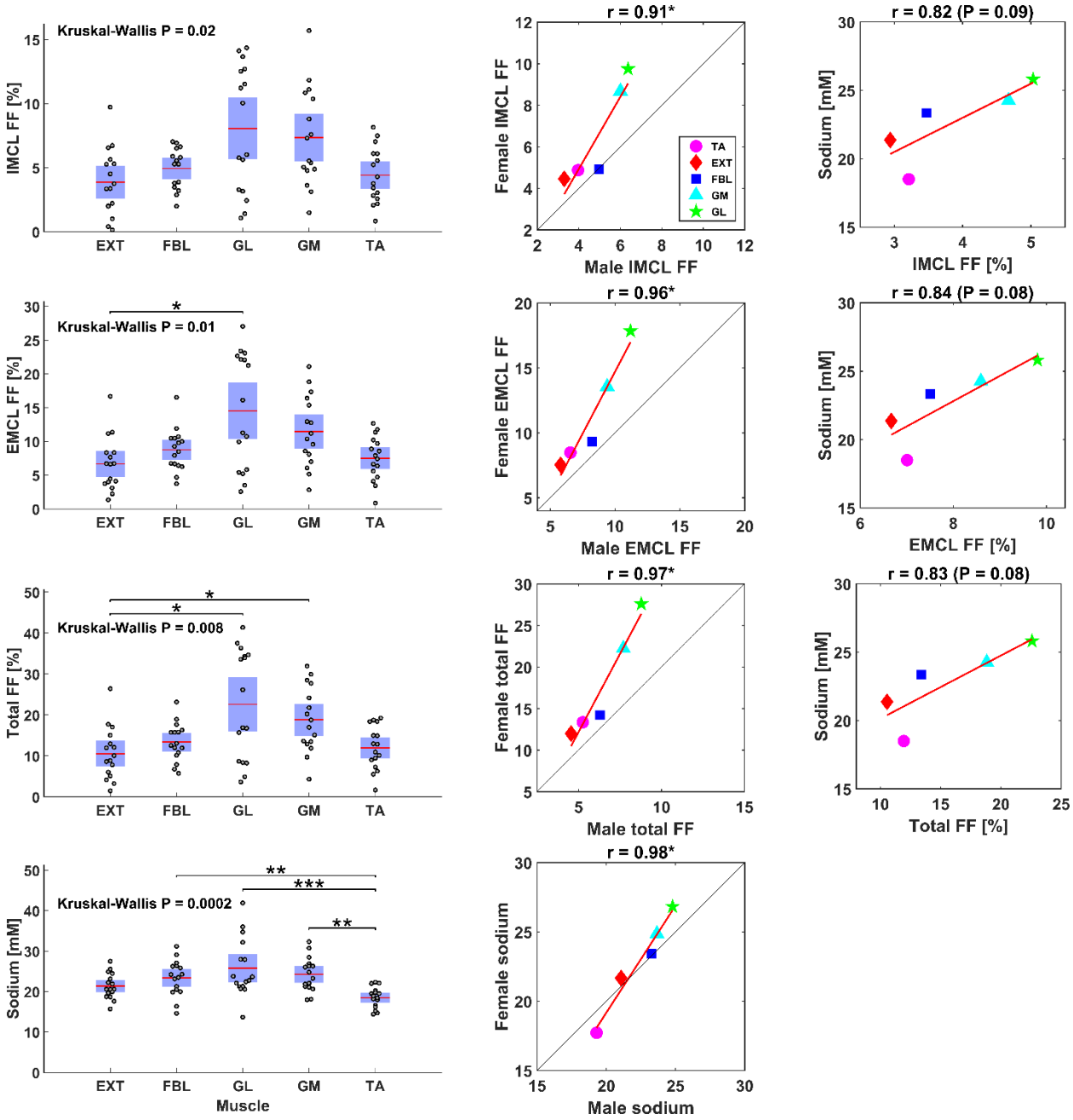

Figure 4.5 Muscle regional comparison (left column). Comparison between the regional variation trend in males versus in females (middle column), and sodium versus the lipid component contents (right column). * denotes P-value < 0.05

The multivariate regression analyses constantly showed a negative correlation between lipid component FFs and the MSC within each calf muscle. However, none of these correlations were significant (see Table 4.1)

Table 4.1 Correlations between the MSC and lipid component FFs within each muscle

Muscle	IMCL FF		EMCL FF		Total FF	
	r	***P*[#]**	***r***	***P*[#]**	***r***	***P*[#]**
EXT	-0.16	0.9	-0.13	0.8	-0.15	0.9
FBL	-0.52	0.3	-0.21	0.5	-0.36	0.9
GL	-0.15	0.7	-0.13	0.7	-0.14	0.7
GM	-0.05	0.5	-0.31	0.2	-0.23	0.3
TA	-0.16	0.9	-0.06	0.7	-0.10	0.8
Avg. muscles	-0.37	0.2	-0.38	0.3	-0.38	0.3

[#] P-values after accounting for the BMI confounding effect

4.4 Discussion

In this chapter, we showed that the used MRSI techniques could provide the required quantitative sodium and lipid component maps that have been used to study their relations. Additionally, ^{23}Na, IMCL, and EMCL levels within the calf muscles were evaluated to assess a potential sex difference. These ^{23}Na and lipid components were also studied as a function of BMI and age. Their spatial distribution among muscles was examined as well. Finally, the lipid components FFs were correlated to the absolute MSC within each involved calf muscle.

Although no significant sex difference has been found, a common trend of having more muscular lipids in females compared to males was noticed from the boxplot medians (Figure 4.3). Among the tested lipids, the IMCL component has the strongest sex difference (P =0.06). The other lipids follow the same trend, but with less statistical significance as a result of their wide variance. This trend can also be seen in the regional comparison (Figure 4.5, middle column). A similar general trend has been observed in a previous lipid study,[142] where higher (but insignificant) IMCL and total FFs in females were noticed within the muscles tested in our work.

The multiple linear regression to assess the effect of BMI and age on lipids and sodium showed an insignificant impact of age. However, there was a strong negative correlation between BMI and the calf MSC (r = -0.7, P <0.01). The lipid components have a positive correlation with the BMI (r = 0.24 ± 0.4), which was statistically insignificant. In a previous study, BMI was positively correlated with the sodium-potassium ratio measured in excreted urine.[141] This may

support our finding of a negative correlation between the BMI and the calf muscle sodium level. Besides, a more related finding was previously noticed in another study done in muscles. The sodium-potassium-ATPase was found to be elevated with BMI but not with age in skeletal muscle biopsy samples.[143] This was linked to an elevation in resting metabolic rate and energy consumption. The sodium-potassium-ATPase regulates pumping the sodium outside the cell.[144] Thus, it is in accord with our negative correlation between the BMI and ^{23}Na concentration found here. However, even with all these pieces of information, the underlying mechanism governing this relation is still unclear. Therefore, further in-depth studies are needed.

In a previous ^{23}Na-MRI study, an age-dependent MSC has been noticed after the 40 year age (above our population age range) and was only found in men.[49] The FF has also been found to be higher in the older population (above 40 years) compared to a younger population.[103] In another ^{23}Na-MRI study acquired with less T_2 bias and younger subjects, no influence of age on the calf MSC or total FF has been found within the control subjects,[145] which is in-line with our results. However, they found that the total FF increased with age in the Duchenne muscular dystrophy patients. Hence, any correlation is likely affected by pathologic conditions as well.

In addition to the assessment of BMI and age impacts on MSC and lipid levels between subjects, we performed a spatially resolved study to provide insight about the sodium-lipid distribution within subjects. The FFs and MSC were found to vary significantly among the calf muscles (Figure 4.5, left column). This spatial distribution finding was consistent in males and females (Figure 4.5, middle column), and for FF and MSC (Figure 4.5, right column). Overall, the calf MSC and lipid component FFs were always higher within gastrocnemius lateralis (GL) and gastrocnemius medialis (GM) muscles compared to their levels within the tibialis anterior (TA), extensor longus (EXT), and fibularis (FBL) muscles. This is suggesting a positive relationship between the MSC and lipids within these calf muscles. In previous works, the trend of having more IMCL and EMCL,[101] and total FF[103] in the GL and GM relative to TA had also been observed.[103] Although there was a consistent negative correlation between the MSC and the lipid components in each muscle (Table 4.1), the multivariant analysis showed that these correlations are not statistically significant and may result from the BMI-sodium negative linearity between subjects.

The regional variation of muscle lipids was related to the amount of slow-twitch (type I) fibers in the muscles.[41,101] For example, GM and GL fibers are a mixture of types I and II fibers, whereas TA and EXT fibers are mainly of type II.[146] Unlike type I fibers, type II fibers are larger

in diameter, contain fewer mitochondria, depend more on the ATPase activity to produce energy and thus store less IMCL for the mitochondrial oxidation process.[106–108] Additionally, the fiber orientation,[74] and function[101] of muscles were suggested as further potential contributors in the regional differences of lipid. These factors can equally take a role in the ^{23}Na regional variation. Thus, the variation of MSC and FFs among muscles is another research topic that needs to be investigated further.

The positive relationship between the calf muscle ^{23}Na concentration and lipid FFs inferred from the regional comparison may seem to be contradicting the previous finding of a negative correlation of sodium content with BMI. Also, the negative MSC-BMI correlation may appear to conflict with dietary studies that associate the ^{23}Na intake with obesity, BMI, and waist circumference.[147] However, the BMI is a measurement that represents the entire body fat composition, while the IMCL and EMCL FFs are measurements reflecting only the fat content within the scanned muscles. Even among muscles, the fat contents are not constant, and the results of our study represent healthy calf muscles only. For example, in a previous work studying the associations of total FF with weight in the thigh and calf regions, significant results were only found in the thigh data, which made them suggesting a preferential lipid accumulation in the thigh.[148] Further, in a study that covered the upper and lower limbs of lipedema patients, the elevation of both lipid and ^{23}Na was only found in the lower legs.[139] In addition, the lipid level in muscles can change with time in health disorders, as muscle is not an adipose tissue that makes the lipid buildup within the muscles a long-term process.[149] Thus, the association may vary based on tissue, region, and health condition.

Some other physiological similarities shared by ^{23}Na and lipids are the energy, hormonal, and immune system influence. While lipids are considered a cellular energy source and provides useful information about the energy supply,[26] sodium controls the cellular energy through its ATPase.[144] Both lipids and sodium are also influenced by hormones. For instance, elevated plasma aldosterone levels are found to promote sodium retention and are independently associated with obesity.[150] Moreover, other studies related autoimmunity diseases to fatty acids[151] and to sodium influences.[152]

This study has a technical limitation. While 4 ms of scanning delay time is considered short for proton imaging, it is considered long for sodium (since the ^{23}Na spins are characterized with ultrashort transverse relaxation time (T_2) compared to ^{1}H), which may result in underestimating

the absolute MSC. However, we corrected this by using the T_2^* values provided for each muscle in Chapter 3. To make sure that this correction is adequate, we compared the MRSI data acquired with a 4 ms delay to data measured by a 3D-MRI sequence with only a 0.3 ms delay and higher spatial resolution (4×4 mm^2). As can be seen in Figure 4.6, after applying a T_2^* correction to the MRSI signal to a 0.3 ms delay, it matches the concentration obtained by the 3D-MRI. In terms of study design limitations, we included only Caucasian subjects to reduce the number of covariables, as race differences in sodium levels has been reported earlier.[153] Thus, the results of our study may not apply to all races.

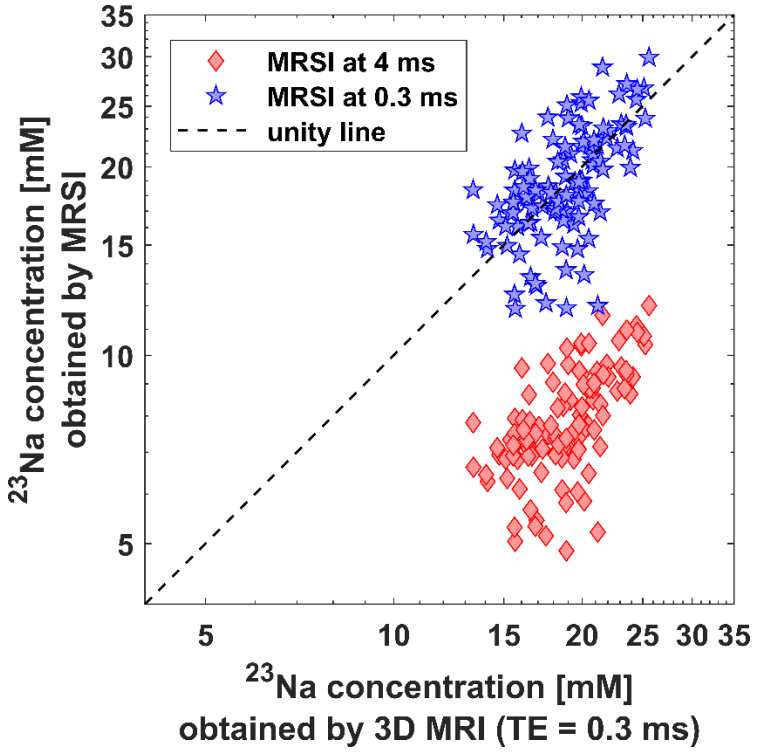

Figure 4.6 Impact of sodium transverse relaxation time (T_2^*) correction on sodium concentration. The fast decaying ^{23}Na-MRSI signals were acquired at 4 ms (red diamond), which is not short enough to avoid the T_2^* bias and thus underestimate the true concentration. These signals were corrected by using the regional T_2^* values at 3T found in Chapter 3. The blue stars represent the concentration after T_2^* correction to a 0.3 ms delay. The corrected data nicely correlates with data measured at the same echo time (TE) of 0.3 ms. This demonstrates the importance of T_2^* correction to obtain correct estimates of sodium concentration

In addition to presenting new baseline results from healthy subjects, our results confirmed previously reported findings from studies conducted with less convenient tools. As discussed above, the results in this work are in-line with previous findings done by a variety of methods

(invasive and non-invasive). Thus, our proposed MRSI methods can be used as a fast and accurate method to quantify ^{23}Na and lipid components noninvasively and to obtain information on their regional distribution. We showed the feasibility of using MRSI to perform a quantitative comparison between sodium and lipid tissue concentrations in healthy subjects. In the future, it will be of interest to perform similar studies under pathological conditions associated with alterations in ^{23}Na and/or lipid levels to evaluate their interaction under different conditions. Additionally, here, we only included the total IMCL and total EMCL components. For many diseases, only a particular lipid of a specific chemical group is related to the health condition. For instance, the bulk methylene IMCL has been found to be the lipid that elevates in cases of insulin sensitivity,[24] mitochondrial disorders,[27] and with exercises.[28] On the other hand, an increase of the saturated lipids with a decline of unsaturated olefinic lipids in bone marrow were associated with osteoporosis.[29] These specific chemical groups of lipids can also be mapped separately with the proposed ^{1}H-MRSI technique. Finally, these methods can also be used beyond muscles. Extra studies to reveal the detailed relation between sodium and lipids are still needed.

4.5 Conclusions

Novel fast MRSI methods allow for noninvasive quantification and regional comparison between ^{23}Na concentration and the FF of different lipid components within a clinically feasible time. In healthy subjects, there is a strong negative relationship between BMI and ^{23}Na concentration within the calf muscles. In terms of spatial distribution, both ^{23}Na and lipid components levels follow the same trend among different evaluated calf muscle regions, suggesting a positive spatial relation between them. Further investigations of the relation in different human tissues and regions under health and diseases are required.

CHAPTER 5 : CONCLUSIONS AND FUTURE WORK

In chapter 2 and 3, we introduced advanced lipid-MRSI and ^{23}Na-MRSI techniques that overcome several drawbacks of the available quantification methods. In chapter 4, the MRSI techniques were utilized to facilitate the study of potential correlations between the sodium concentration and lipid components (IMCL and EMCL) FF within the calf muscles region.

The advantages, limitations, and potential future usage (or development) of this work will be summarized in this chapter.

5.1 Lipid MRSI

5.1.1 Advantages

Compared to other MRSI techniques, the implemented technique allows results of higher resolution (0.25 mL) within a shorter scan time (~3 min). Typically, conventional lipid-MRSI techniques require long scan times ranging from about 17 - 50 minutes based on the spatial resolution (usually, 0.25 - 0.76 mL). The high spatial resolution is essential to reduce the effect of fiber orientation heterogeneity to get resolved lipid peaks.

Compared to other accelerated MRSI, our DW CRT MRSI grants higher SNR that facilitates detecting the lipid components of relatively low signal intensity, which is commonly challenging. Moreover, CRT acquisition has been found to be less sensitive to system imperfection compared to other methods such as EPSI and spiral acquisition methods. Additionally, by implementing the MC technique, simultaneous separate water-only and metabolites-only (with only ~ 1% residual water) spectra can be generated within a single fast acquisition. This is a significant advantage, as it reduces scan duration by eliminating the lengthy time needed to suppress water information with conventional methods. Alternative approaches will be: 1) acquiring two data sets (water suppressed, and non-water suppressed) resulting in long acquisition times, or 2) using only a non-water suppressed data that allows resolving only the most intense methylene peak.

Further, the water-only and metabolite-only spectra generated after implementing the MC can be used to get differentiated fatty acids FF maps that cannot be produced by other available

imaging methods. This is important because each fatty acid carries different unique information. In many clinical applications, only specific fatty acid/s is/are associated. For instance, diabetes was associated with an increase in the methylene IMCL FF. At the same time, osteoporosis was linked to an increase in the saturated lipid FF together with a decrease in the unsaturated olefinic FF. Since MR-imaging techniques cannot differentiate these lipids, single-voxel MRS techniques are usually used to obtain these lipids information. However, the single-voxel MRS information reflects a limited region of interest, which is most likely not representative of the surrounding regions. This is a major limitation when assessing heterogeneous diseases (such as liver steatosis) or naturally complex organs. Even within the calf muscles, we have shown significant regional variations in lipid FF. In these cases, MRSI is preferred to map the lipids and show their regional distributions. With the proposed DW-CRT MC MRSI, we showed that reconstructing differentiated lipid component FF maps is feasible with good quality (high quantification accuracy, high signal sensitivity, and good spatial resolution) within a quick scan.

Thus, the advantages of this method are the ability to provide in vivo quantitative information about different fatty acids with their spatial distribution, and within a clinically accepted scan time. Hence, this novel MRSI tool provides unique outputs for improved diagnosis and characterization of health disorders, and it facilitates the investigation of new potential applications that were hard to perform with the limitations of the other quantification methods.

5.1.2 Limitations

Similar to all MRS based techniques, this MRSI needs special expertise to deal with the resulting data. To get useful information from the collected spectra, they need complex post-processing before fitting their peaks. Additionally, the fitting of multiple voxels may require several minutes. However, this can be mitigated with faster computer processors. Although DW-CRT (with alpha=1) resulted in a better SNR compared to conventional Cartesian k-space-filling trajectory methods such as EPSI, it suffers from a degraded spatial response function. In our case, gaining more SNR with a cost of degradation in spatial response function was worthy since high SNR is needed to detect the small lipid peaks. Compared to MRI (typically at 1 x 1 cm^2 in-plane resolution), MRSI usually has a lower spatial resolution. This may introduce some partial volume effect, increase signal leakage between voxels due to the larger point spread function, which may result in blurry images. Yet, the implemented MRSI resolution in this work is considered high compared

to currently available MRSI methods, as described in the preceding section. Additionally, within our ^{23}Na-MRSI study (Chapter 3), we showed the ability to reach a higher in-plane resolution (2.5 x 2.5 mm^2) with our proposed MRSI technique without hardware limitations. Since ^{1}H has a higher SNR and needs lower hardware requirements relative to ^{23}Na, the ^{23}Na-MRSI method can be translated for ^{1}H acquisitions with higher spatial resolutions (similar to the MRI resolutions).

5.1.3 Future Directions

Many applications can make use of the proposed MRSI. Basically, any triglyceride quantification application or any Dixon MRI usage that does not require a resolution higher than 0.25 mL can profit from this technique. Some representative examples within the skeletal muscles include diabetes, hypertension, lipedema, and Duchenne muscular dystrophy. Beyond muscles, diseases linked to the fat accumulation in kidney, pancreas, liver, and breast may be evaluated by this MRSI technique. For instance, our fast high-resolution MRSI can be used to evaluate renal cell carcinoma by quantifying the lipids within the thin kidney cortex with less contamination from its surrounding structures (higher resolution introduces less partial volume effect).

In addition to lipids, MRSI can provides extra metabolites such as choline (malignancy marker), and creatine and carnitine (energy change biomarkers). Combining the information from these biomarkers and the lipids can help better characterization of health disorders. For example, breast choline information can be used to enhance the diagnosis specificity (breast MRI screenings are known to be of high sensitivity and relatively low specificity).

Theoretically, the spatial resolution can be increased to meet the needs of any application that require higher spatial details. However, more scan averages may be needed to compensate for the lost SNR that would prolong the acquisition period. Thus, developing more sophisticated acceleration approaches may assist in this case. Moreover, reducing the acquisition delay time would be useful to reduce the amount of phase and j-coupling effects. However, reaching shorter delay times may be challenging due to the magnetic gradient requirements. Accordingly, innovative techniques to shorten the readout delay are anticipated to be of great interest. With our advanced OVS-based ^{23}Na-MRSI technique (Chapter 3), we showed the feasibility of reaching a higher resolution and scanning with a shorter delay (< 0.6 ms). However, tailoring this OVS-based technique for ^{1}H acquisition is still needed.

5.2 Sodium MRSI

5.2.1 Advantages

With the developed ^{23}Na-MRSI, the in vivo absolute ^{23}Na concentration can be measured with a minimum relaxation bias. Further, valuable regional relaxation information is simultaneously provided. Previously, such information would require a much longer time to be acquired and with less spatial resolution. Compared to 3D MRI techniques, which acquire a few time-points (8-38) with nominal spatial resolution ranging between 2.8 x 2.8 and 6 x 6 mm^2 within lengthy scan times (40 – 60 minutes), our MRSI method can collect 64 time-points with 2.5 x 2.5 mm^2 nominal spatial resolution within only ~15 minutes. Thus, our MRSI method allows better T_2^* estimation within acceptable acquisition time and with better spatial quality.

As implemented in Chapter 4, the measured transverse relaxation constants from Chapter 3 can be used to mitigate the relaxation bias on datasets collected at any TE. Thus, it can help other studies in this aspect. That being said, performing subject-specific relaxometry measurements using methods similar to the proposed one would still provide more precise results, grant voxel-wise correction, and provide additional physiological information.

Examples of potential clinical applications include, but are not limited to, diabetes, cardiovascular and renal diseases, tumor diagnosis and responses, strokes, multiple sclerosis, lipedema, and osteoarthritis. The enhancement in the concentration estimation accuracy and spatial resolution allowed with the provided MRSI is expected to improve characterizing health diseases associated with ^{23}Na concentration elevation even within relatively small anatomy. Further, the ability to map T_2^* with their signal contribution fraction within acceptable scan duration would provide a valuable clinical tool to assess in vivo physiological and molecular environment status.

5.2.2 Limitations

The OVS bands combined with the ^{23}Na-MRSI is highly dependent on the T_1 of the tissues to be suppressed. As shown in Chapter 3, the OVS performed very well in the leg area. However, similar performance at other locations cannot be confirmed without further investigations.

5.2.3 Future Directions

Since absolute ^{23}Na concentration can be provided more accurately, health disorders related to the increase of sodium concentration can be conducted. The extra relaxation values can also provide additional diagnostic insight, as it carries information on physiological alterations.

Since the ^{23}Na-MRSI has been tested only on the lower leg region, additional evaluation at different body regions may be of interest. Additionally, testing the sequence with different diseases is also required, as it tried only on healthy subjects.

In terms of technical improvements, the TR can be reduced, which will render a shorter acquisition duration. Anyway, the TR should be long enough to avoid any T_1 weighting effect. In addition, reducing the delay time and increasing the FID sampling rate may boost the fitting quality further. Moreover, a faster and more robust fitting method would help this and many other relaxation mapping studies to enhance their results.

5.3 Sodium-lipid correlation

5.3.1 Findings

While various health disorders and physiological changes have been previously related to the accumulation of lipids and sodium, the correlation between these metabolites is still unclear. This is the first time a study correlates the levels of ^{23}Na and the specific lipid components (IMCL and EMCL). By conducting this study, we showed the feasibility of performing such a correlation. Also, with this study, we contributed in setting baseline information based on the results observed within the healthy calf muscles. Our findings suggest a positive spatial relationship between ^{23}Na and lipid levels within the investigated human calf muscles. However, the underlying physiological reason still needs further investigation. Furthermore, we observed a negative sodium-BMI correlation within the calf muscles. Thus, the BMI variable should be accounted for when performing a ^{23}Na study within the calf muscles.

5.3.2 Limitations

The correlation study had a few design limitations. The sample size was relatively small because of our limited budget. However, subjects were recruited carefully to cover certain age (young) and BMI (healthy) ranges. Moreover, only white subjects were included to avoid extra variables from

race differences that have been noticed from earlier sodium diet experiments. While this may be considered as a limitation, it keeps the door open for future studies to assess the correlation under the race difference influence.

5.3.3 Future Directions

As an initial step, we studied the correlation of ^{23}Na-lipids levels within the calf region of healthy subjects and under normal conditions. Now, with the introduced MRSI techniques, it is possible to evaluate the correlation at different body locations, within patients with diseases characterized by fat infiltration and sodium level elevation. Additionally, exercise studies that were limited to single voxel-MRS can now be conducted with extra spatial distribution information.

5.4 Summary

In this work, two sophisticated and practical MRSI techniques were developed to facilitate evaluating lipids and sodium levels noninvasively. The feasibility of these techniques has been shown within healthy calf muscles region. Compared to the available techniques, the proposed methods were able to deliver faster and superior quantification results.

Unfortunately, many appealing MR applications require long scan times that eventually result in a high cost and discomfort for patients that hinder the spreading of their clinical usage. Here, we considered this point by developing improved quality MR methods that can be used within a reasonable acquisition time. In addition to reducing the scan duration, the proposed MRSI method overcome several limitations of the available lipid and sodium quantification methods; our MRSI methods are non-invasive (vs. biopsy), have better spatial resolution (vs. MRS and lower resolution MRSI), and provide differentiated lipid components and metabolite maps with higher sensitivity and quantification accuracy (vs. imaging methods).We hope that these improvements would increase the chance of using such MR techniques more frequently. Taking into account the other added values in sensitivity and extra information that can be provided by the proposed method, it is anticipated that further development and optimization of similar techniques will be of research interest. Additionally, the sodium-lipid relationship suggested here may also open the door for more in-depth studies of their interaction in health and disease.

REFERENCES

1. Cunningham CH, Vigneron DB, Chen AP, et al. Design of flyback echo-planar readout gradients for magnetic resonance spectroscopic imaging. *Magn Reson Med*. 2005. doi:10.1002/mrm.20663
2. Posse S, Otazo R, Caprihan A, et al. Proton echo-planar spectroscopic imaging of J-coupled resonances in human brain at 3 and 4 Tesla. *Magn Reson Med*. 2007. doi:10.1002/mrm.21287
3. Furuyama JK, Wilson NE, Thomas MA. Spectroscopic imaging using concentrically circular echo-planar trajectories in vivo. *Magn Reson Med*. 2012. doi:10.1002/mrm.23184
4. Adalsteinsson E, Irarrazabal P, Topp S, Meyer C, Macovski A, Spielman DM. Volumetric spectroscopic imaging with spiral-based k-space trajectories. *Magn Reson Med*. 1998. doi:10.1002/mrm.1910390606
5. Dydak U, Weiger M, Pruessmann KP, Meier D, Boesiger P. Sensitivity-encoded spectroscopic imaging. *Magn Reson Med*. 2001. doi:10.1002/mrm.1250
6. Tsai SY, Otazo R, Posse S, et al. Accelerated proton echo planar spectroscopic imaging (PEPSI) using GRAPPA with a 32-channel phased-array coil. *Magn Reson Med*. 2008. doi:10.1002/mrm.21545
7. Otazo R, Sodickson D, Yoshimoto A, Posse S. Accelerated Proton Echo-Planar Spectroscopic Imaging Using Parallel Imaging and Compressed Sensing. In: *Proceedings 17th Scientific Meeting, International Society for Magnetic Resonance in Medicine*. ; 2009.
8. Chiew M, Jiang W, Burns B, et al. Density-weighted concentric rings k-space trajectory for1H magnetic resonance spectroscopic imaging at 7 T. *NMR Biomed*. 2018. doi:10.1002/nbm.3838
9. Jiang W, Lustig M, Larson PEZ. Concentric rings K-space trajectory for hyperpolarized 13C MR spectroscopic imaging. *Magn Reson Med*. 2016. doi:10.1002/mrm.25577
10. La Scala J, Wool RP. Property analysis of triglyceride-based thermosets. *Polymer (Guildf)*. 2005. doi:10.1016/j.polymer.2004.11.002

11. Eggstein M, Kuhlmann E. Triglycerides and Glycerol Determination after Alkaline Hydrolysis. In: *Methods of Enzymatic Analysis*. ; 1974. doi:10.1016/b978-0-12-091304-6.50035-5
12. Abbasi F, Brown BW, Lamendola C, McLaughlin T, Reaven GM. Relationship between obesity, insulin resistance, and coronary heart disease risk. *J Am Coll Cardiol*. 2002. doi:10.1016/S0735-1097(02)02051-X
13. Sjögren P, Sierra-Johnson J, Gertow K, et al. Fatty acid desaturases in human adipose tissue: Relationships between gene expression, desaturation indexes and insulin resistance. *Diabetologia*. 2008. doi:10.1007/s00125-007-0876-9
14. Miles EA, Calder PC. Fatty acids, lipid emulsions and the immune and inflammatory systems. *World Rev Nutr Diet*. 2015. doi:10.1159/000365426
15. Süllentrop F, Hahn J, Moka D. In Vitro and in vivo 1H-MR spectroscopic examination of the renal cell carcinoma. *Int J Biomed Sci*. 2012;8(2):94-108.
16. Boesch C, Slotboom J, Hoppeler H, Kreis R. In vivo determination of intra-myocellular lipids in human muscle by means of localized1H-MR-spectroscopy. *Magn Reson Med*. 1997. doi:10.1002/mrm.1910370403
17. Wren TAL, Bluml S, Tseng-Ong L, Gilsanz V. Three-point technique of fat quantification of muscle tissue as a marker of disease progression in Duchenne muscular dystrophy: preliminary study. *AJR Am J Roentgenol*. 2008. doi:10.2214/AJR.07.2732
18. Goodpaster BH, Wolf D. Skeletal muscle lipid accumulation in obesity, insulin resistance, and type 2 diabetes. *Pediatr Diabetes*. 2004. doi:10.1111/j.1399-543X.2004.00071.x
19. Lee S, Lucas RM, Lansdown DA, et al. Magnetic resonance rotator cuff fat fraction and its relationship with tendon tear severity and subject characteristics. *J Shoulder Elb Surg*. 2015. doi:10.1016/j.jse.2015.01.013
20. Gaeta M, Mileto A, Mazzeo A, et al. MRI findings, patterns of disease distribution, and muscle fat fraction calculation in five patients with Charcot-Marie-Tooth type 2 F disease. *Skeletal Radiol*. 2012. doi:10.1007/s00256-011-1199-y
21. Kühn JP, Hernando D, Meffert PJ, et al. Proton-density fat fraction and simultaneous R2*estimation as an MRI tool for assessment of osteoporosis. *Eur Radiol*. 2013. doi:10.1007/s00330-013-2950-7

22. Kumar D, Karampinos DC, MacLeod TD, et al. Quadriceps intramuscular fat fraction rather than muscle size is associated with knee osteoarthritis. *Osteoarthr Cartil*. 2014. doi:10.1016/j.joca.2013.12.005
23. Perseghin G, Scifo P, De Cobelli F, et al. Intramyocellular triglyceride content is a determinant of in vivo insulin resistance in humans: A 1H-13C nuclear magnetic resonance spectroscopy assessment in offspring of type 2 diabetic parents. *Diabetes*. 1999. doi:10.2337/diabetes.48.8.1600
24. Krssak M, Falk Petersen K, Dresner A, et al. Intramyocellular lipid concentrations are correlated with insulin sensitivity in humans: A 1H NMR spectroscopy study. *Diabetologia*. 1999. doi:10.1007/s001250051123
25. Vock R, Hoppeler H, Claassen H, et al. Design of the oxygen and substrate pathways. VI. Structural basis of intracellular substrate supply to mitochondria in muscle cells. *J Exp Biol*. 1996.
26. HAVEL RJ, CARLSON LA, EKELUND LG, HOLMGREN A. TURNOVER RATE AND OXIDATION OF DIFFERENT FREE FATTY ACIDS IN MAN DURING EXERCISE. *J Appl Physiol*. 1964. doi:10.1152/jappl.1964.19.4.613
27. Golla S, Ren J, Malloy CR, Pascual JM. Intramyocellular lipid excess in the mitochondrial disorder MELAS. *Neurol Genet*. 2017. doi:10.1212/NXG.0000000000000160
28. Thamer C, Machann J, Bachmann O, et al. Intramyocellular lipids: Anthropometric determinants and relationships with maximal aerobic capacity and insulin sensitivity. *J Clin Endocrinol Metab*. 2003. doi:10.1210/jc.2002-021674
29. Yeung DKW, Griffith JF, Antonio GE, Lee FKH, Woo J, Leung PC. Osteoporosis is associated with increased marrow fat content and decreased marrow fat unsaturation: A proton MR spectroscopy study. *J Magn Reson Imaging*. 2005. doi:10.1002/jmri.20367
30. Hoppeler H, Lüthi P, Claassen H, Weibel ER, Howald H. The ultrastructure of the normal human skeletal muscle - A morphometric analysis on untrained men, women and well-trained orienteers. *Pflügers Arch Eur J Physiol*. 1973. doi:10.1007/BF00588462
31. Goodpaster BH, Kelley DE, Thaete FL, He J, Ross R. Skeletal muscle attenuation determined by computed tomography is associated with skeletal muscle lipid content. *J Appl Physiol*. 2000. doi:10.1152/jappl.2000.89.1.104

32. Essén B, Hagenfeldt L, Kaijser L. Utilization of blood-borne and intramuscular substrates during continuous and intermittent exercise in man. *J Physiol*. 1977. doi:10.1113/jphysiol.1977.sp011726
33. Kelley DE, Slasky BS, Janosky J. Skeletal muscle density: Effects of obesity and non-insulin-dependent diabetes mellitus. *Am J Clin Nutr*. 1991. doi:10.1093/ajcn/54.3.509
34. Pietrobelli A, Faith MS, Allison DB, Gallagher D, Chiumello G, Heymsfield SB. Body mass index as a measure of adiposity among children and adolescents: A validation study. *J Pediatr*. 1998. doi:10.1016/S0022-3476(98)70433-0
35. Pietrobelli A, Wang Z, Formica C, SB H, Heymsfield SB. Dual-energy X-ray absorptiometry: fat estimation errors due to variation in soft tissue hydration. *Am J Physiol*. 1998.
36. Dixon WT. Simple proton spectroscopic imaging. *Radiology*. 1984;153(1):189-194.
37. Malenfant P, Joanisse DR, Thériault R, Goodpaster BH, Kelley DE, Simoneau JA. Fat content in individual muscle fibers of lean and obese subjects. *Int J Obes*. 2001. doi:10.1038/sj.ijo.0801733
38. Spielman D, Webb P, Macovski A. Water referencing for spectroscopic imaging. *Magn Reson Med*. 1989. doi:10.1002/mrm.1910120105
39. Johnson G, Jung KJ, Wu EX, Hilal SK. Self-correction of proton spectroscopic images for gradient eddy current distortions and static field inhomogeneities. *Magn Reson Med*. 1993. doi:10.1002/mrm.1910300217
40. Schick F, Eismann B, Jung W -I, Bongers H, Bunse M, Lutz O. Comparison of localized proton NMR signals of skeletal muscle and fat tissue in vivo: Two lipid compartments in muscle tissue. *Magn Reson Med*. 1993. doi:10.1002/mrm.1910290203
41. Hwang J-H, Pan JW, Heydari S, Hetherington HP, Stein DT. Regional differences in intramyocellular lipids in humans observed by in vivo ^{1}H-MR spectroscopic imaging. *J Appl Physiol*. 2001. doi:10.1152/jappl.2001.90.4.1267
42. Madelin G, Lee JS, Regatte RR, Jerschow A. Sodium MRI: Methods and applications. *Prog Nucl Magn Reson Spectrosc*. 2014. doi:10.1016/j.pnmrs.2014.02.001
43. Boada FE, Qian Y, Nemoto E, et al. Sodium MRI and the Assessment of Irreversible Tissue Damage During Hyper-Acute Stroke. *Transl Stroke Res*. 2012. doi:10.1007/s12975-012-0168-7

44. Paling D, Solanky BS, Riemer F, et al. Sodium accumulation is associated with disability and a progressive course in multiple sclerosis. *Brain*. 2013. doi:10.1093/brain/awt149
45. Mellon EA, Pilkinton DT, Clark CM, et al. Sodium MR imaging detection of mild Alzheimer disease: Preliminary study. *Am J Neuroradiol*. 2009. doi:10.3174/ajnr.A1495
46. Reetz K, Romanzetti S, Dogan I, et al. Increased brain tissue sodium concentration in Huntington's Disease - A sodium imaging study at 4T. *Neuroimage*. 2012. doi:10.1016/j.neuroimage.2012.07.009
47. Kopp C, Linz P, Maier C, et al. Elevated tissue sodium deposition in patients with type 2 diabetes on hemodialysis detected by 23Na magnetic resonance imaging. *Kidney Int*. 2018. doi:10.1016/j.kint.2017.11.021
48. Nagel AM, Amarteifio E, Lehmann-Horn F, et al. 3 Tesla sodium inversion recovery magnetic resonance imaging allows for improved visualization of intracellular sodium content changes in muscular channelopathies. *Invest Radiol*. 2011. doi:10.1097/RLI.0b013e31822836f6
49. Kopp C, Linz P, Dahlmann A, et al. 23Na magnetic resonance imaging-determined tissue sodium in healthy subjects and hypertensive patients. *Hypertension*. 2013. doi:10.1161/HYPERTENSIONAHA.111.00566
50. Ouwerkerk R, Jacobs MA, MacUra KJ, et al. Elevated tissue sodium concentration in malignant breast lesions detected with non-invasive 23Na MRI. *Breast Cancer Res Treat*. 2007. doi:10.1007/s10549-006-9485-4
51. Schepkin VD, Chenevert TL, Kuszpit K, et al. Sodium and proton diffusion MRI as biomarkers for early therapeutic response in subcutaneous tumors. *Magn Reson Imaging*. 2006. doi:10.1016/j.mri.2005.12.004
52. Berendsen HJC, Edzes HT. THE OBSERVATION AND GENERAL INTERPRETATION OF SODIUM MAGNETIC RESONANCE IN BIOLOGICAL MATERIAL. *Ann N Y Acad Sci*. 1973. doi:10.1111/j.1749-6632.1973.tb30799.x
53. Ra JB, Hilal SK, Cho ZH. A method for in vivo MR imaging of the short T2 component of sodium-23. *Magn Reson Med*. 1986. doi:10.1002/mrm.1910030213
54. Rooney WD, Springer CS. A comprehensive approach to the analysis and interpretation of the resonances of spins 3/2 from living systems. *NMR Biomed*. 1991. doi:10.1002/nbm.1940040502

55. Bottomley PA. Sodium MRI in Man: Technique and Findings. In: *Encyclopedia of Magnetic Resonance*. ; 2012. doi:10.1002/9780470034590.emrstm1252
56. Hu R, Kleimaier D, Malzacher M, Hoesl MAU, Paschke NK, Schad LR. X-nuclei imaging: Current state, technical challenges, and future directions. *J Magn Reson Imaging*. 2020. doi:10.1002/jmri.26780
57. Hawley JA, Holloszy JO. Exercise: It's the real thing! *Nutr Rev*. 2009. doi:10.1111/j.1753-4887.2009.00185.x
58. Goodpaster BH, Thaete FL, Kelley DE. Thigh adipose tissue distribution is associated with insulin resistance in obesity and in type 2 diabetes mellitus. *Am J Clin Nutr*. 2000. doi:10.1093/ajcn/71.4.885
59. Weber MA, Nagel AM, Jurkat-Rott K, Lehmann-Horn F. Sodium (23Na) MRI detects elevated muscular sodium concentration in Duchenne muscular dystrophy. *Neurology*. 2011. doi:10.1212/WNL.0b013e31823b9c78
60. Weber MA, Nagel AM, Marschar AM, et al. 7-T 35Cl and 23Na mr imaging for detection of mutationdependent alterations in muscular edema and fat fraction with sodium and chloride concentrations in muscular periodic paralyses. *Radiology*. 2016. doi:10.1148/radiol.2016151617
61. Chang G, Wang L, Schweitzer ME, Regatte RR. 3D 23Na MRI of human skeletal muscle at 7 tesla: Initial experience. *Eur Radiol*. 2010. doi:10.1007/s00330-010-1761-3
62. Hammon M, Grossmann S, Linz P, et al. 3 Tesla 23Na Magnetic Resonance Imaging During Aerobic and Anaerobic Exercise. *Acad Radiol*. 2015. doi:10.1016/j.acra.2015.06.005
63. Tarnopolsky MA, Rennie CD, Robertshaw HA, Fedak-Tarnopolsky SN, Devries MC, Hamadeh MJ. Influence of endurance exercise training and sex on intramyocellular lipid and mitochondrial ultrastructure, substrate use, and mitochondrial enzyme activity. *Am J Physiol - Regul Integr Comp Physiol*. 2007. doi:10.1152/ajpregu.00472.2006
64. Bogardus C, Lillioja S, Mott DM, Hollenbeck C, Reaven G. Relationship between degree of obesity and in vivo insulin action in man. *Am J Physiol Metab*. 1985. doi:10.1152/ajpendo.1985.248.3.E286

65. Must A, Jaques PF, Dallal GE, Bajema CJ, Dietz WH. Long-Term Morbidity and Mortality of Overweight Adolescents — A Follow-up of the Harvard Growth Study of 1922 to 1935. *N Engl J Med*. 1992. doi:10.1056/NEJM199211053271904
66. Dietz WH, Richardson S, Goodman N, et al. Health Consequences of Obesity in Youth: Childhood Predictors of Adult Disease. *Pediatrics*. 1998. doi:10.1007/s12098-011-0489-7
67. Daniels SR. The consequences of childhood overweight and obesity. *Futur Child*. 2006. doi:10.1353/foc.2006.0004
68. Saad MF, Knowler WC, Pettitt DJ, Nelson RG, Charles MA, H. Bennett P. A two-step model for development of non-insulin-dependent diabetes. *Am J Med*. 1991. doi:10.1016/0002-9343(91)90547-B
69. Hasegawa N, Kurihara T, Sato K, et al. Intramyocellular and Extramyocellular Lipids Are Associated with Arterial Stiffness. *Am J Hypertens*. 2015. doi:10.1093/ajh/hpv041
70. Jacob S, Machann J, Rett K, et al. Association of increased intramyocellular lipid content with insulin resistance in lean nondiabetic offspring of type 2 diabetic subjects. *Diabetes*. 1999. doi:10.2337/diabetes.48.5.1113
71. Velan SS, Durst C, Lemieux SK, et al. Investigation of muscle lipid metabolism by localized one- and two-dimensional MRS techniques using a clinical 3T MRI/MRS scanner. *J Magn Reson Imaging*. 2007;25(1):192-199. doi:10.1002/jmri.20786
72. Ren J, Dimitrov I, Sherry AD, Malloy CR. Composition of adipose tissue and marrow fat in humans by ^{1}H NMR at 7 Tesla. *J Lipid Res*. 2008. doi:10.1194/jlr.D800010-JLR200
73. Machann J, Stefan N, Wagner R, et al. Intra- and interindividual variability of fatty acid unsaturation in six different human adipose tissue compartments assessed by 1H-MRS in vivo at 3 T. *NMR Biomed*. 2017. doi:10.1002/nbm.3744
74. Vermathen P, Kreis R, Boesch C. Distribution of Intramyocellular Lipids in Human Calf Muscles as Determined by MR Spectroscopic Imaging. *Magn Reson Med*. 2004. doi:10.1002/mrm.10721
75. Weis J, Courivaud F, Hansen MS, Johansson L, Ribe LR, Ahlström H. Lipid content in the musculature of the lower leg: Evaluation with high-resolution spectroscopic imaging. *Magn Reson Med*. 2005. doi:10.1002/mrm.20518

76. Larson-Meyer DE, Newcomer BR, Hunter GR. Influence of endurance running and recovery diet on intramyocellular lipid content in women: a 1H NMR study. *Am J Physiol Metab*. 2002;282(1):E95-E106.
77. Hu J, Willcott MR, Moore GJ. Two-Dimensional Proton Chemical-Shift Imaging of Human Muscle Metabolites. *J Magn Reson*. 1997. doi:10.1006/jmre.1997.1163
78. Newcomer BR, Lawrence JC, Buchthal S, den Hollander JA. High-resolution chemical shift imaging for the assessment of intramuscular lipids. *Magn Reson Med An Off J Int Soc Magn Reson Med*. 2007;57(5):848-858.
79. Weis J, Johansson L, Courivaud F, Karlsson FA, Ahlström H. Quantification of intramyocellular lipids in obese subjects using spectroscopic imaging with high spatial resolution. *Magn Reson Med*. 2007. doi:10.1002/mrm.21085
80. Weis J, Bruvold M, Ortiz-Nieto F, Ahlström H. High-resolution echo-planar spectroscopic imaging of the human calf. *PLoS One*. 2014;9(1). doi:10.1371/journal.pone.0087533
81. Vermathen P, Saillen P, Boss A, Zehnder M, Boesch C. Skeletal muscle 1H MRSI before and after prolonged exercise. I. muscle specific depletion of intramyocellular lipids. *Magn Reson Med*. 2012. doi:10.1002/mrm.24168
82. Bao S, Guttmann CRG, Mugler JP, et al. Spin-echo planar spectroscopic imaging for fast lipid characterization in bone marrow. *Magn Reson Imaging*. 1999. doi:10.1016/S0730-725X(99)00056-9
83. Szczepaniak LS, Dobbins RL, Stein DT, Denis McGarry J. Bulk magnetic susceptibility effects on the assessment of intra- and extramyocellular lipids in vivo. *Magn Reson Med*. 2002. doi:10.1002/mrm.10086
84. Steidle G, Machann J, Claussen CD, Schick F. Separation of intra- and extramyocellular lipid signals in proton MR spectra by determination of their magnetic field distribution. *J Magn Reson*. 2002. doi:10.1006/jmre.2001.2481
85. Steel A, Chiew M, Jezzard P, et al. Metabolite-cycled density-weighted concentric rings k-space trajectory (DW-CRT) enables high-resolution 1 H magnetic resonance spectroscopic imaging at 3-Tesla. *Sci Rep*. 2018. doi:10.1038/s41598-018-26096-y
86. Emir UE, Burns B, Chiew M, Jezzard P, Thomas MA. Non-water-suppressed short-echo-time magnetic resonance spectroscopic imaging using a concentric ring k-space trajectory. *NMR Biomed*. 2017. doi:10.1002/nbm.3714

87. Hu HH, Kim HW, Nayak KS, Goran MI. Comparison of fat-water MRI and single-voxel MRS in the assessment of hepatic and pancreatic fat fractions in humans. *Obesity*. 2010. doi:10.1038/oby.2009.352
88. Fessler JA, Sutton BP. Nonuniform fast Fourier transforms using min-max interpolation. *IEEE Trans Signal Process*. 2003. doi:10.1109/TSP.2002.807005
89. Provencher SW. Estimation of metabolite concentrations from localized in vivo proton NMR spectra. *Magn Reson Med*. 1993. doi:10.1002/mrm.1910300604
90. Meisamy S, Hines CDG, Hamilton G, et al. Quantification of Hepatic Steatosis with T1-independent, T2*-corrected MR Imaging with Spectral Modeling of Fat: Blinded Comparison with MR Spectroscopy. *Radiology*. 2011. doi:10.1148/radiol.10100708
91. Stanisz GJ, Odrobina EE, Pun J, et al. T1, T2 relaxation and magnetization transfer in tissue at 3T. *Magn Reson Med*. 2005. doi:10.1002/mrm.20605
92. Wang Z, Bovik AC, Sheikh HR, Simoncelli EP. Image quality assessment: from error visibility to structural similarity. *IEEE Trans image Process*. 2004;13(4):600-612.
93. Burakiewicz J, Sinclair CDJ, Fischer D, Walter GA, Kan HE, Hollingsworth KG. Quantifying fat replacement of muscle by quantitative MRI in muscular dystrophy. *J Neurol*. 2017. doi:10.1007/s00415-017-8547-3
94. Dyke JP, Lauto A, Schneider E, et al. Homogeneous Water-Lipid Phantoms with Matched T1 and T2 Relaxation Times for Quantitative Magnetic Resonance Imaging of Tissue Composition at 3 . 0 Tesla. 2004;11:2004.
95. Hardy PA, Hinks RS, Tkach JA. Separation of fat and water in fast spin-echo MR imaging with the three-point dixon technique. *J Magn Reson Imaging*. 1995. doi:10.1002/jmri.1880050213
96. Hamilton G, Middleton MS, Bydder M, et al. Effect of PRESS and STEAM sequences on magnetic resonance spectroscopic liver fat quantification. *J Magn Reson Imaging*. 2009. doi:10.1002/jmri.21809
97. Breitkreutz DY, Fallone BG, Yahya A. Effect of J coupling on 1.3-ppm lipid methylene signal acquired with localised proton MRS at 3T. *NMR Biomed*. 2015. doi:10.1002/nbm.3387

98. Yu H, Shimakawa A, McKenzie CA, Brodsky E, Brittain JH, Reeder SB. Multiecho water-fat separation and simultaneous R*2 estimation with multifrequency fat spectrum modeling. *Magn Reson Med*. 2008. doi:10.1002/mrm.21737
99. Golla S, Ren J, Malloy CR, Pascual JM. Intramyocellular lipid excess in the mitochondrial disorder MELAS. *Neurol Genet*. 2017. doi:10.1212/NXG.0000000000000160
100. Schrauwen-Hinderling VB, Hesselink MKC, Schrauwen P, Kooi ME. Intramyocellular lipid content in human skeletal muscle. *Obesity*. 2006. doi:10.1038/oby.2006.47
101. Rico-Sanz J, Thomas EL, Jenkinson G, Mierisová Š, Iles R, Bell JD. Diversity in levels of intracellular total creatine and triglycerides in human skeletal muscles observed by 1 H-MRS. *J Appl Physiol*. 1999;87(6):2068-2072. doi:10.1152/jappl.1999.87.6.2068
102. Nakagawa Y, Hattori M. Intramyocellular lipids of muscle type in athletes of different sport disciplines. *Open Access J Sport Med*. 2017. doi:10.2147/oajsm.s139801
103. Schwenzer NF, Martirosian P, Machann J, et al. Aging effects on human calf muscle properties assessed by MRI at 3 Tesla. *J Magn Reson Imaging*. 2009. doi:10.1002/jmri.21789
104. Sinha R, Dufour S, Petersen KF, et al. Assessment of skeletal muscle triglyceride content by 1H nuclear magnetic resonance spectroscopy in lean and obese adolescents: Relationships to insulin sensitivity, total body fat, and central adiposity. *Diabetes*. 2002. doi:10.2337/diabetes.51.4.1022
105. Shen W, Mao X, Wolper C, et al. Reproducibility of single- and multi-voxel 1H MRS measurements of intramyocellular lipid in overweight and lean subjects under conditions of controlled dietary calorie and fat intake. *NMR Biomed*. 2008. doi:10.1002/nbm.1218
106. Edgerton VR, Smith JL, Simpson DR. Muscle fibre type populations of human leg muscles. *Histochem J*. 1975. doi:10.1007/BF01003594
107. LITHELL H, ÖRLANDER J, SCHÉLE R, SJÖDIN B, KARLSSON J. Changes in lipoprotein-lipase activity and lipid stores in human skeletal muscle with prolonged heavy exercise. *Acta Physiol Scand*. 1979. doi:10.1111/j.1748-1716.1979.tb06471.x
108. Schiaffino S, Reggiani C. Fiber Types in Mammalian Skeletal Muscles. *Physiol Rev*. 2011. doi:10.1152/physrev.00031.2010

109. Strijkers GJ, Araujo ECA, Azzabou N, et al. Exploration of new contrasts, targets, and MR imaging and spectroscopy techniques for neuromuscular disease-A workshop report of working group 3 of the biomedicine and molecular biosciences COST action BM1304 MYO-MRI. *J Neuromuscul Dis*. 2019. doi:10.3233/JND-180333
110. Bredella MA, Fazeli PK, Miller KK, et al. Increased bone marrow fat in anorexia nervosa. *J Clin Endocrinol Metab*. 2009. doi:10.1210/jc.2008-2532
111. Hussain HK, Chenevert TL, Londy FJ, et al. Hepatic Fat Fraction: MR Imaging for Quantitative Measurement and Display—Early Experience. *Radiology*. 2005. doi:10.1148/radiol.2373041639
112. Li C, Kuo YC, Chen C, et al. Quantification of choline compounds in human hepatic tumors by proton MR spectroscopy at 3 T. *Magn Reson Med An Off J Int Soc Magn Reson Med*. 2005;53(4):770-776.
113. Tse GM, Yeung DKY, King AD, Cheung HS, Yang WT. In vivo proton magnetic resonance spectroscopy of breast lesions: An update. *Breast Cancer Res Treat*. 2007. doi:10.1007/s10549-006-9412-8
114. Roebuck JR, Cecil KM, Schnall MD, Lenkinski RE. Human breast lesions: characterization with proton MR spectroscopy. *Radiology*. 1998. doi:10.1148/radiology.209.1.9769842
115. Parente DB, Rodrigues RS, Paiva FF, et al. Is MR spectroscopy really the best MR-based method for the evaluation of fatty liver in diabetic patients in clinical practice? *PLoS One*. 2014. doi:10.1371/journal.pone.0112574
116. Weber MA, Nielles-Vallespin S, Essig M, Jurkat-Rott K, Kauczor HU, Lehmann-Horn F. Muscle Na+ channelopathies: MRI detects intracellular 23Na accumulation during episodic weakness. *Neurology*. 2006. doi:10.1212/01.wnl.0000233841.75824.0f
117. Constantinides CD, Gillen JS, Boada FE, Pomper MG, Bottomley PA. Human skeletal muscle: Sodium MR imaging and quantification - Potential applications in exercise and disease. *Radiology*. 2000. doi:10.1148/radiology.216.2.r00jl46559
118. Bansal N, Szczepaniak L, Ternullo D, Fleckenstein JL, Malloy CR. Effect of exercise on 23Na MRI and relaxation characteristics of the human calf muscle. *J Magn Reson Imaging*. 2000. doi:10.1002/(sici)1522-2586(200005)11:5<532::aid-jmri9>3.3.co;2-r

119. Boada FE, Christensen JD, Huang-Hellinger FR, Reese TG, Thulborn KR. Quantitative in vivo tissue sodium concentration maps: The effects of biexponential relaxation. *Magn Reson Med*. 1994. doi:10.1002/mrm.1910320210
120. Nagel AM, Bock M, Hartmann C, et al. The potential of relaxation-weighted sodium magnetic resonance imaging as demonstrated on brain tumors. *Invest Radiol*. 2011. doi:10.1097/RLI.0b013e31821ae918
121. Gerhalter T, Carlier PG, Marty B. Acute changes in extracellular volume fraction in skeletal muscle monitored by 23Na NMR spectroscopy. *Physiol Rep*. 2017. doi:10.14814/phy2.13380
122. Gerlach DA, Schopen K, Linz P, et al. Atrophy of calf muscles by unloading results in an increase of tissue sodium concentration and fat fraction decrease: a 23Na MRI physiology study. *Eur J Appl Physiol*. 2017. doi:10.1007/s00421-017-3647-4
123. Choi IY, Tkac I, Gruetter R. Single-shot, three-dimensional "non-echo" localization method for in vivo NMR spectroscopy. *Magn Reson Med*. 2000. doi:10.1002/1522-2594(200009)44:3<387::AID-MRM8>3.0.CO;2-3
124. Henning A, Fuchs A, Murdoch JB, Boesiger P. Slice-selective FID acquisition, localized by outer volume suppression (FIDLOVS) for 1H-MRSI of the human brain at 7 T with minimal signal loss. *NMR Biomed*. 2009. doi:10.1002/nbm.1366
125. Nagel AM, Laun FB, Weber MA, Matthies C, Semmler W, Schad LR. Sodium MRI using a density-adapted 3D radial acquisition technique. *Magn Reson Med*. 2009. doi:10.1002/mrm.22157
126. Gast L V., Henning A, Hensel B, Uder M, Nagel AM. Localized B0 shimming based on 23Na MRI at 7 T. *Magn Reson Med*. 2020. doi:10.1002/mrm.28011
127. Sutton BP, Noll DC, Fessler JA. Fast, iterative image reconstruction for MRI in the presence of field inhomogeneities. *IEEE Trans Med Imaging*. 2003. doi:10.1109/TMI.2002.808360
128. Nguyen HM, Peng X, Do MN, Liang ZP. Denoising MR spectroscopic imaging data with low-rank approximations. *IEEE Trans Biomed Eng*. 2013. doi:10.1109/TBME.2012.2223466

129. Jackson JI, Meyer CH, Nishimura DG, Macovski A. Selection of a Convolution Function for Fourier Inversion Using Gridding. *IEEE Trans Med Imaging*. 1991. doi:10.1109/42.97598
130. Gerhalter T, Gast L V., Marty B, Uder M, Carlier PG, Nagel AM. Assessing the variability of 23Na MRI in skeletal muscle tissue: Reproducibility and repeatability of tissue sodium concentration measurements in the lower leg at 3 T. *NMR Biomed*. 2020. doi:10.1002/nbm.4279
131. Blunck Y, Josan S, Taqdees SW, et al. 3D-multi-echo radial imaging of 23Na (3D-MERINA) for time-efficient multi-parameter tissue compartment mapping. *Magn Reson Med*. 2018. doi:10.1002/mrm.26848
132. Riemer F, Solanky BS, Wheeler-Kingshott CAM, Golay X. Bi-exponential 23Na T2* component analysis in the human brain. *NMR Biomed*. 2018. doi:10.1002/nbm.3899
133. Lommen JM, Flassbeck S, Behl NGR, et al. Probing the microscopic environment of 23 Na ions in brain tissue by MRI: On the accuracy of different sampling schemes for the determination of rapid, biexponential T2* decay at low signal-to-noise ratio. *Magn Reson Med*. 2018. doi:10.1002/mrm.27059
134. Ridley B, Nagel AM, Bydder M, et al. Distribution of brain sodium long and short relaxation times and concentrations: a multi-echo ultra-high field 23Na MRI study. *Sci Rep*. 2018. doi:10.1038/s41598-018-22711-0
135. Syeda W, Blunck Y, Kolbe S, Cleary JO, Johnston LA. A continuum of T2* components: Flexible fast fraction mapping in sodium MRI. *Magn Reson Med*. 2019. doi:10.1002/mrm.27659
136. Stollberger R, Wach P. Imaging of the active B1 field in vivo. *Magn Reson Med*. 1996. doi:10.1002/mrm.1910380225
137. Han TS, Al-Gindan YY, Govan L, Hankey CR, Lean MEJ. Associations of body fat and skeletal muscle with hypertension. *J Clin Hypertens*. 2019. doi:10.1111/jch.13456
138. M. W, A.M. N, K. J, H.-U. K, W. S, F. L. Increased muscular sodium concentration is demonstrated in duchenne muscular dystrophy by sodium (23NA) MRI. *Neuroradiology*. 2011. doi:10.1007/s00234-011-0914-7

139. Crescenzi R, Donahue PMC, Petersen KJ, et al. Upper and Lower Extremity Measurement of Tissue Sodium and Fat Content in Patients with Lipedema. *Obesity*. 2020. doi:10.1002/oby.22778
140. Alhulail AA, Patterson DA, Xia P, et al. Fat–water separation by fast metabolite cycling magnetic resonance spectroscopic imaging at 3 T: A method to generate separate quantitative distribution maps of musculoskeletal lipid components. *Magn Reson Med*. 2020. doi:10.1002/mrm.28228
141. Dyer AR, Elliott P, Shipley M, Stamler R, Stamler J. Body mass index and associations of sodium and potassium with blood pressure in INTERSALT. *Hypertension*. 1994. doi:10.1161/01.hyp.23.6.729
142. Ortiz-Nieto F, Johansson L, Ahlström H, Weis J. Quantification of lipids in human lower limbs using yellow bone marrow as the internal reference: Gender-related effects. *Magn Reson Imaging*. 2010. doi:10.1016/j.mri.2010.03.014
143. Charalambous BM, Webster DJT, Mir MA. Elevated skeletal muscle sodium-potassium-ATPase in human obesity. *Clin Chim Acta*. 1984;141(2-3):189-195. doi:10.1016/0009-8981(84)90010-X
144. SKOU JC. ENZYMATIC BASIS FOR ACTIVE TRANSPORT OF NA+ AND K+ ACROSS CELL MEMBRANE. *Physiol Rev*. 1965. doi:10.1152/physrev.1965.45.3.596
145. Gerhalter T, Gast L V., Marty B, et al. 23Na MRI depicts early changes in ion homeostasis in skeletal muscle tissue of patients with duchenne muscular dystrophy. *J Magn Reson Imaging*. 2019. doi:10.1002/jmri.26681
146. Lionikas A, Blizard DA, Vandenbergh DJ, et al. Genetic architecture of fast- and slow-twitch skeletal muscle weight in 200-day-old mice of the C57BL/6J and DBA/2J lineage. *Physiol Genomics*. 2004. doi:10.1152/physiolgenomics.00103.2003
147. Yi SS, Firestone MJ, Beasley JM. Independent associations of sodium intake with measures of body size and predictive body fatness. *Obesity*. 2015. doi:10.1002/oby.20912
148. Morrow JM, Sinclair CDJ, Fischmann A, et al. Reproducibility, and age, body-weight and gender dependency of candidate skeletal muscle MRI outcome measures in healthy volunteers. *Eur Radiol*. 2014. doi:10.1007/s00330-014-3145-6
149. UNGER RH, ORCI L. Diseases of liporegulation: new perspective on obesity and related disorders. *FASEB J*. 2001. doi:10.1096/fj.00-0590

150. Zhang X, Lerman LO. The metabolic syndrome and chronic kidney disease. *Transl Res*. 2017. doi:10.1016/j.trsl.2016.12.004
151. Tsai S, Clemente-Casares X, Revelo XS, Winer S, Winer DA. Are obesity-related insulin resistance and type 2 diabetes autoimmune diseases? *Diabetes*. 2015. doi:10.2337/db14-1488
152. Kleinewietfeld M, Manzel A, Titze J, et al. Sodium chloride drives autoimmune disease by the induction of pathogenic TH 17 cells. *Nature*. 2013. doi:10.1038/nature11868
153. Wenner MM, Paul EP, Robinson AT, Rose WC, Farquhar WB. Acute NaCl loading reveals a higher blood pressure for a given serum sodium level in African American compared to Caucasian adults. *Front Physiol*. 2018. doi:10.3389/fphys.2018.01354